UNIVERSITÀ
DEGLI STUDI
FIRENZE

**DOTTORATO DI RICERCA IN**
**FISICA E ASTRONOMIA**

CICLO XXX

COORDINATORE Prof. Raffaello D'Alessandro

# *Study of the reaction $^{80}Kr + ^{40,48}Ca$ at 35 MeV/u with the FAZIA detector array*

Settore scientifico disciplinare: FIS/04 Fisica nucleare e subnucleare


**Dottorando**

Dott. Giuseppe Pastore

**Tutore**

Dott. Gabriele Pasquali

**Coordinatore**

Prof. Raffaello D'Alessandro


Anni 2014 / 2017

A Monica,

fonte di forza e ispirazione
senza la quale
ben poco di questo lavoro
avrebbe visto la luce

# Contents

# Introduction

Since more than fifty years heavy ion collisions have been an important tool to study the properties of nuclear matter far from equilibrium conditions [1, 2]. One of the aspects still attracting experimental and theoretical investigations is the behaviour of the nuclear equation of state (EOS), which describes the properties of nuclear matter in terms of macroscopic variables such as density, pressure, temperature, volume. In particular two issues are still under study: the dependence of the EOS on the density and on the nucleonic asymmetry [3]. The latter point requires the investigation of observables depending on the isospin[1] of the products and, as a consequence, it is a challenge from the experimental side because it needs detectors able to measure Z and A of the ejectiles in over the largest possible range of Z, possibly also with very low energy thresholds. Moreover, in order to extract some information about the EOS it is necessary to compare the experimental data with the predictions of sophisticated microscopic models (such as, for example, the dynamical model AMD [4], used in this work coupled to the statistical code GEMINI++ [5] as afterburner), employing different parametrization of the EOS and in particular of its symmetry energy ($E_{sym}$).

Heavy ion collisions at Fermi energy are one of the best tools to study this topic because the colliding nuclear system during its evolution explores regions far from normal conditions, thus allowing to test the density dependence of the symmetry energy. For example, in peripheral and semiperipheral collisions it is well known that the exit channel is mainly binary, with two heavy fragments (called QP, for "quasi-projectile" and QT for "quasi-target", see Chap. 1). If the entrance channel is asymmetric, a nucleon exchange takes place during the interaction phase, aiming at restoring the isospin equilibration of the whole system; the efficiency of this process (called isospin diffusion) depends on $E_{sym}$. Moreover, in these reactions a large amount of emission at midvelocity was observed and generally attributed to the rupture of the "neck" [6] forming between QP and QT in the first phase of the reaction reference. Such a structure is expected to be at lower density with respect

[1]We want to note that in the literature, especially in experimental papers concerning the study of the isospin related phenomena, the isospin parameter is often defined as N/Z.

to QP and QT; as a consequence, the measurement of the neutron to proton ratio of midvelocity fragments allows for testing the density dependence of $E_{sym}$: an isospin migration (drift) towards the neck region is expected [7, 8].

The present work is part of the mainstream experimental studies on the symmetry energy. In fact the reactions $^{80}\mathrm{Kr} + ^{40,48}\mathrm{Ca}$ at 35 MeV/u were investigated by means of an experimental apparatus called FAZIA which represents the "state of the art" from the point of view of the isotopic identification without using a mass spectrometer [9]. FAZIA is the result of a long R&D phase which allowed to push to their limit the identification capabilities of the silicon detectors.

The experiment discussed in this work was the first physics experiment exploiting FAZIA and it was performed with a reduced version of the setup, i.e. only four blocks covering a reduced fraction of the solid angle; polar angles with respect to the beam going approximately from 5° to 17°. Nevertheless as it will be shown in the following Chapters, it was possible to separate different classes of events (peripheral and central collisions) and, in particular, to investigate the isospin transport phenomena (drift and diffusion), also comparing the results with the prediction of AMD + GEMINI. The fission of the QP was also investigated, with a particular focus on the events in which the mass was measured for both fission fragments. Comparing the <N>/Z of the fission products with the Evaporation Attractor Line (EAL) [10] it was possible to establish that the largest part of the fission events are of dynamical and not of statistical nature, i.e. they take place in the first phase of the reaction (t< 300 fm/c).

The thesis is organized as follows: in Chapter 1 a theoretical description of the studied phenomena is reported; in Chapter 2 the results obtained by the FAZIA Collaboration during the R&D phase will be presented in more detail also evidencing the nice results recently obtained in the optimization of the Pulse Shape Analysis (PSA) isotopic identification in the framework of this work [11]; Chapter 3 is dedicated to the description of the experimental setup of the ISO-FAZIA experiment and to the long and complex calibration and identification procedure needed to perform the physics analysis; in Chapter 4 the used theoretical models are presented; Chapter 5 is dedicated to the description of the imposed conditions in order to sort the events according to their reaction mechanisms; finally, in Chapter 6 the results of the analysis and the comparison with the model predictions are reported.

# Chapter 1

# Physics case

## 1.1 Heavy-Ion reaction landscape

Heavy-ion reactions allow to investigate a large number of different intrinsic and collective aspects of the nuclei. The reaction mechanisms strongly depends on the energy domain which can be varied studying different time scales or different processes or maybe even the thermodynamic aspects of the nuclear matter. For this reason, heavy-ion reactions are one of the most important tools used to study the nuclear Equation of State (nEoS). The interaction between nucleons inside two colliding nuclei can be treated in different ways depending on the energy involved in the reaction. It is possible to distinguish two main energy regimes widely studied in the last fifty years:

- **low energy regime** (beam energy lower than $\sim 15\,\mathrm{MeV/u}$): the kinetic energy transferred to the nucleons during the reaction is low and the Pauli exclusion principle is very effective in reducing the nucleon-nucleon collisions and the possibility to reach a nucleon free-state. Since the de Broglie wavelength of the nucleons is larger than the mean distance between the nucleons inside the nucleus, their behaviour is determined by collective interactions (mean-field). During the relatively long interaction time ($\sim 10^{-21}\,\mathrm{s}$) almost a complete chemical and thermal equilibration is reached. In this kind of reaction a great part of the initial kinetic energy is dissipated into the internal degrees of freedom. For central collision the formation of a compound nucleus (an equilibrated system including the initial projectile and target, highly excited and without memory of the entrance channel) is favoured [12]. Its de-excitation is governed by the statistical competition between the different decay channels available in the phase-space such as emission of particles, $\gamma$-decay or sequential fission.

For more peripheral collision, the Deep Inelastic process (DIC) is responsible for practically the entire reaction cross section. In this kind of reaction, a binary exit channel is observed and only part of the kinetic energy of the relative motion is transferred to the internal degrees of freedom. The more peripheral the reaction, the less effective the energy dissipation. The two excited fragments keep memory of their previous identity and for this reason they are thus called Quasi-Projectile (QP) and Quasi-Target (QT);

- **high energy regime** (beam energy higher than $\sim 100\,\mathrm{MeV/u}$): the kinetic energy transferred to the nucleons is high enough to allow them to reach a nucleonic free-state in spite of the Pauli exclusion principle, which can be neglected. For increasing energy, the wavelength of the nucleons becomes smaller than the mean distance among the nucleons inside the nucleus and the collective properties assume a lower relevance with respect to the nucleon-nucleon collisions. In these conditions only a small group of nucleons takes part to the interaction according to the "participant-spectator" model [13, 14]. The participants form a "fireball" of dense hot matter travelling at about the center of mass (CM) velocity of the participant nucleons and emitting energetic nucleons, while the spectators form a low excited region which decays by evaporative emissions.

In between this two energy regions, there is an intermediate energy interval (beam energy between $15\,\mathrm{MeV/u}$ and $\sim 100\,\mathrm{MeV/u}$) called "Fermi region" which represents a transition region which requires a more complex description. In fact, in this energy regime, features typical of the low and the high energy regime coexist because both the mean field and the nucleon-nucleon collisions play some role.

In this work a study of the reaction $^{80}\mathrm{Kr} + ^{48,40}\mathrm{Ca}$ at $35\,\mathrm{MeV/u}$ is presented and therefore a few more details about the intermediate energy regime will be given in Sec. 1.1.1. The reasons for choosing this particular projectile/target combination will be given in Sec. 3.1.

### 1.1.1 Intermediate energy

In the Fermi energy regime the de Broglie wavelength of the nucleons is comparable to the mean distance among the nucleons inside the nuclei. As a consequence neither the mean-field interaction not the nucleon-nucleon collisions can be neglected. In fact, at this energies nucleon-nucleon collisions are able to promote nucleons in one of the available free-states respecting the Pauli principle. The interaction time at intermediate energy is $\sim 10^{-22}\,\mathrm{s}$, about one order of magnitude shorter than for

the low energy regime. As a consequence, the system is not able to reach complete thermal equilibration.

The peripheral and semi-peripheral collisions around the Fermi energies are dominated by binary deep inelastic collisions. In this kind of reactions, according to the experimental observations and theoretical models, the contact region between the projectile and the target forms an elongated low density region called "neck" or "mid-velocity region". The neck zone is involved in a great number of different phenomena and it has been studied deeply in the last thirty years [6, 15–19]. The neck zone is subject to fast break up due to the rise of nuclear mechanical instabilities caused by temperature and pressure effects. A fast fragmentation of the neck structure has been observed, associated to the prompt emission of Intermediate Mass Fragments (IMF) moving away rapidly from the neck because of the Coulomb repulsion. The typical neck emission is also called "mid-velocity" emission due to the typical observed velocities which are, for kinematical reasons, around the CM velocity of the system.

By reducing the impact parameter of the collision the probability to observe an incomplete fusion or a multi-fragmentation increases. In the intermediate energy regime the probability of a complete fusion between projectile and target is quite low. Nevertheless, incomplete fusion between the projectile and a small amount of nucleons of the target has been observed for central events [20, 21]. In multi-fragmentation events, many IMFs are produced, all coming from the disassembly of a unique possibly equilibrated central source including a large fraction of the total mass of the system. The excitation energy of the fragmenting source is very high ($E^* \geq$4-5 MeV depending on the size of the nucleus) [22].

Independently of the reaction mechanism, the products of the dynamical phase of the collision are called *primary* fragments and thus usually are excited fragments. In the case of a DIC reaction, there are two main fragments (QP and QT) plus Light Charged Particles (LCP) or IMFs emitted from neck. The de-excitation of these hot fragments can occur by means of different competitive processes such as statistical decay (Sec. 1.1.2) or fission (Sec. 1.1.3). In the latter case the produced fission fragments may be affected by a following statistical evaporation.

### 1.1.2 Statistical evaporation decay

The statistical model for the decay of the compound-nucleus (CN) was originally introduced by Bohr, Bethe and Weisskopf. Wolfenstein [23], Hauser and Feshbach [24] have taken into account the conservation of total angular momentum and afterwards the model was extended and generalized by many authors. Nowadays it is extensively used in many reaction scenarios in which compound nuclei are formed after a

nuclear collision.

The hypothesys at the basis of the model is that the CN is a complete equilibrated system and that its de-excitation is totally independent of the way it was created. The primary hot fragments produced in a heavy-ion reaction are generally treated as small CNs, i.e. equilibrated systems whose decay is independent of the way they were produced.

The statistical decay promotes the de-excitation of these fragments via the different competitive open decay channels such as the $\gamma$-emissions, the particles evaporation or the statistical fission. The decay probability depends on the excitation energy $E^*$ of the fragment, on its angular momentum $J$ and on its charge $Z$ and mass $A$, and, of course, on Z and A of the evaporated particles. Applying the Fermi golden rule it is possible to find the transition probability from the initial state to one of the possible final states of the system and thus evaluate the branching ratios between the open channels. The cold particles and fragments obtained at the end of the statistical emission from the primary fragments are called *secondary* products. In the experiment, case only secondary fragments can be detected due to the relatively long time (with respect to the emission time scale) required by the particles to reach the detectors. For this reason a statistical-model is usually employed as "afterburner" in all the simulation codes describing the dynamic phase in order to obtain model predictions comparable to the experimental data.

The secondary fragments obtained after the particle evaporation of the excited primary fragments move their location in the chart of nuclides towards a line called Evaporation Attractor Line (EAL), studied for the first time by R. J. Charity [10]. In fig. 1.1, taken from the Charity paper, the EAL line is plotted on the nuclide chart. Neutron-rich primary fragments evaporate, on average, more neutrons than protons thus attaining a more equilibrated ratio between protons and neutrons. For proton-rich nuclei the opposite behaviour happens. Protons and neutrons emission rates are similar only when their "energy cost" are of the same order. Depending on which side of the EAL a fragment is, either neutron or proton emission quickly dominates. In order to move towards the EAL line, the fragment cools down by particle emission, thus moving horizontally or vertically in the nuclide chart depending on whether the primary fragment is in the neutron-rich or proton-rich region (in fig. 1.1 the trajectories of the primary fragments (large solid markers) are drawn as a function of the initial excitation energy). Only when the excitation of the fragment is low enough it approaches the EAL line. However, primary fragments too far from the EAL will evaporate towards the EAL but they will never reach it, since they exhaust their excitation energy before. Therefore the final position of the cold secondary fragments depends on the initial excitation energy of the primary fragments.

Fragments on the EAL line have similar neutron and proton decay rates and

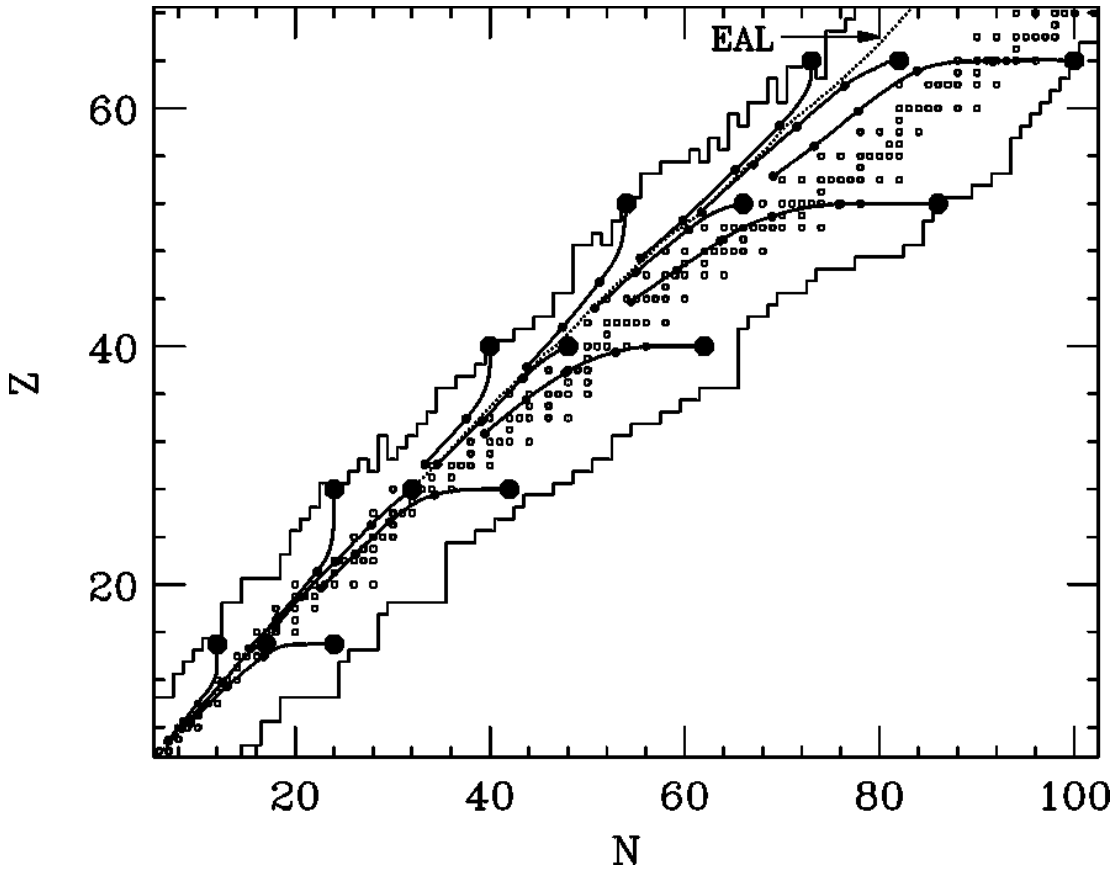


**Figure 1.1:** *Figure taken from Ref. [10]. The caption as it appears in the reference is: "The curves show the loci of the predicted, average locations of secondary fragments in the chart of nuclides for the compound nuclei indicated by the large solid points. The small points on these curves correspond to the average location of secondary fragments as the excitation energy is increased in 100 MeV increments. The evaporation attractor line (EAL) is indicated.".*

hence their neutron richness does not change and the following evaporation follows the attractor line down in mass. The slope of the EAL line depends on the decay width of neutrons, $\Gamma_N$, and protons, $\Gamma_Z$, including all the emissions of more complex fragments and it is given by the average ratio $< \Gamma_N/\Gamma_Z >$. This means that if the primary fragment is on the EAL the average number of evaporated protons and neutrons is the same independently on how the primary fragment has been produced. The EAL line has been evaluated using the GEMINI statistical code [5] (this code has been used also in this thesis and it is described in Sec. 4.2) starting from different nuclei with different initial excitation energy. The EAL line has been parametrized as a function of A and Z of the nucleus and can be written as:

$$A = 2.072Z + 2.32 \times 10^{-3} Z^2 \tag{1.1}$$

The EAL line lies on the neutron deficient side of the $\beta$-stability line due to the presence of the Coulomb barrier. For the heavier fragments whose Coulomb barrier is higher, the EAL lies farther away with respect to the $\beta$-stability line than for lighter ones. In the nuclide chart, the farther the initial fragment position from the EAL, the farther will be the final one. The lighter the primary nucleus, the closer the final position will be to the EAL. For $Z > 82$ the EAL is not considered very reliable because it crosses the line of known isotopes. The exact location of the EAL in that region of the nuclide chart is uncertain.

An important remark of R. J. Charity work is that, as a consequence of the evaporation decay, a nuclear fragment can never have an average decay trajectory crossing the attractor line, but only a trajectory approaching the line without crossing it.

### 1.1.3 Fission

The fission of the hot fragments after the collision is one of the main de-excitation processes together with the statistical particle evaporation. The fission mechanism has been studied since 1938 by Otto Hahn and Fritz Strassmann and nowadays it represents one of the more well known reaction processes. The sequential fission of an excited fragment produced in a heavy ion reaction is a statistical process in which the fissioning deformed nucleus is a thermodynamically equilibrated system with no memory of the initial collision which generated it. When the deformation of the hot source is greater than the surface energy term of the nuclear binding energy, the nucleus breaks up into two main pieces according to the angular momentum and energy conservation laws. The fission fragments are produced with a mass distribution depending on the system energy and size and they are isotropically emitted in the reaction plane.

In heavy ion collisions also a fast fission mechanism called "dynamical fission" has also been observed and studied in the last twenty years [25–28]. In binary collisions at the end of the interaction phase, the excited and deformed primary QP may separate in two fragments on time scales of the order of 100-150 fm/c. At variance with the sequential fission, which takes place on longer time scales, the fission fragments are not isotropically emitted. An aligned configuration appears, the more aligned the more asymmetric the mass splitting, with the heavier fragment emitted towards the non fissioning primary fragment.

The experimental anisotropy observed in the angular distribution of the fragments and the observation of some ternary and quaternary aligned breakup process after DIC reactions represent a confirmation of this kind of fast process [29].

## 1.2 Nuclear equation of state

Heavy ion collisions at the Fermi energy regime constitute a good tool to investigate the properties of the nuclear equation of state because regions of density different from the normal density are explored by the system during the collision.

Nowadays accessing the properties of nuclear matter, consisting of an infinite number of neutrons and protons interacting via Van-der-Waals-like forces[1], is one of the main research topics in nuclear physics. The behaviour of the nuclear matter in terms of thermodynamic observables (like density, temperature, pressure, volume or isospin) can be described by means of the nuclear Equation of State (nEoS). A nucleus in its ground state is a system at temperature $T = 0$ and density $\rho_0 = 0.16\,\mathrm{fm}^{-3}$ (called saturation density). The Bethe-Weizsaecker formula can be considered the first attempt to describe the nucleus as a thermodynamic system governed by different kind of forces. Starting from and extending the liquid-drop model, the physicists deduced the equation for the binding energy ($E_b$) of a nucleus with charge $Z$ and atomic number $A$:

$$E_b = a_v A - a_s A^{\frac{2}{3}} - a_c \frac{Z(Z-1)}{A^{\frac{1}{3}}} - a_{sym} \frac{(A-2Z)^2}{A} + \delta(A,Z) \tag{1.2}$$

The parameters $a_v$, $a_s$, $a_c$ and $a_{sym}$ represent the intensity of the volume, surface, Coulomb and asymmetry energy terms respectively; $\delta(A,Z)$ is a correction parameter which takes into account the and the pairing force. The Bethe-Weizsaecker formula works well for nuclei in the ground state, i.e. in standard condition of temperature and density, but it cannot describe the energy of an excited nucleus. The nEoS is aimed at describing the energy per nucleon of a nucleus far from ground-state conditions. Most of our experimental and theoretical knowledge about nEoS regards symmetric nuclear matter at saturation density, so that many efforts are in progress to figure out behaviour of asymmetric nuclear matter in extreme conditions.

Heavy-ion collisions allow to study the nEoS under laboratory controlled conditions. In fact, by increasing the beam energy one can produce nuclear systems at higher densities (supra-saturation densities, $\rho/\rho_0 > 1$) in the early stage of the reaction (around $t \approx 20\,\mathrm{fm/c}$). The system later expands to sub-saturation densities ($\rho/\rho_0 < 1$). In this way is possible to explore different regions of the nEoS diagram.

[1]The nuclear matter consists of an infinite number of neutrons and protons interacting via a nucleon-nucleon interaction which is a residual interaction with respect to the strong interaction between the quarks in a nucleon. In that respect, the nucleon interaction resembles the Van der Waals force between molecules.

### 1.2.1 Asymmetric nuclear matter

As it is obvious from eq. 1.2, the symmetry energy term is null for symmetric nuclear matter ($N = Z$). To take into account the differences between the behaviour of the symmetry energy term in symmetric and asymmetric nuclear matter, the nEoS can be written as a function of the density and the neutron-proton content (called *isospin* $I$[2]) which is defined as:

$$I = \frac{\rho_n - \rho_p}{\rho} = \frac{N - Z}{A}$$

where $\rho_n$ and $\rho_p$ are the neutron and proton densities relative to the total nucleon density $\rho$ respectively. Trying to isolate the effect of the asymmetry, the nEoS can be expressed in a parabolic form [2]:

$$E_b(\rho, I) = E_b(\rho, I = 0) + E_{sym}(\rho)I^2 \tag{1.3}$$

The first term does not depend on the isospin ($I = 0$ for a system with $N = Z$) and so it represents the binding energy evaluated for symmetric nuclear matter. The second term includes all the asymmetry dependence and qualitatively it is the amount of energy required to change all protons into neutrons in symmetric nuclear matter. Thus, the symmetry energy can also be defined as the difference between the binding energy of pure neutron matter, $E(\rho, 1)$, and symmetric nuclear matter, $E(\rho, 0)$.

The symmetry energy $E_{sym}$ can be expanded in a Taylor series around the saturation density $\rho_0$ [30]:

$$E_{sym}(\rho) = S_0 - L\epsilon + \frac{1}{2}K_{sym}\epsilon^2 + O[\epsilon^3] \tag{1.4}$$

where $S_0$ is the symmetry energy term at $\rho_0$ obtained from the Bethe-Weizsaecker formula, $L$ is the slope parameter of the curve, $K_{sym}$ is the curvature parameter which defines the incompressibility of nuclear matter and $\epsilon$ is a defined as $\epsilon = (\rho - \rho_0)/(3\rho_0)$.

A good knowledge of the $E_{sym}(\rho)$ potential is still lacking far from saturation conditions. There are a large number of different parametrizations studied and used in the literature [3]. Though all the parametrizations assume the same behaviour at normal conditions, they are in strong disagreement when compared in supra-saturation or sub-saturation density regions. In this work we have compared our experimental data with simulations (see Chapter. 4) performed with two different parametrizations (asy-stiff and asy-soft) whose dependence on density is reported

[2] We want to note again that in the literature, especially in experimental papers concerning the study of the isospin related phenomena, the isospin parameter is often defined as N/Z.

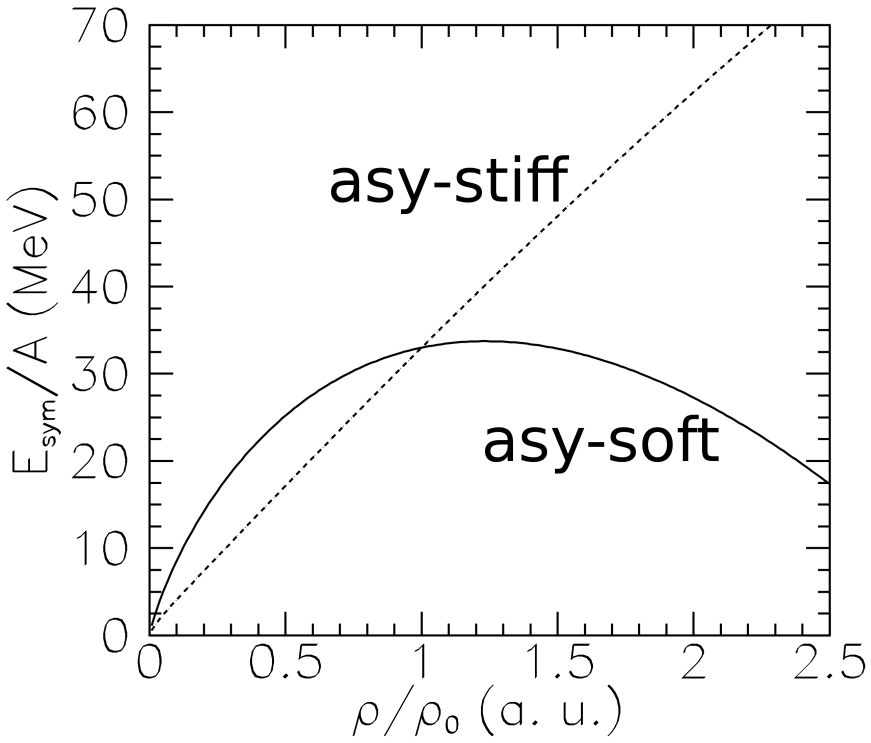


**Figure 1.2:** *Density dependence of the symmetry energy term obtained from theoretical calculations using the asy-stiff and asy-soft parametrizations of the nEoS.*

in fig. 1.2. One of the main goal of this thesis was to try to constraint the density dependence of the symmetry energy term by working with isospin observables sensitive to the the $E_{Sym}$ parametrization. In fact, experimental constraints on the $E_{sym}$ density dependence may help to enhance the accuracy of predictions of astrophysical phenomena [2, 31–33], the understanding of fundamental nucleon-nucleon interactions, in addition to the knowledge of the general properties of the nuclear matter [2, 34, 35].

In a recent and very interesting paper, Bao-An Li and Xiao Han [36] have reported all the constrainted values of the $E_{sym}(\rho_0)$ and $L(\rho_0)$ from 28 different analysis of terrestrial experiments and astrophysical observations. All these predictions have been gathered together in the plot shown in fig. 1.3 taken from their paper. The error bars associated to the different points are different because they depend on the particular experimental apparatus used. An average value for the two studied parameters has been estimated: $E_{sym}(\rho_0) = 31.5542$ and $L_{sym}(\rho_0) = 58.8865$.

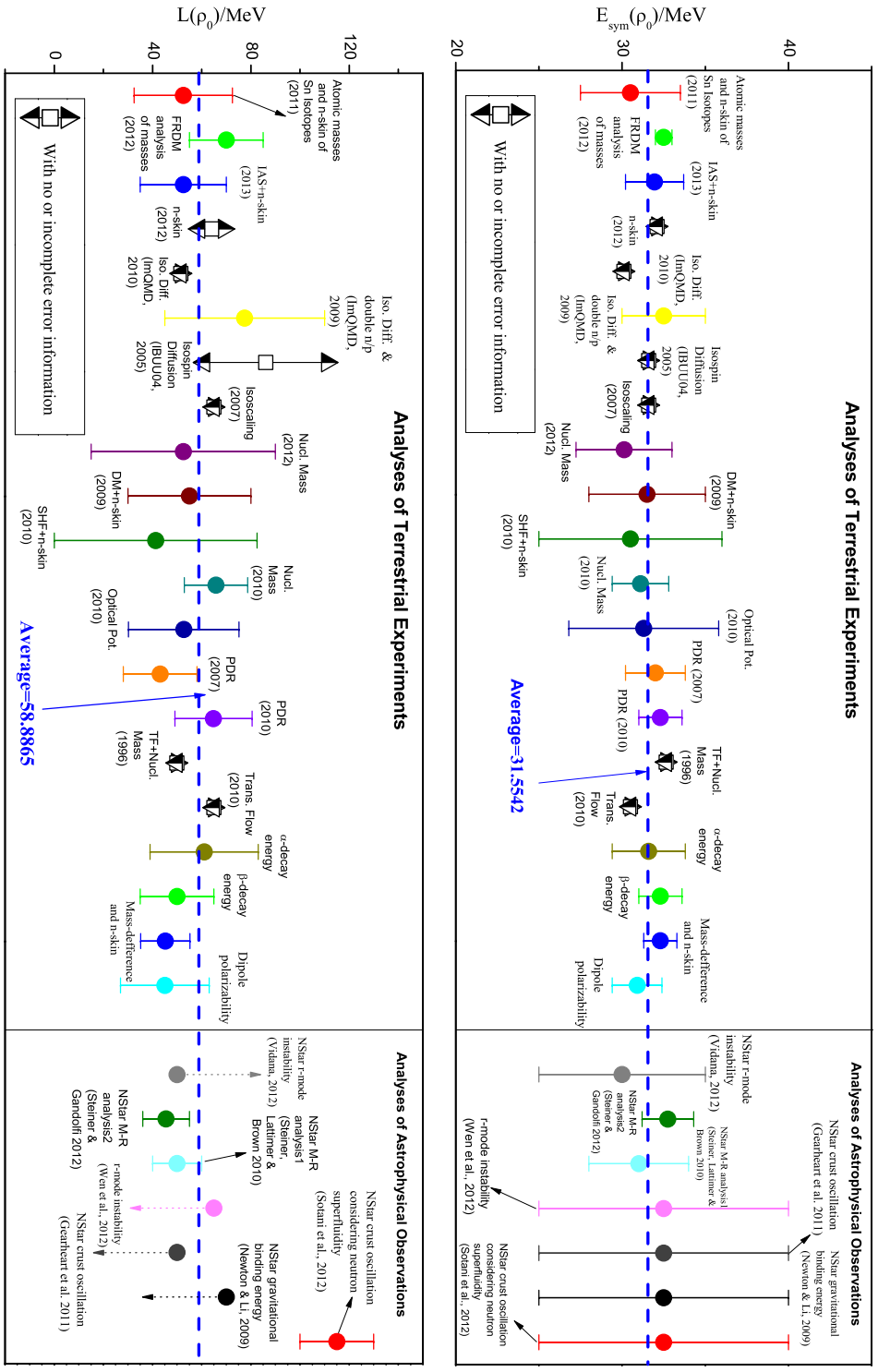


**Fig. 1.** (Color online.) Nuclear symmetry energy (upper) and its slope $L$ (lower) at normal density of nuclear matter from 28 analyses of terrestrial nuclear laboratory experiments and astrophysical observations.

**Figure 1.3:** *Figure and caption taken from Ref. [36]: Bao-An Li and Xiao Han, Phys. Lett. B (2013) 276-281.*

### 1.2.2 Isospin transport phenomena

The study of the isospin diffusion and drift phenomena [37, 38] in peripheral and semi-peripheral collisions is one of the several tools which have been used more or less successfully in literature to probe the symmetry energy at intermediate energies [2]. In order to enhance the effects induced by $E_{sym}$ on nuclear dynamics due to the $I^2$ factor of eq. (1.3), it is useful to study nuclear collisions in asymmetric systems i.e. using a projectile and a target having a large difference in $I$.

As already said, peripheral and semi-peripheral collisions at Fermi energies mostly evolve towards a binary mechanism which is characterized by the formation of a QP and a QT. Isospin transport is described as the exchange of nucleons between the projectile and the target during the dynamic phase of compression and expansion of the nuclear matter happening during the collision. Involving also the low density neck region, this process of neutron migration between projectile and target is also sensitive to the low-density behaviour of the $E_{sym}$ [8].

Considering the behaviour of neutron and proton chemical potentials as a function of the density $\rho$ and the isospin $I$, the proton/neutron currents can be written as:

$$\mathbf{j}_{p/n} = D^{\rho}_{p/n}\nabla\rho - D^{I}_{p/n}\nabla I \tag{1.5}$$

where $D^{\rho}_{p/n}$ and $D^{I}_{p/n}$ are the drift and diffusion coefficients for transport described in [7]. From eq. (1.5) two different contributions to the neutron and proton migration can be distinguished: the **isospin drift**, defined as the motion of nucleons due to a density gradient in the system ($\nabla\rho$) and the **isospin diffusion**, i.e. the motion of nucleons due to an asymmetry gradient ($\nabla I$).

Experimentally, the interest in the study of the isospin transport phenomena is related to the link between the difference of proton/neutrons currents and the $E_{sym}$ value (and also its density dependence). In fact, as shown below by eq. (1.6) and (1.7), the isospin diffusion depends directly on the absolute value of $E_{sym}$ while the isospin drift depends on the slope of $E_{sym}$ as a function of $\rho$:

$$D^{\rho}_{n} - D^{\rho}_{p} \propto 4I\frac{\partial E_{sym}}{\partial\rho}, \tag{1.6}$$

$$D^{I}_{n} - D^{I}_{p} \propto 4\rho E_{sym} \tag{1.7}$$

Hence transport phenomena in nuclear reactions appear directly linked to the EOS properties.

While the diffusion phenomenon can be observed only for asymmetric systems, the drift effect is always present (independently of the neutron-proton symmetry of the system) as long as the energy of the reaction and the size of the system is

large enough to generate a density gradient inside the hot nuclear matter. In a binary collision (in the low-density neck region) a density gradient is formed and the isospin transport phenomena, mainly ruled by the density derivative of the symmetry energy, lead to a larger neutron flow towards the neck clusters. This mechanism leads to the neutron enrichment of the neck region and it is strongly sensitive to the different symmetry energy parametrizations used to theoretically describe the phenomenon.

The diffusion component will tend to smooth out the isospin asymmetries in the system through the exchange of protons and neutrons in order to balance the asymmetry across the system as a whole. If we consider an infinite contact time between projectile and target, one would expect that on the average the final equilibrated products would be homogenous in isospin content. Since the contact time is not infinite, the measurement of the amount of equilibration that has occurred can lead to an understanding of the strength of the drift and diffusion components of nucleon transport mechanism [2, 8, 39, 40].

# Chapter 2

# The FAZIA detector array

## 2.1 The FAZIA detector telescope

The FAZIA (Four-$\pi$ A Z Identification Array [41]) Collaboration was born in 2006 and it is mainly an Italian-French collaboration with the participation of other researchers from different countries. The goal of the FAZIA Collaboration is the design of a next-generation detector array optimized for energy measurements and charge and mass identification of charged fragments in the energy range 10-100 MeV/u. The detector is designed for easy transport and coupling with other detection apparatuses. It features a modular architecture based on a three stage $\Delta$E-E telescope and digitizing readout electronics. After the FAZIA R&D phase, a first demonstrator (consisting of 4 blocks and more than 48 $\Delta$E-E telescopes) has been built. Its good performance in terms of isotopic identification and energy measurement puts FAZIA at the forefront among the detector arrays for nuclear physics studies with charged particles, especially now that its angular coverage has been extended by adding new blocks.

The FAZIA telescope consists of two silicon detectors $\sim$300 $\mu$m and $\sim$500 $\mu$m thick respectively, named Si1 and Si2 in the following, and a CsI(Tl) (Cesium Iodide doped with Thallium) $\sim$ 10 cm thick, named CsI in the following.

Basing on the experience acquired during the R&D phase, the FAZIA Collaboration designed the final FAZIA "block" shown in figure 2.1. Every block is made up of 16 telescopes mounted as a square $4 \times 4$ matrix. Every silicon pad has a surface of $2 \times 2$ $cm^2$ so that the entire block covers about $8 \times 8$ $cm^2$ (a solid angle of 6.2 msrad at a distance of 80 cm from target). Not only the preamplifiers but also the digitizing and acquisition electronics are placed under vacuum near the detectors. As it is shown in fig. 2.1, the detectors are connected to the preamplifiers by kapton cables of about 15 cm length. The front end electronics (FEE) will be described in more detail in section 2.1.2.

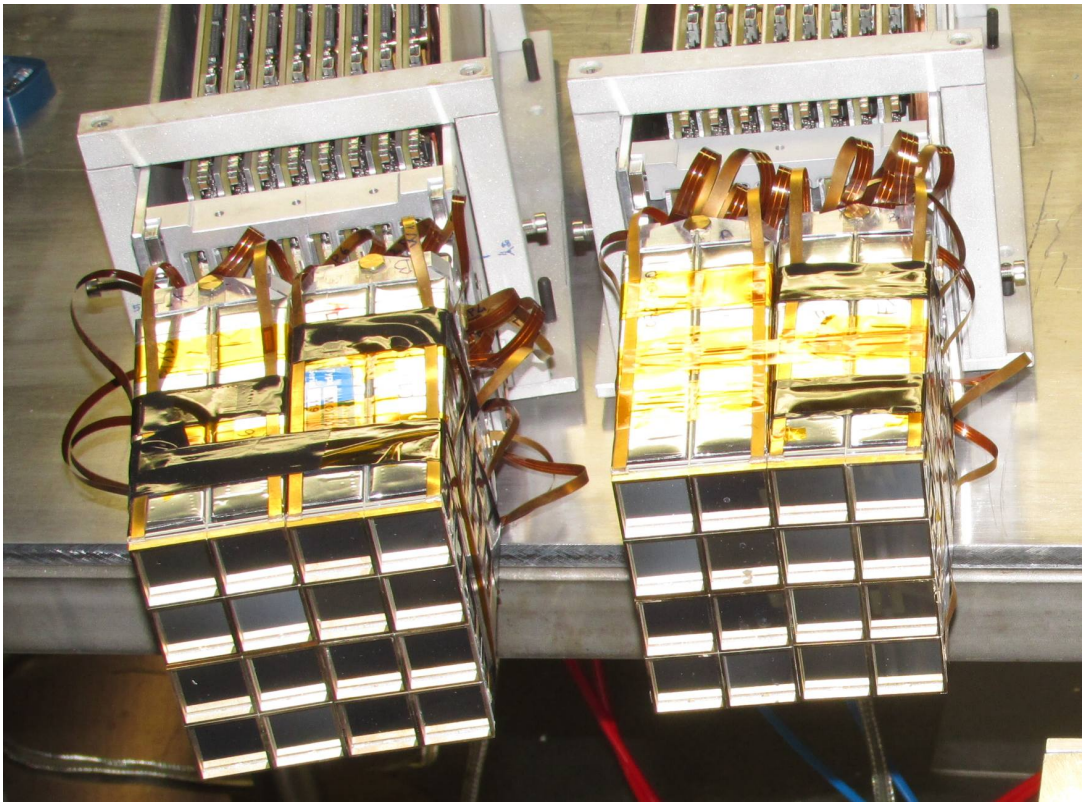

**Figure 2.1:** *FAZIA blocks mounted inside the Ciclope scattering chamber at LNS during ISO-FAZIA experiment in June 2015.*

FAZIA started its first experimental campaign using four blocks in Catania at LNS in 2015 with the ISO-FAZIA and FAZIA-SYM experiments, followed in 2017 by FAZIA-COR and FAZIA-PRE (scheduled for November 2017). Afterwards a complete demonstrator (composed of twelve FAZIA blocks, i.e. 192 ΔE-E telescopes) will be moved to GANIL (Caen, France) for a new campaign, and coupled with the INDRA detector [42]. The campaign is aimed at studying the multi-fragmentation and vaporization of the projectile at intermediate energy, up to 65 MeV/u. At GANIL, FAZIA will cover the forward angles in the laboratory reference frame, thus replacing part of the INDRA $4\pi$ detector array. A sketch of the INDRA-FAZIA apparatus setup as it will be settled in GANIL is shown in fig. 2.2.

### 2.1.1 The detector recipe

In this paragraph we want to summarize the construction criteria for Si detectors which have been identified during the R&D phase as a way to obtain good identification performance both in ΔE-E and in PSA (see [9] for more details):

- silicon detectors obtained from neutron transmutation doped (n-TD) ingots in order to optimize the dopant homogeneity;

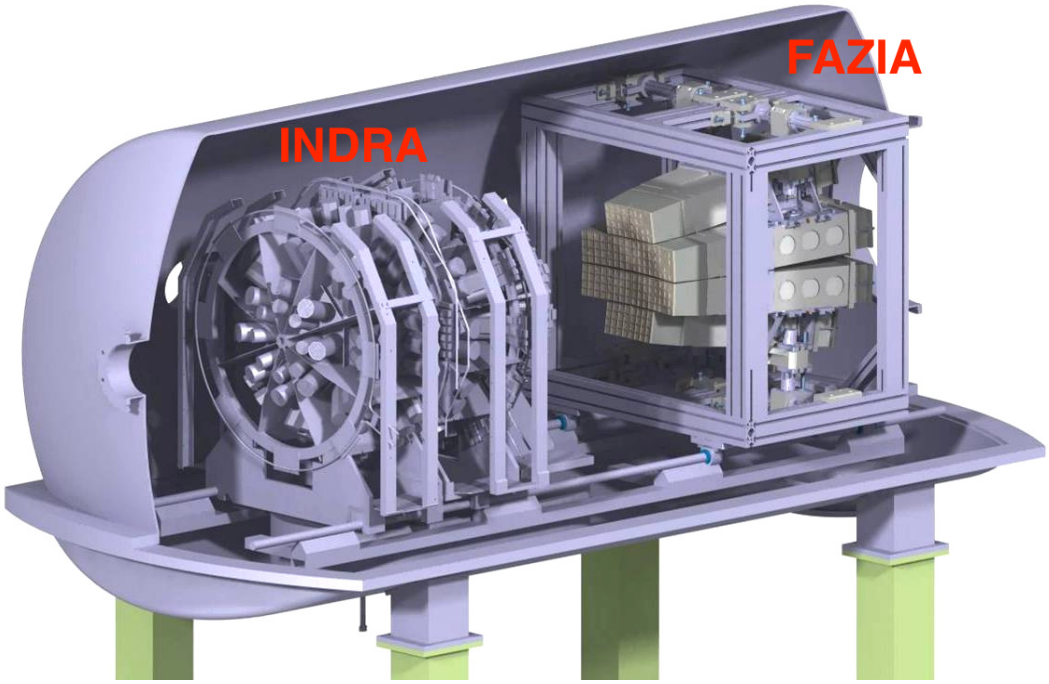


**Figure 2.2:** *Design for the coupling of the FAZIA demonstrator at forward angles (12 complete FAZIA Blocks) with the INDRA Four-π detector array.*

- silicon detectors with a thickness uniformity better than ±1 $\mu$m in order to reduce the dependence on the impact point of the energy $\Delta$E lost by a charged fragment punching through the detector;
- cut of the silicon wafers at about 7° with respect to the $< 100 >$ axis of the silicon lattice in order to minimize channeling effects [43][1];
- reverse mounting configuration of the silicon detectors (i.e. the charged fragments impinge on the low field side of the detector) to enhance the variation of the collection time with Z, A and E (as illustrated in [44]);
- deposition of a $\sim$ 30 nm thick Al layer on the detector electrodes in order to reduce the sheet resistance thus minimizing the dependence of the signal shape from the impact point, due to the electrode acting as a two dimensional transmission line (as explained in [45]);
- FEE placed in vacuum near the detectors in order to reduce noise and shape distortion associated to long cables;

[1]In PSA studies, we call "channeling effect" the increase in shape fluctuations (around an averaged shape) of the detector signals, for given Z, A and E, when the fragments impinge along one of the symmetry axis of the Si crystalline lattice.

- monitoring of the stability of the voltage applied to the detector and compensation for changes in bias current;
- optimization of the digital processing of detector signals, such as the recent development of a new interpolation algorithm applied to the current signal for a better extraction of pulse shape related parameters [11].

### 2.1.2 Front-End Electronics (FEE)

In the FAZIA block the connections between the detectors and the Front End Electronics (FEE) are kept short in order to avoid signal distortion due to the transmission through long cables and capacitive loading of the preamplifier input (the latter increasing the series noise contribution). Since the electronics operates under vacuum, a cooling system is required to keep the temperature of the electronic components below 50°C.

A sketch of the electronic acquisition system which stores detector signals on disk is shown in fig. 2.3.

For each block, the FEE electronics consists in 8 Digitizing Boards, a Block Controller board and a Power Supply board. Every Digitizing Board manages 2 telescopes. Each detection layer is connected to a single Charge Sensitive Preamplifier (CSP). After the CSP, the signals are processed as follows.

Among the telescope stages, Si1 is certainly the most important. In fact, its performance determines the quality of the ΔE-E and PSA identification, as well as

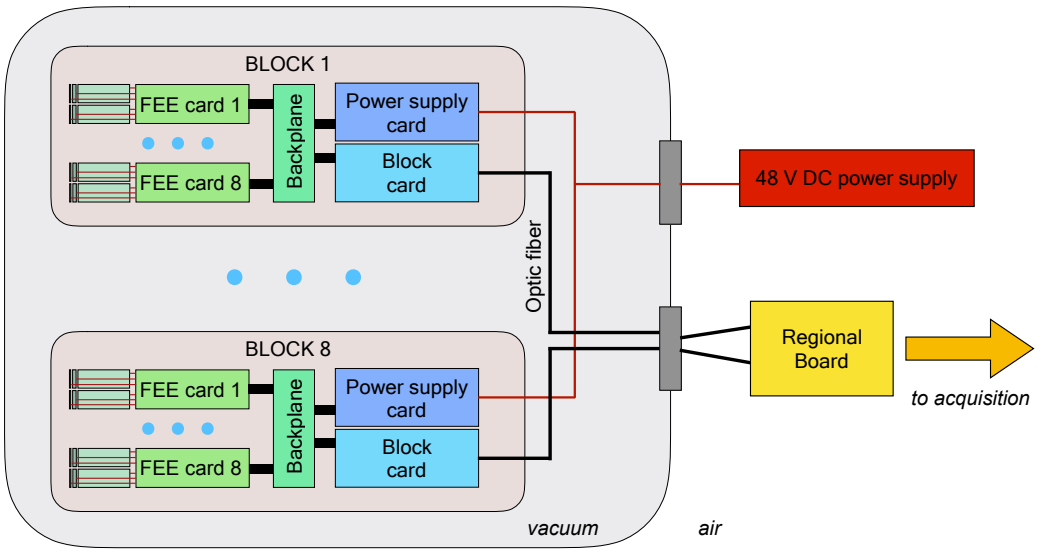


**Figure 2.3:** *Architecture of the FAZIA acquisition electronics from the detectors to the "regional" board, acting as data collector when more than one block is used.*

| Technical spec | QH1 | QL1 | I1 | Q2 | I2 | Q3 |
|---|---|---|---|---|---|---|
| Detector | Si1 | Si1 | Si1 | Si2 | Si2 | CsI(Tl) |
| Resolution (bit) | 14 | 14 | 14 | 14 | 14 | 14 |
| Sampling Rate (MSPS) | 100 | 250 | 250 | 100 | 250 | 100 |
| Effective Number of Bits | 11.4 | 11.2 | 11.4 | 11.4 | 11.2 | 11.4 |
| Signal Length (samples) | 1048 | 2048 | 512 | 1024 | 512 | 1024 |
| Measured Noise (LSB) | 1.8 | 7.6 | 14.4 | 1.8 | 12.3 | 2.0 |
| Full Scale (GeV) | 4 | 0.35 | - | 4 | - | |

**Table 2.1:** *Main features of the FAZIA FEE digitizing channels. QH1 and QL1: charge signal of Si1 with high and low energy range respectively (corresponding to low and high gain). Q2: charge signal of Si2. Q3: charge signal of the CsI detector. I1 and I2: current signals of Si1 and Si2, respectively. Signal length and noise values refer to the ISO-FAZIA experiment.*

that of the timing information. Since low amplitude signals could suffer from worse signal-to-noise ratio (SNR), the signal coming from Si1, after the CSP, is splitted and sent to two digitizing chains, with different gains. On the high range line (called QH1) the signal is attenuated by a factor of four and digitized at 100 MSPS (Mega Samples per Second) with 14 bit resolution and around 11.4 ENOB (Effective Number of Bits)[2]. On the low range line (called QL1) the signal is amplified by a factor of four and digitized at 250 MSPS at 14 bit resolution and 11.2 ENOB. Therefore, the dynamic range of the QH1 is 16 times larger than that of QL1. The higher sampling rate of QL1 is aimed at a better timing information. In order to obtain a current signal to be used for PSA, the CSP signal is sent on a third line (called I1) where it is differentiated by a high-pass filter and sampled at 250 MSPS with 14 bit resolution and 11.2 ENOB. The signals coming from Si2 are processed along a high range line (called Q2 and equivalent to QH1) and a differentiating line aimed at producing a current signal (called I2 and equivalent to I1). The signal coming from the CsI scintillator, after the CSP, is digitized at 100 MSPS with 14 bit resolution and 11.4 ENOB (this signal is called Q3). The main features of the different electronic channels are summarized in tab. 2.1. In this work the low dynamic range channel QL1 has not been used. Therefore, in the following with "charge signal of Si1" we always refer to the QH1 channel.

Each digitizing board is equipped with two programmable logic devices, FPGA (Field Programmable Gate Array). The FPGAs are devoted to acquisition and

[2]ENOB is a measure of the effective noise variance of an Analog-to-digital converter (ADC). In principle the dynamic range of an ADC is divided in $2^N$ signal levels determined by its number of bits ($N$). The error introduced in the digitizing process is usually described as a white noise contribution called quantization noise and it can be quantified as $\sigma^2 = \frac{R^2}{12*4^N}$ where R is the ADC range in Volt. However, the ADC analog input noise and the aperture time jitter also contribute to the total noise level of the ADC thus reducing its dynamic range. The effective ADC noise variance can be quantified as $\sigma^2 = \frac{R^2}{12*4^{ENOB}}$ where $ENOB < N$, typically $N - ENOB = 1 \div 2$.

storage of the digitized signals. They also apply a signal shaping algorithm on the digitized pulses produced by QH1, Q2 and Q3 in order to get the best SNR in estimating their amplitude (which in turn is related to the energy deposited in the detector). Data coming from the digitizing boards are collected and assembled in "event packages" by the "Block Card" (BC) which handles all the digitizing boards of a single block. From the BC, through an optic fiber, data are sent to a "Regional Board" (ReBo) placed outside the scattering chamber. The ReBo separates acquisition data from trigger information and sends back a validation signal to the BCs when a good event has been recognized (e.g. basing on particle multiplicity in the event). Acquisition data (i.e. signal shapes, shaper amplitudes, etc.) are written on disk for the offline analysis.

See [46, 47] for more details on the FEE architecture and the acquisition system.

## 2.2 Identification techniques

In order to identify the detected nuclear fragments, two identification techniques are employed: the ΔE-E technique and the Pulse Shape Analysis (PSA).

The ΔE-E technique is extensively used in detection systems for heavy-ion collisions thanks to its identification capability in charge and also in mass. It exploits the dependence of the specific energy loss of the fragment in the detector on its charge and mass (Bethe-Bloch formula [48]):

$$\left|\frac{dE}{dx}\right| = \frac{4\pi Z^2 e^4 N_{el}}{m_e \beta^2 c^2} B \tag{2.1}$$

where:

$$\beta = \frac{v}{c}\ ,\ N_{el} = \rho\frac{N_{Av} Z_{abs}}{A_{abs}} \quad \text{and} \quad B = \left[\ln\left(\frac{2m_e v^2}{I}\right) - \beta^2 - \ln\left(1 - \frac{v^2}{c^2}\right)\right]$$

$Z$ is the projectile atomic number, $N_{Av}$ is the Avogadro number, $N_{el}$ is the electron density in the absorber whose atomic and mass number are $Z_{abs}$ and $A_{abs}$ respectively, $m_e$ and $e$ are the electron rest mass and charge, $I$ is the average ionization potential of the absorber.

For non relativistic heavy ions, the previous equation gives:

$$\left|\frac{dE}{dx}\right| \propto \frac{Z^2}{\beta^2} \propto \frac{Z^2 A}{E} \tag{2.2}$$

where $E$ is the kinetic energy of the fragment.

As one can deduce from eq. (2.2), for a ΔE-E telescope, the energy loss in the detector (especially the ΔE) depends from the product $Z^2 A$ of the fragment and it

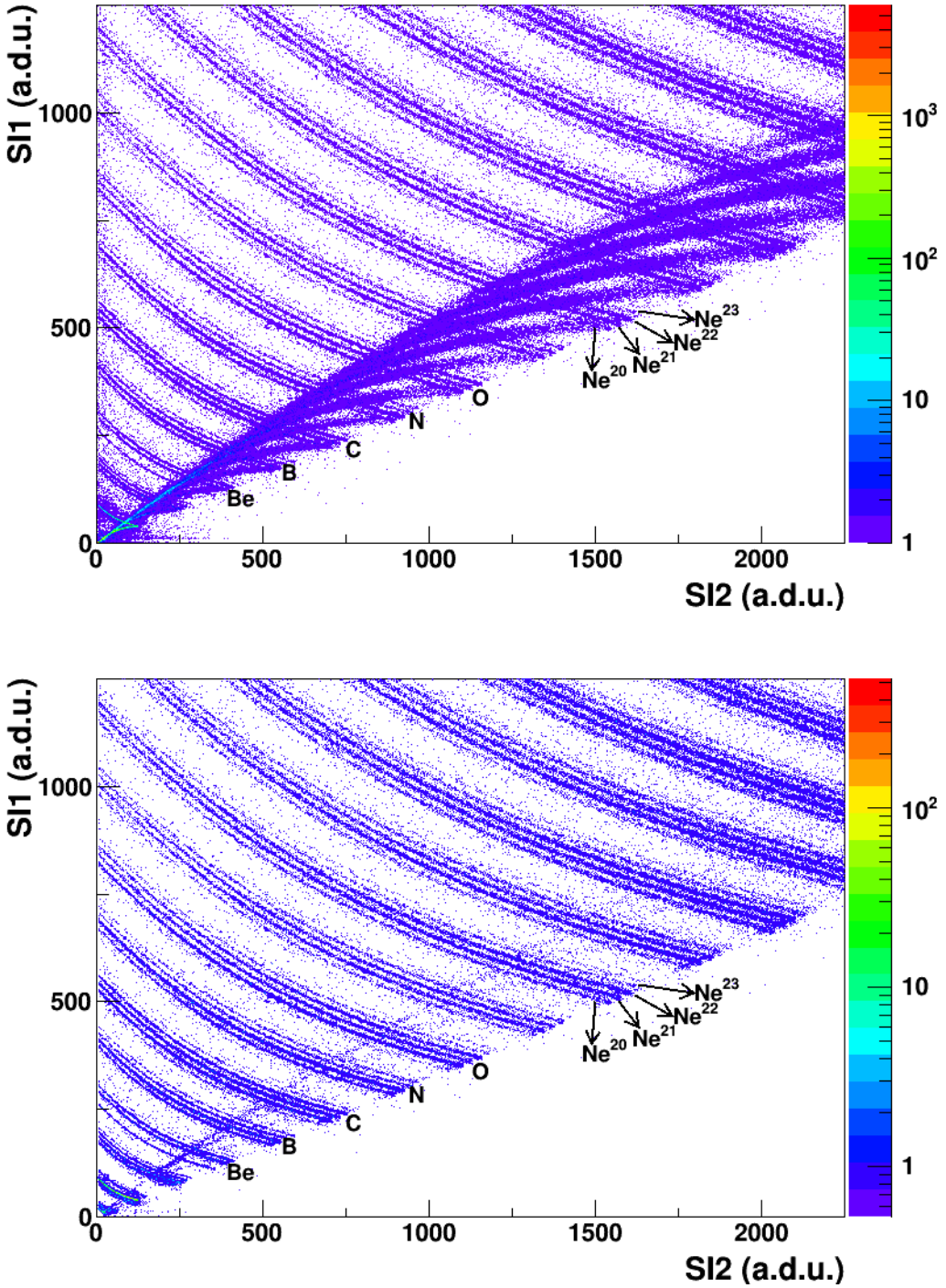


**Figure 2.4:** *$\Delta$E-E matrix correlation between the energies deposited in Si1 and Si2. The data are taken from the ISO-FAZIA experiment. The bottom panel shows the same correlation in the top panel with the veto condition of the third layer of the FAZIA telescope (CsI scintillator) to reject punching through particles.*

decreases increasing the energy E of the incident fragment. Correlating the energies deposited by a charged fragment in two consecutive detectors we obtain a "$\Delta$E-E

matrix" as shown in figure 2.4 for Si1-Si2 correlation. The loci associated to different Z value are well separated and, due to the good resolution of the telescope, the fine structure due to the different A values (different isotopes of the same element) is also apparent.

For each detector, we define the "punch through" energy as the energy for which the range of the fragment in the detector is equal to its thickness. It follows that the energy of the fragments identified by the ΔE-E correlation must be higher than the punch through energy in the first detector and lower than the punch through energy in the second. Fragments with energy greater than the punch through energy of the second layer produce a cusp on the right of the curve which degrades the identification capability of the method, as it is shown in the top panel of fig. 2.4. This effect can be avoided, as it is shown in the bottom panel of fig. 2.4 in which only a small amount of punch through contamination is observable, exploiting the energy information of a third detection layer (CsI scintillator in our case).

The punch through energy in the first detector sets the energy threshold for identification. To minimize this lower limit, the first layer of the telescope should be as thin as possible. However, a small thickness gives a worse performance when it comes to Signal-to-Noise Ratio (SNR)[3] and energy straggling[4].

Since it exploits the information coming from a single detector, the PSA applied to Si1 (the first telescope layer) was chosen by the FAZIA Collaboration as a way to reduce the energy identification thresholds.

First proposed by Ammerlaan [49] more than fifty years ago, the PSA technique has greatly benefited from the availability of fast sampling digitizers [44, 50–54]. In fact, it is easier and cheaper to apply PSA to digitized signals with respect to analog signals. PSA exploits the different shapes of the signals produced by fragments with different Z and A, due to the process of collection of the carriers inside the detector. The carrier (i.e. electron-hole pairs) density of the ionization track produced by a fragment stopped in a Si detector follows the so-called "Bragg curve" which has a peaked shape as a function of the penetration depth with its maximum towards the end of the track. The carrier density along the track is so high (especially for $Z > 3$) that it can behave like a plasma of positive and negative charges. The electric field which is present in the depletion region needs some time to put all the carriers into motion (the so-called "plasma time" [55–57]). Moreover, the electric field decreases going from the junction side to the opposite side of the depletion region,

[3] A thinner detector produces a smaller amplitude signal. Moreover, the Si detector p-n junction has a higher capacitance, thus enhancing the series noise component due to the input transistor of the CSA. The combined effect is a reduction of the SNR.

[4] The energy loss process is a statistical phenomenon and is affected by an intrinsic fluctuation called *straggling* which can become the dominant limit of the ΔE-E technique. In fact, the relative uncertainty due to the energy straggling increases for a decreasing detector thickness.

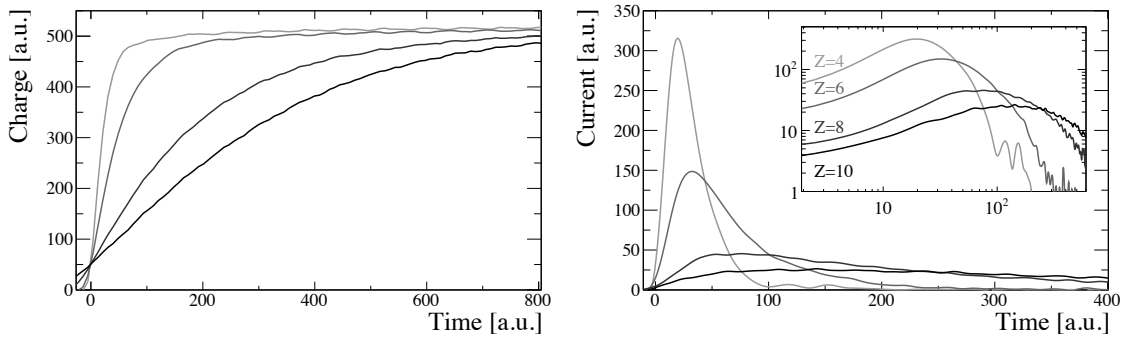


**Figure 2.5:** *Experimental signals coming from Si1 for different isotopes ($Z = 4, 6, 8$ and 10) at 95.5 MeV. In the left (right) panel the acquired charge (current) signals are shown. The inset in the right panel shows and expanded view in semilogarithmic scale. From Ref. [58].*

so that the intensity of the field near the Bragg peak depends on the fragment penetration (i.e. its "range") into the detector. For all these reasons, the current flowing in the detector and the collection time depend on Z, A and energy (E) of the fragment, as well as on the detector characteristics (applied voltage, thickness, resistivity, etc...). Some example signals coming from Si1 and corresponding to different isotopes ($Z = 4, 6, 8, 10$) at same energy (95.5 MeV) are shown in fig. 2.5. The signal shapes are very different and dependent on the fragment type.

To increase the PSA performances, it is important to reduce shape variations (for given Z, A and E) from event to event. Therefore, the Si wafers are cut in such a way as to reduce the probability of "channeling" of the impinging particles. A good uniformity of the electric field (and therefore of the resistivity of the bulk, which can be measured using the technique described in [59]) along the detector surface is also mandatory for good results. Moreover, the detector bias must be kept constant during the measurement, e.g. correcting for variations of the leakage current which affect the applied voltage through the voltage drop on the bias resistor.

Electronic noise can also limit PSA performance at low incident energy. Last but not least, an intrinsic limit to PSA identification is associated to the "range straggling" phenomenon, i.e. the variation in track length (for fixed Z,A, and E) due to the stochastic nature of the energy loss process.

Two different PSA approaches were extensively investigated by the FAZIA collaboration:

- the correlation between the energy deposited in the silicon detector and the risetime of the charge signal (*PSA(Q)* in the following) as shown in fig 2.6;
- the correlation between the energy deposited in the silicon detector and the maximum amplitude of the current signal (*PSA($I_{max}$)* in the following) as shown in fig 2.7.

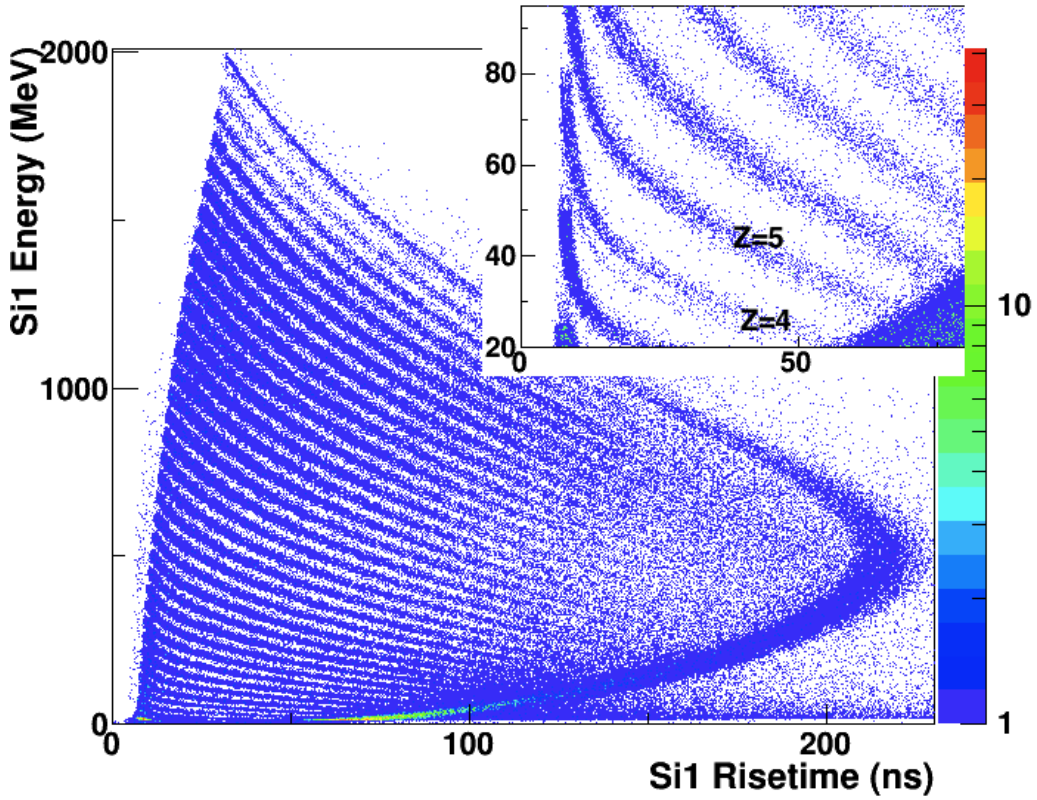


**Figure 2.6:** PSA(Q) *correlation with Energy measured by Si1 vs Risetime of the charge signal. All the elements from hydrogen to kripton are identified in Z. In the inset we show an expanded view of the low Z region from Li to N. A hint of isotopic resolution is present just for* $Z = 5$ *for a risetime between 15 and 30 ns.*

The lower energy thresholds for identification with the two PSA techniques were investigated in a previous work [60], where the prototype version of the FEE was used. They were found to be quite similar (see Fig.17 of Ref. [60]). In the ISO-FAZIA experiment we employed for the first time in a physics experiment a complete FAZIA block, including the new FEE electronics. The new FEE cards feature a higher sampling rate on the current channel, allowing for better performance of $PSA(I_{max})$. A great effort was done also to improve the signal processing on the current signal to exploit as much as possible the identification capabilities of the $PSA(I_{max})$. The details of the recent developments in the PSA technique obtained in this work are presented in Sec 2.3.

The PSA technique can be applied also to the CsI detector. In fact, the light intensity emitted during the scintillation process as a function of time can be modelled as the sum of two exponentials with different time constants ("fast" and "slow" with respective decay time of 700 ns and 2 $\mu$s). The ratio of the two components, as well as the value of the fast time constant, depend on Z, A, and E of the impinging

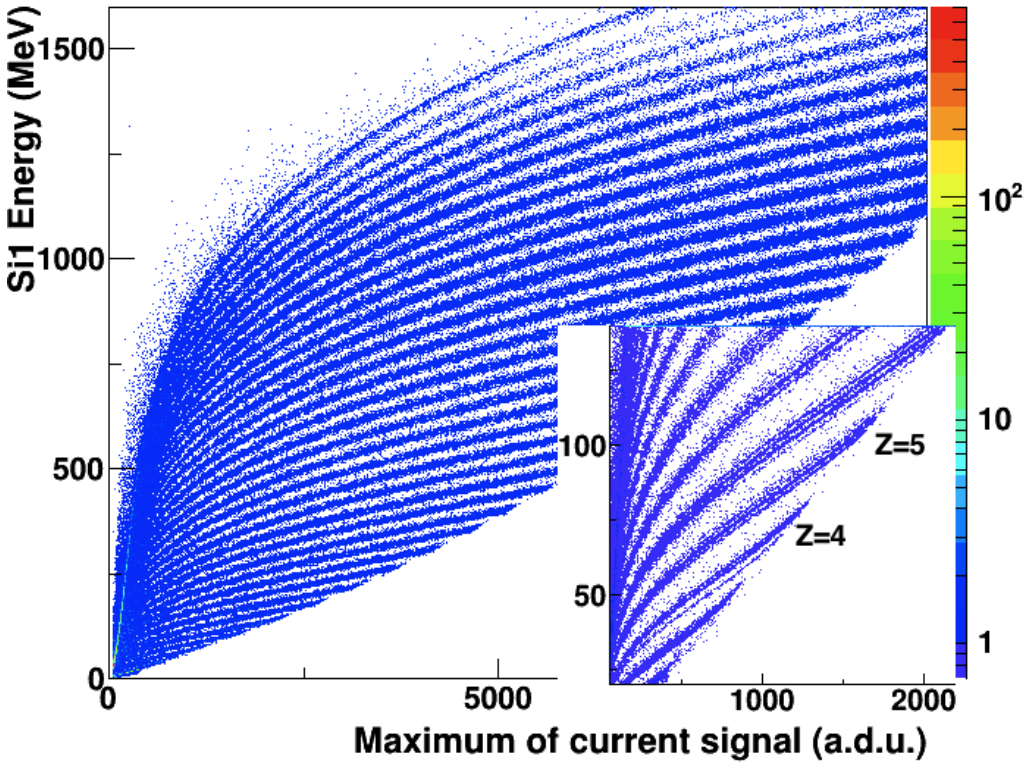


**Figure 2.7:** PSA($I_{max}$) *correlation with Energy measured by Si1 vs Maximum of current signal. All the fragments from hydrogen to kripton are identified in Z. Also the isotopic resolution is achieved up to* $Z \sim 20$ *for an energy between* 715 *and* $900 MeV$. *In the inset we show an expanded view of the low region for a better appreciation of the good isotopic resolution obtained.*

fragment. It is possible to resolve the fast and slow information by treating the detector signal with two shapers with different time constants. Moreover, integrating for longer time, the slow shaper includes also the fast scintillation contribution consequently correlating the two components. An example of a *Fast-Slow* correlation is shown in fig. 2.8 in which is possible to identify the mass number at least up to $Z$ = 4-5. In the figure the fast component is reported as a function of the variable $Slow - 0.9 * Fast$ in order to enhance the isotopic separation between the different lines.

### 2.2.1 Charge signal processing

Both the ΔE-E and the PSA identification methods require a precise energy measurement in order to obtain isotopic resolution. In ISO-FAZIA, 1024 samples (corresponding to $\approx 10\,\mu$s of signal length) are acquired for the charge signal and stored for offline processing. Using a pre-trigger portion of the signal, stored in a circular

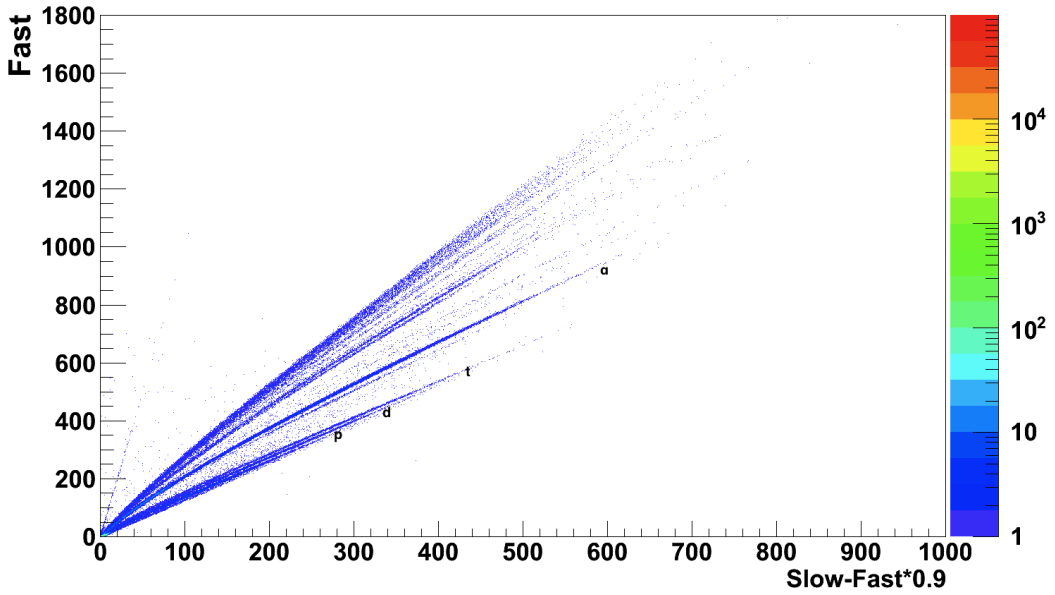


**Figure 2.8:** *Correlation between the Fast component and the difference between Slow component and a fraction of Fast component of charge signal produced in CsI detector.*

buffer, evaluation and subtraction of the baseline from the digitized signal is possible [61]. The pre-trigger length was set to 640 samples ($\approx 6\,\mu$s). After baseline subtraction, the signal is shaped by means of a trapezoidal digital filter. The charge signal rise-time depends on the type of the impinging fragment and on its energy. To avoid ballistic deficit, we adjusted the parameters of the filter to cope with the slowest acquired signals. Since the maximum measured rise-time is $\approx 250$ ns, we use $1\,\mu$s as the flat-top duration of the trapezoidal shaper and $2\,\mu$s as the rise-time. The latter determines the bandwidth of the filter and therefore the final SNR. No pole-zero cancellation was applied to correct for the exponential decay of the preamplifier signal. In fact, its effect would be negligible due to the long preamplifier decay constant ($\sim 260\,\mu$s) with respect to the length of the flat top. The deposited energy is evaluated from the maximum value of the output of the trapezoidal filter. In the case of charge signal coming from CsI two different trapezoidal filters have been used to estimate the different components, *Fast* and *Slow*, of its shape. The fast trapezoidal filter has $0.7\,\mu$s and $0.5\,\mu$s of rise-time and flat-top respectively while the slow trapezoidal has $2\,\mu$s of rise-time and $10\,\mu$s of flat-top. The treatment of the current channel deserves a dedicated section (see Sec. 2.3) in order to illustrate the recent developments aimed at optimizing the PSA identification capability.

## 2.3 Recent improvements in PSA technique

To enhance the identification capability of the *PSA($I_{max}$)* correlation, taking also advantage of the better performance of the new FEE cards, in the framework of this work, we improved the offline processing of the current signal [11]. For the determination of the maximum value of the current signal ($I_{max}$), two main points have emerged as crucial: the need for interpolation, in order to reconstruct the actual maximum of the original signal (i.e. before sampling) and the need to apply low-pass filtering to reduce the noise fluctuations superimposed on the sampled signal.

Interpolation and noise are related issues. The power spectrum of a current pulse decreases monotonically with frequency while the superimposed noise has an almost white power spectral density. Therefore, electronic noise is relatively more important close to the Nyquist frequency[5], where artifacts due to the reconstruction can either enhance or attenuate its importance. In fact, different interpolation methods add different amounts of high frequency components to the reconstructed signal (see Fig. 3.14 of Ref. [62]).

### 2.3.1 Interpolation

Interpolation allows for a reconstruction of the original analog signal from its acquired samples. The importance of applying an interpolation procedure on the current signal to enhance the isotopic resolution of the *PSA($I_{max}$)* correlation has been already evidenced in previous works [63, 64]. In this work, the need of the interpolation procedure in order to get the best isotopic resolution, even after the reduction in sampling period on current signal from the 10 ns value of the prototypes to the 4 ns of the new FAZIA FEE card, has been recognized.

We tested different cubic interpolation algorithms using in all cases a factor 10 of upsampling (i.e. the sampling period of the interpolated signal is equal to 0.4 ns), to compare the obtainable isotopic resolution via *PSA($I_{max}$)*. In particular we tested:

- the algorithm described in Ref. [64], based on the unique third order polynomial curve, passing through four consecutive samples which is used to interpolate in the interval in between the second and third sample. We call this algorithm *Cubic interpolation*;
- a cubic spline interpolation [65] which produces a composite curve, passing through the samples, obtained by piecewise joining third order polynomials. At the sampling points, the curve is continuous up to its second order derivative. The main features of the algorithm are reported in Sec. 2.3.2 together with a

[5] In this context we call Nyquist frequency half the sampling rate of the ADC.

short explanation of the computational details. We call this algorithm *Spline interpolation*;

- a smoothing spline interpolation algorithm [66] based, as the previous one, on spline curves continuous up to the second derivative. This algorithm is not an interpolation in the strict sense, since the interpolated signal does not necessarily pass through the original samples. The algorithm incorporates a smoothing procedure to reduce the noise fluctuations. A "noise reduction" parameter $l$ controls the tradeoff between similarity to the original signal and reduction of the noise fluctuations: in the following we use $l = 1$. The main features of the algorithm are reported in Sec. 2.3.2 together with a short explanation of the computational details. We refer to this algorithm as *SmSpline interpolation*;

### 2.3.2 Splines and Smoothing Splines

The cubic splines interpolation algorithm consists in finding a member $g(t)$ of the cubic splines function family that passes through all the samples of a sequence $x[n]$. The family of cubic splines is the set

$$K(f,\, T_s) = \left\{ g(t) \mid g(t) = \sum_{m=-\infty}^{+\infty} c_m\, f(t/T_s - m) \right\}$$

where $T_s$ represents the sampling period of the sequence and $f(t)$ is a cubic box-spline interpolation kernel [65]. For a finite length signal, for each sampled value $x[n]$ we require $g(nT_s) = x[n]$ thus getting a linear system with the $c_m$ coefficients as unknowns. The coefficients $c_m$ should therefore be obtained by solving a linear system of order equal to the total number of samples in the signal. In order to reduce the calculation time, in this work we used an approximated algorithm which is however good enough for our applications. In fact, it allows us to solve a reduced linear system of order 17 while at the same time keeping the absolute error below $\Delta \sim 10^{-5}$ LSB (Least Significant Bits), usually lower than the noise fluctuations present in real signals.

If we define a quantity

$$D = \sum_{k=-\infty}^{\infty} \left(x[k] - g(kT_s)\right)^2 \tag{2.3}$$

as an estimator of the "closeness" to the sequence, the coefficients obtained as previously described guarantee that $D = 0$. In fact, one could determine the $c_m$ coefficients as those values which minimize the positively defined quantity $D$. However,

the constraints of having a cubic spline function passing through all samples (i.e. $D = 0$) and continuous up to the second derivative, are known to generate artifacts such as ringing and over/under-shoots in presence of noise or fast transients. To overcome these problems, the smoothing spline interpolation is used [66]. This algorithm minimizes the quantity

$$D = \sum_{k=-\infty}^{\infty} (x[k] - g(kT_s))^2 + l \int_{-\infty}^{\infty} \left| \frac{d^2}{dt^2} g(t) \right|^2 dt \tag{2.4}$$

The second term introduces the smoothing effect. By changing the value of the parameter $l$, the relative weight of the two conditions is changed. Due to the smoothing term it is impossible to achieve $D = 0$ (unless the sequence is $x[k] = Ak$), so the minimization process produces a cubic spline function which does not necessarily pass through all the samples. Actually, with respect to the cubic splines interpolation, the smoothing splines interpolation introduces a low pass filtering, which is similar to the effect obtained by using a moving average filter prior to cubic spline interpolation.

### 2.3.3 Noise reduction

We have found that by applying a noise reduction algorithm we can obtain a better estimate of $I_{max}$, thus getting better isotopic resolution from PSA($I_{max}$). This can be obtained either by means of a simple moving average algorithm, applied before interpolation, or as part of the interpolation itself (e.g. using the smoothing spline interpolation algorithm).

The electronic noise on the current channel, I1, is dominated by the contribution coming from the preamplifier before being sampled by the ADC. In fact, an ADC with 11.2 ENOB and 14 bit resolution (these are the features of ADC used to current signal digitization) is expected to contribute noise with a standard deviation $\sim$ 2 LSB while our measured value, determined on the signal baseline, is much larger, $\sim$ 14.4 LSB. The power spectral density of noise, also determined using the baseline, is flat, i.e. after digitization the noise of the signal is practically white.

The moving average is a Finite Impulse Response (FIR) filter which is optimal for reducing the white noise superimposed on the signal, while at the same time keeping the sharpest step response (see [67] page 278). In order to produce the n-th sample of its output sequence, $y[n]$, the moving average filter evaluates the average amplitude of M samples around the n-th sample of the input sequence $x[n]$. For a *causal* moving average $y[n] = \frac{1}{M} \sum_{i=0}^{M-1} x[n-i]$. In the frequency domain, the moving average acts as a low-pass filter. In the time domain, it has a smoothing action on

the signal [67]. After optimization of the filter in our particular application, a value $M = 4$ has been selected, thus obtaining a reduction of the standard deviation of noise on current signal from 14.4 to 4.0 LSB (see inset of Fig. 2.9).

### 2.3.4 Comparison between different processing

The effect of the processing applied to the current signal is shown in Fig. 2.9. The original signal, generated by a carbon fragment of 370 MeV incident energy, is represented by full circles. The time $T_{over}$ spent over a given fraction of the maximum is a useful way to quantify the changes in the reconstructed signal, since it takes into account not only the slowing down of the transients but also the reduction of its amplitude. Choosing a threshold of half the maximum value, we get $T_{over} = 16$ ns after reconstruction by cubic interpolation, without any noise reduction applied and

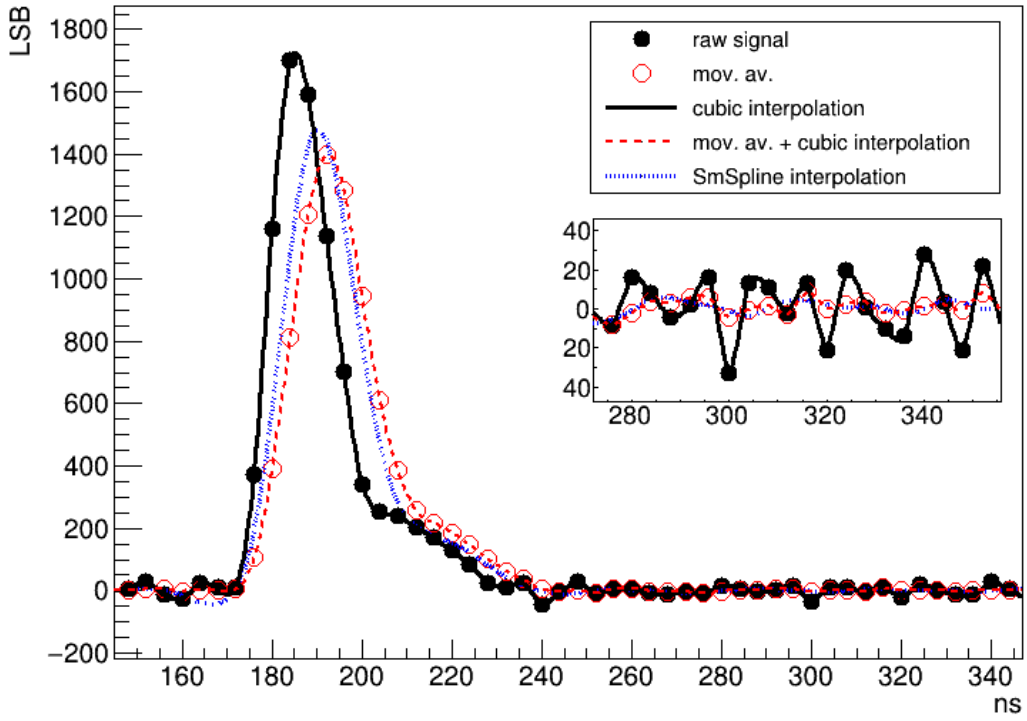


**Figure 2.9:** *Current signal for a carbon ion of 370 MeV energy. The baseline has been subtracted. Full black circles: samples of the original current signal. Open red circles: samples of the same signal after applying the moving average filter. Ten times upsampled signals, obtained by cubic interpolation, are shown as lines passing through the samples: continuous black line for raw samples and dashed red line for samples after the moving average. The dotted blue line refers to the signal obtained by SmSpline interpolation with ten times upsampling.*

10-time upsampling (continuous line passing through the full circles in Fig. 2.9). After applying the moving average filter (open circles in Fig. 2.9), the cubic interpolated signal has a $T_{over} = 20\,\text{ns}$ (dashed line in Fig. 2.9). The moving average filter modifies the shape of the current signal, reducing the amplitude and slowing down the transients. The smoothing spline interpolation (dotted blue line in Fig. 2.9), also shows a smoothing behavior, similar to that of the moving average ($T_{over} = 20\,\text{ns}$). The inset in Fig. 2.9 shows a portion of the signal baseline on an expanded amplitude scale: the reduced noise fluctuations when either the moving average or the Smoothing Spline interpolation are used in the processing chain are apparent.

In order to estimate quantitatively the performance of the different processing algorithms, as in previous works of the collaborations (see for instance [43]), we built the so-called PID (Particle Identification) spectra. Figure 2.10 is an example of a PID spectrum obtained using the *PSA(*$I_{max}$*)* correlation of Fig. 2.7. PID is a continuous variable which can be associated to any detected ion in such a way that the PID values associated to the isotopes of element Z never overlap the PID values of isotopes having atomic number Z±1. First, any of the finer curved lines present in correlations like the one of Fig. 2.4 or 2.7, is assigned with a PID value, which is a function of the Z and A values pertaining to the various lines, known or guessed. Once this assignment is performed, the curved lines associated to each PID value

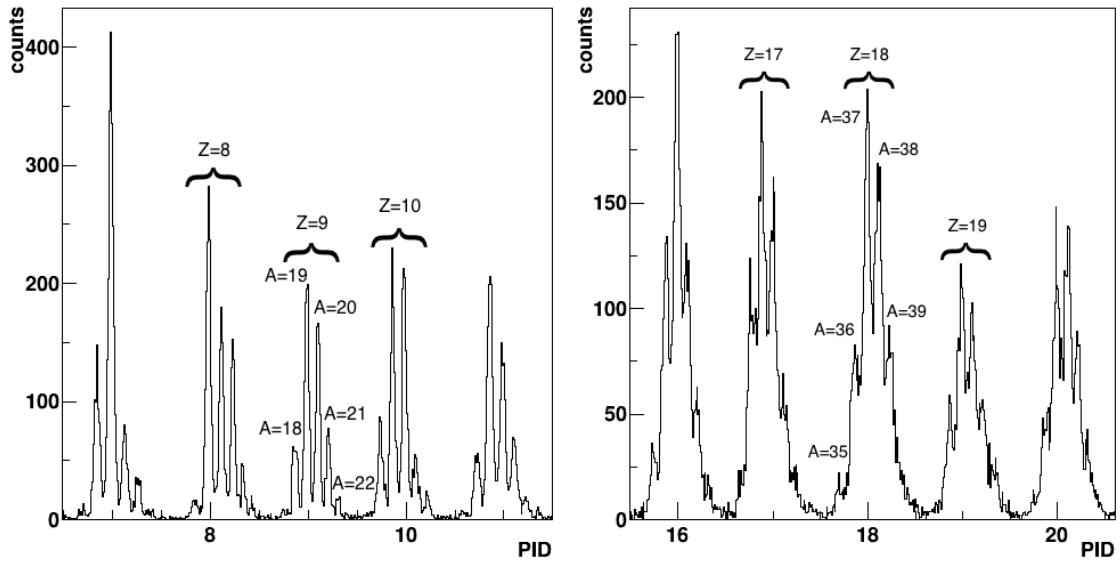


**Figure 2.10:** *PID distributions, integrated on the energy range where the isotopic resolution is achievable, obtained from the* PSA($I_{max}$) *correlation of Fig. 2.7. Left panel: PID spectrum for ions from Nitrogen up to Sodium. Right panel: fragments from sulphur to calcium.*

can be transformed into straight lines running parallel to the energy axis. Typically this *linearization* is obtained by graphically drawing the lines corresponding to the same PID over correlations like the one in Fig. 2.7. In the data analysis, the PID value of any detected fragment not exactly lying on the PID curves is assigned via an interpolation based on the distance of its $I_{max}$ (or energy in case of $\Delta$E-E matrix) and energy coordinates from the closest graphical PID lines. The resulting correlation thus presents straight horizontal PID lines with finite width, each belonging to ions with unique Z and A values. The projection on the PID axis gives the energy integrated PID spectra. In Fig. 2.10 we present an example of the PID distribution obtained from the $PSA(I_{max})$ correlation of Fig. 2.7.

A multi-gaussian fit is then applied to the isotopic peaks associated with each element and a FoM [68] can be evaluated for pairs of adjacent peaks. The FoM is defined as:

$$FoM = \frac{PID_2 - PID_1}{FWHM_2 + FWHM_1} \tag{2.5}$$

where $PID_2$ and $PID_1$ are the centroids of two adjacent peaks in the PID spectrum and $FWHM_2$ and $FWHM_1$ their respective widths.

Figure 2.11 shows a multi-gaussian fit performed on the isotopic peaks for Oxygen. The left and right panels refer respectively to interpolation without and with a preceding moving average filtering. The dotted red line in the left panel (marked $I_{raw}$ in the legend) has been obtained from an analysis in which neither an interpolation nor a noise reduction algorithm have been applied before extracting the maximum of the current signal. By comparing it to the other curves in the same panel, it is clear that interpolation is still needed for a good fragment separation, in spite of the increased sampling frequency on the current channel in the new FAZIA FEE. The general improvement of the isotopic resolution obtained by using a noise reduction algorithm is evident from the comparison of the curves in the two panels: the peak to valley ratio for a given interpolation algorithm, and even for no interpolation, improves after noise reduction. Moreover, the SmSpline interpolation appears to give even better results than the moving average followed by interpolation.

To get a more quantitative indication, we evaluated the FoM for three representative isotopic pairs, corresponding to fragments stopped in Si1: $^{16,17}$O, $^{25,26}$Mg, $^{33,34}$S. Our analysis is limited to the energy interval where the isotopic identification is achievable with the $PSA(I_{max})$ correlation. In fact (see inset of Fig. 2.7) the isotopic resolution is not achieved in the entire energy range of a "Z-line". Only fragments with energy higher than certain thresholds (e.g. 130 MeV for $^{16,17}$O, 175 MeV for $^{25,26}$Mg and 235 MeV for $^{33,34}$S) and lower than the punch through energy are taken into account.

The FoM obtained from $PSA(I_{max})$ correlation for the chosen isotopic pairs are reported in Table 2.2. A conventional reference value, above which one considers

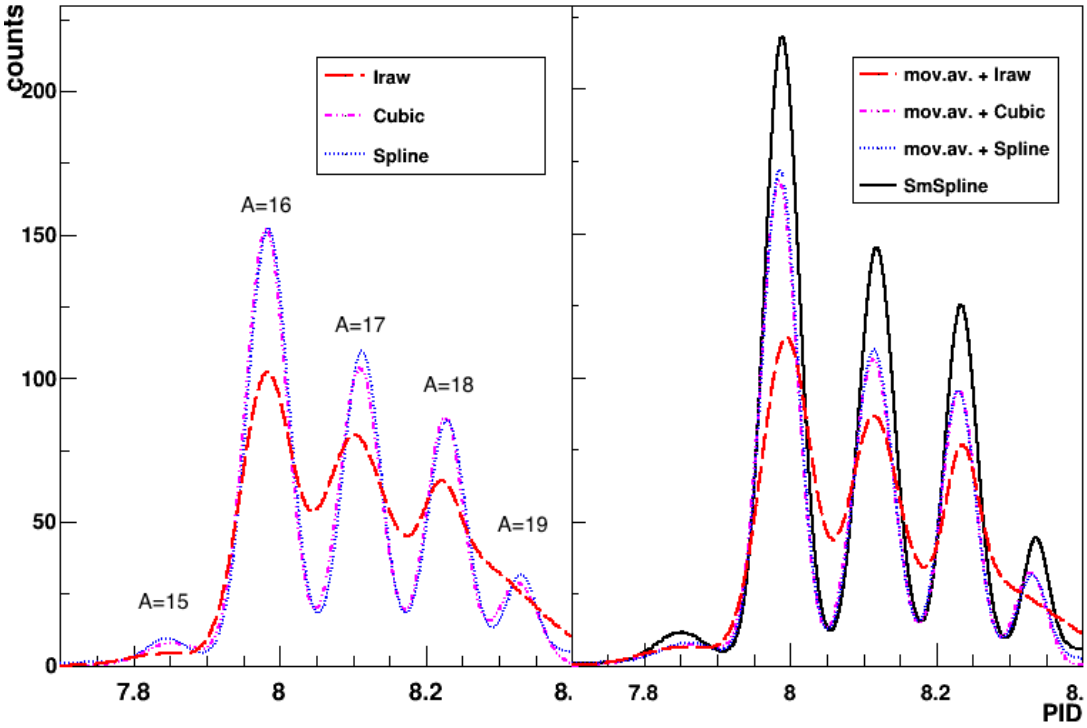


**Figure 2.11:** *Multi-gaussian fit results for Oxygen isotopes as obtained on the PID spectra. The studied interpolation algorithms are compared with the raw data results. Left (right) panel: results obtained without (with) the application of the moving average filter (m.a.).*

| Current processing | FoM $^{16,17}O$ | $\chi^2_{red}$ | FoM $^{25,26}Mg$ | $\chi^2_{red}$ | FoM $^{33,34}S$ | $\chi^2_{red}$ |
|---|---|---|---|---|---|---|
| $I_{raw}$ | 0.65±0.06 | 1.12 | 0.53±0.09 | 1.38 | - | - |
| m.a. + $I_{raw}$ | 0.75±0.04 | 1.15 | 0.63±0.04 | 1.10 | - | - |
| Cubic | 0.96±0.02 | 1.17 | 0.83±0.03 | 1.24 | 0.66±0.04 | 0.99 |
| m.a. + Cubic | 1.04±0.03 | 1.58 | 0.88±0.03 | 1.28 | 0.71±0.04 | 1.25 |
| Spline | 1.01±0.03 | 0.96 | 0.83±0.03 | 1.01 | 0.69±0.05 | 0.94 |
| m.a. + Spline | 1.08±0.03 | 1.31 | 0.91±0.03 | 1.17 | 0.72±0.04 | 0.97 |
| SmSpline | 1.15±0.02 | 1.15 | 0.90±0.02 | 1.21 | 0.72±0.04 | 0.99 |

**Table 2.2:** *FoM values and associated reduced $\chi^2$ as obtained from the multi-gaussian fit. The results are reported for no interpolation on current signal ($I_{raw}$), for cubic interpolation (Cubic), for spline interpolation (Spline) and for Smoothing Spline interpolation (SmSpline). Furthermore we report FoM and reduced $\chi^2$ for the same interpolation algorithms when a four-sample moving average filter (m.a.) is applied to the signal before interpolation.*

two peaks as well separated, is FoM= 0.7 corresponding to a peak-to-valley ratio of 2 when the two peaks have equal areas [43]. The FoM values for $I_{raw}$ (maximum of current signal without any digital processing) are all below 0.7. By applying a moving average and no interpolation, the FoM value for the $^{16,17}$O pair rises above the 0.7 level. For sulphur, the isotopic peaks in the PID distribution are not even distinguishable, so that the FoM was not estimated. It is thus confirmed that interpolation is needed in order to get a better separation. Using interpolation, the obtained FoM are higher than 0.7 for all the chosen pairs except for sulphur, for which all FoM values are anyway compatible with 0.7 within the experimental errors. The Cubic and Spline interpolation give practically the same performance.

The moving average filter improves the FoM regardless of the interpolation algorithm. The SmSpline does not require the use of the moving average filter because of its intrinsic smoothing process. It is worth stressing that the best results in terms of identification capabilities are obtained using the SmSpline interpolation algorithm.

### 2.3.5 Energy threshold

To define the energy thresholds we apply the same procedure based on FoM proposed in Ref. [43]. First we produce the PID vs Energy correlation, then we subdivide it into consecutive energy intervals and for each of them we project the data on the PID axis by integrating the event density over the energy interval. We thus obtain the PID distribution spectra relative to each interval. To get the energy threshold for element identification, we evaluate the FoM for each element pair considered on the PID distribution spectra, obtained by integrating over 5 MeV wide intervals. The lowest threshold for identification is therefore determined as the energy above which the two peaks have a FoM greater than 0.7. The used width of the integration energy interval, i.e. 5 MeV in the present case, gives the uncertainty on the energy threshold associated with element separation. To perform the same analysis for isotopic separation, in order to have enough statistics in the spectra, we use wider intervals: 15 MeV up to $Z = 14$ and 25 MeV for $Z > 14$ fragments which correspond to the uncertainty in the evaluation of isotopic threshold.

In Fig. 2.12 we report the obtained results, compared with the isotopic identification threshold for the ΔE-E method. The energy thresholds for element identification quoted in Ref. [60] are also reported, for sake of comparison.

Our values are similar, though slightly worse for high Z fragments, to those of Ref. [60]. A possible explanation of the observed discrepancy could be the sizeably worse doping homogeneity of the detector used in this work ($\sim 3-6\%$ instead of 0.6% of Ref.[60]). The energy thresholds for isotopic identification, for fragments with $3 \leq Z \leq 19$, are also plotted in Fig. 2.12, right panels. In the left panel

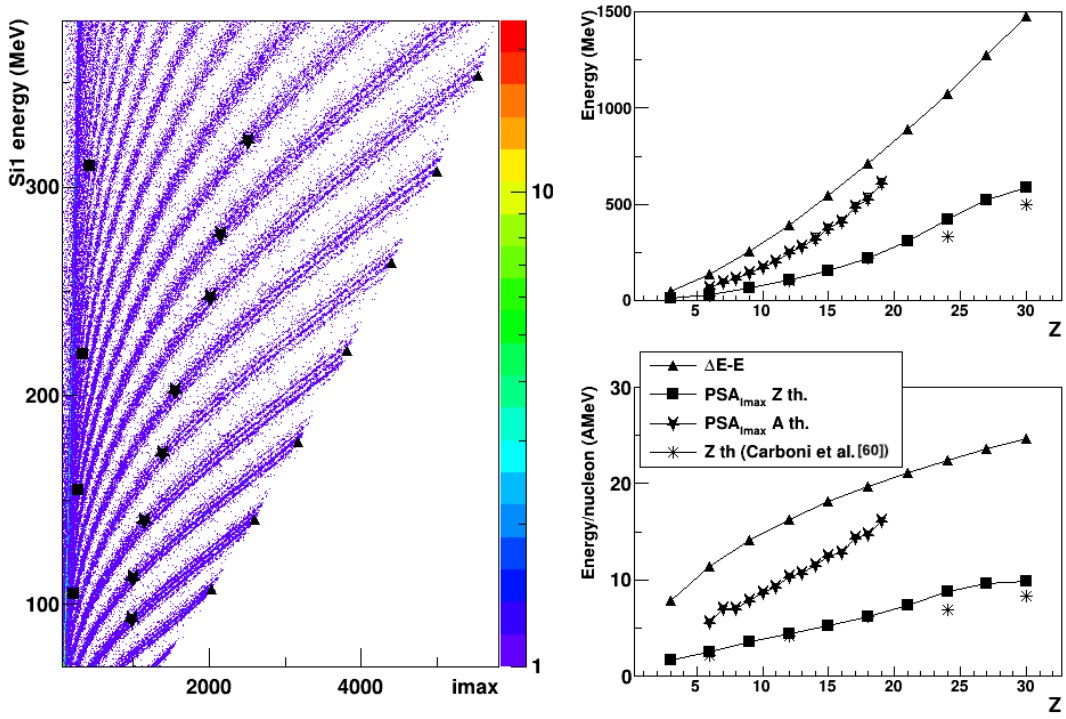


**Figure 2.12:** *Energy thresholds for atomic and mass number identification for ΔE-E and* PSA($I_{max}$)*, obtained by processing the current signal with a smoothing spline interpolation algorithm. We used the FoM for the adjacent element pairs (Z threshold) or for the adjacent most abundant isotopic pairs of a given Z (A threshold). The error bars are smaller than the marker size. In the left panel we show, using the same markers of the right panels, the obtained energy threshold values superimposed on the* PSA($I_{max}$) *correlation. The color code represents counts in each histogram cell, according to the legend shown on the right.*

of Fig. 2.12, the energy thresholds for the different techniques are reported on the Energy vs $I_{max}$ correlation, using the same markers as in the right panels, in order to evidence the different regions corresponding to element and isotopic identification. For every charged fragment we evaluate the FoM between the two peaks of the most abundant isotopic pair and define the energy threshold with the criterion already described.

Although, as we have previously shown, the quality of the isotopic resolution does depend on the processing algorithm, the energy values above which this resolution is available (i.e. the energy thresholds) are almost independent on the adopted procedures.

As a way to evidence the lowering of the energy threshold for isotopic separation obtained by using the PSA, in Fig. 2.13 the PID obtained with both *PSA($I_{max}$)* and ΔE-E (each method applied in its proper energy interval) is reported as a function of

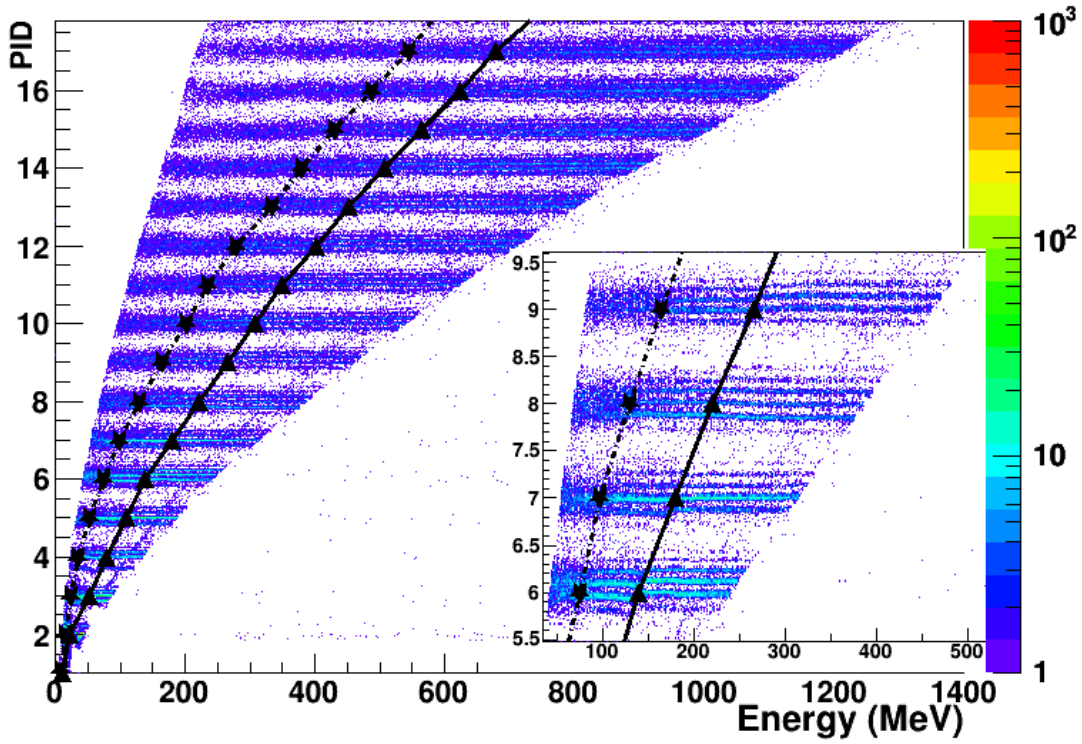


**Figure 2.13:** *(color online) Correlation between the PID (obtained both with the* PSA($I_{max}$) *and the ΔE-E methods) and the incident energy of the fragment. For a few selected isotopes, one for each element, the star marks the lower energy threshold for isotopic identification using PSA. The full (black) triangles show the punch-through energy in Si1, i.e. the lower energy threshold for isotopic identification using the ΔE-E technique. In between the two markers, for a given element, the identification is obtained via the* PSA($I_{max}$) *technique. To the right of the full triangle, identification is obtained through the ΔE-E technique. The inset shows an expanded view of a few elements from carbon to fluorine, to better appreciate the enlargement of the energy range where identification is possible, thanks to the PSA technique. The color code represents counts in each histogram cell, according to the legend shown on the right.*

the incident energy of the detected fragments. The energy intervals associated with the two identification methods are separated by markers, with the same meaning as in Fig. 2.12: stars are associated with the lower energy threshold for isotopic identification via PSA, triangles correspond to the punch-through energy in Si1 and therefore to the lower energy threshold for isotopic identification using the ΔE-E technique. In the inset, the good isotopic separation capability of the FAZIA detector is apparent, together with the effective widening of the energy range for mass identification obtained using the PSA on the first silicon detector, in addition to the standard ΔE-E technique applied to the first two Si stages.

To our knowledge, there are no other studies in the literature of the same kind and with similar details about isotopic identification with PSA. Therefore a comparison with previous results from the literature is not possible.

## 2.4 FAZIA detection energy thresholds

In the previous sections we have presented the identification techniques employed in data analysis and the improvements which have been obtained by the FAZIA Collaboration. Each technique is capable of identifying fragments only in a limited energy range. Moreover, charge and mass separation feature a different energy threshold for each technique. Fig. 2.14 summarizes the identification capabilities of the FAZIA detector in a single picture. In the left panel the ordinate axis reports the atomic number, Z, of the detected fragment and the abscissa represents its velocity. In the right panel the fragment energy is reported instead of its velocity.

The white region in both panels is the region where no identification can be obtained, so that its border gives the lower threshold of the FAZIA apparatus, either in velocity or energy, in terms of identification capability. The regions where the identification can be performed only in Z or both in Z and A are drawn respectively in light blue and orange. In those regions one exploits the PSA in Si1, so that the lower limits in velocity or in energy are the values reported in fig. 2.12, while the upper limit is the punch through velocity or energy for Si1. The areas in magenta (only charge identification) and green (both charge and mass identification) are the regions where identification can be performed via $\Delta$E-E using the Si1 vs Si2 correlation. The thresholds are determined by the punch through velocity or energy of the Si1-Si2 stack. The regions where identification is obtained via the $\Delta$E-E technique by exploiting the Si2 vs CsI correlation are coloured in red (only charge identification) and blue (both charge and mass identification). For these regions the range for identification goes from the punch through velocity or energy in the silicon stack to that of the silicon plus CsI combination. The identification performed with *Fast-Slow* correlation in CsI has not been reported in the plot because it covers a very small region and it only applies to light charged fragments.

The data reported in fig. 2.14 are obtained from data acquired by a standard FAZIA telescope during the ISO-FAZIA experiment, the first experiment of the Collaboration after the R&D phase. This is the reason why the Z axis is limited to $Z = 35$. Previous studies using heavier beams have shown the FAZIA capability to identify in Z all fragments up to Xenon ($Z = 54$) with comparable Z thresholds [60].

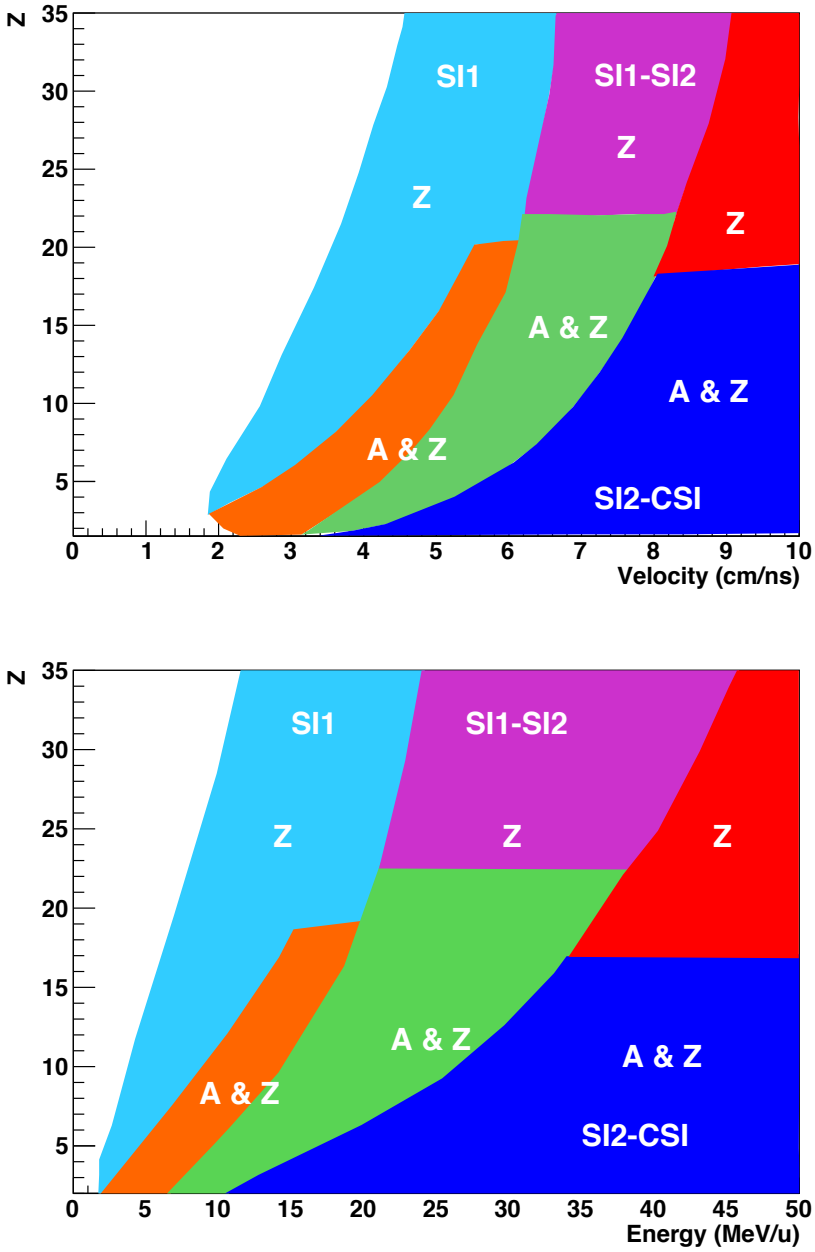


**Figure 2.14:** *In figure are shown two schemes where the energy thresholds in charge (Z) and mass (A) for the different identification techniques are resumed. In top (bottom) panel is shown the charge Z vs the velocity (energy) of detected fragments. The identification via Fast-Slow of CsI has not been included in this plot. The energy thresholds have been referred to the ISO-FAZIA data.*

# Chapter 3

# The ISO-FAZIA experiment

## 3.1 Goal and motivation

The FAZIA telescope array is very well suited for studies requiring the identification in charge and mass of the detected fragments. The good identification capability of FAZIA telescopes was first exploited in 2011, when the FAZIA Collaboration investigated the isospin transport process by means of just one prototype telescope. The study compared the reactions $^{84}$Kr+$^{112,124}$Sn at 35 AMeV [40]. The detector, which covered polar angles between 4° and 6°, was able to measure only the ejectiles associated to the QP phase space. As shown in Ref. [40], the $< N > /Z$ ratio of all the detected products was found to be systematically higher for the $^{124}$Sn target than for the $^{112}$Sn. Moreover, for light fragments, it was observed that the average isospin of those emitted close to the centre of mass velocity (i.e. those possibly coming from the neck) was higher than the isospin of those showing a velocity close to the QP (i.e. those possibly evaporated by the QP). The first observation was interpreted as an evidence of isospin diffusion, while the second one was explained as an evidence of isospin drift.

The ISO-FAZIA experiment was proposed in order to continue such a study using a more complete setup. In order to better exploit the small angular coverage of the apparatus, reverse kinematics (projectile more massive than target) has been used, thus exploiting the kinematic focusing of the ejectiles. The calcium target was chosen since two stable calcium isotopes with a large difference in isospin are available ($I = 1.0$ for $^{40}$Ca and $I = 1.4$ for $^{48}$Ca). In view of the isospin transport study, $^{84}$Kr was used for the projectile in order to have the projectile isospin lies almost exactly in between the values for $^{40}$Ca and $^{48}$Ca ($I = 1.22$ for $^{84}$Kr).

Nevertheless, the great improvement of ISO-FAZIA with respect to the previous experiment is the new multi-telescope setup which allows to detect fragments in coincidence. This is at variance with the previous experiment, performed with

just one telescope, where only inclusive data were collected. It is thus possible to obtain a better event selection, based on centrality and event type. For example, the QP and a great amount of its evaporation products can be clearly identified; neck fragments can be put into evidence too. A further possibility offered by this experimental setup is the coincident identification (in charge and mass) of fission fragments coming from the QP. To separate the dynamic fission of the QP (characterized by a short time scale, 200-300 fm/c) from its sequential fission (characterised by a longer time scale), the N/Z of both fission fragments could be compared for the two classes of events, thus gaining some information on the typical times of the isospin equilibration process. The comparison of the experimental data on the isospin transport to the predictions of theoretical models such as SMF (Stochastic Mean Field) [69, 70] or AMD (Antisymmetrized Molecular Dynamics) [4] could allow to extract some information on the symmetry energy term. The AMD code has been used in this work: it will be described in Chapter 4 and its results will be compared to our experimental data in Chapters 5 and 6.

## 3.2 Experimental Setup

The ISO-FAZIA experiment was performed in Catania at Laboratori Nazionali del Sud (LNS) of Istituto Nazionale di Fisica Nucleare (INFN) in June 2015. ISO-FAZIA was the first physics experiment after the R&D phase of the FAZIA Collaboration. A $^{80}$Kr beam at 35 MeV/u was used with two different calcium targets: $^{40}$Ca and $^{48}$Ca of 500 $\mu$g/cm$^2$, both protected by a thin carbon backing.[1] Data were acquired also for a $^{12}$C target of 308 $\mu$g/cm$^2$. The measurement with the carbon target is needed to estimate the carbon contamination introduced by the carbon backing. In order to acquired some data also for elastic scattering, to be employed in the calibration process, a gold target (196 $\mu$g/cm$^2$) was also employed for a short time.

Figure 3.1 shows a sketch of the geometric arrangement of the detectors during the ISO-FAZIA experiment and a picture of the experimental setup looking downstream along the beam direction. Four complete FAZIA blocks were used, arranged in a belt configuration covering polar angles from 2.4° to 17.4°, i.e. beyond the grazing angle of $\sim$1.9°.

The blocks were mounted inside the Ciclope scattering chamber at a distance of about 80 cm from target. Every block (area 8×8 cm$^2$) covers a solid angle of $\sim$0.01 sr. The vacuum inside the scattering chamber was $2\times10^{-5}$ mbar during the whole experiment. The beam was pulsed by means of a chopper. The time interval

[1] A Carbon backing is put on top of both side of the Calcium target by manufacturer in order to prevent the oxidation of the target surface in air during the mounting and dismounting phases. The manufacturer estimates 10 $\mu$g/cm$^2$ of Carbon for both side. See Sec. 5.3.6 for more details.

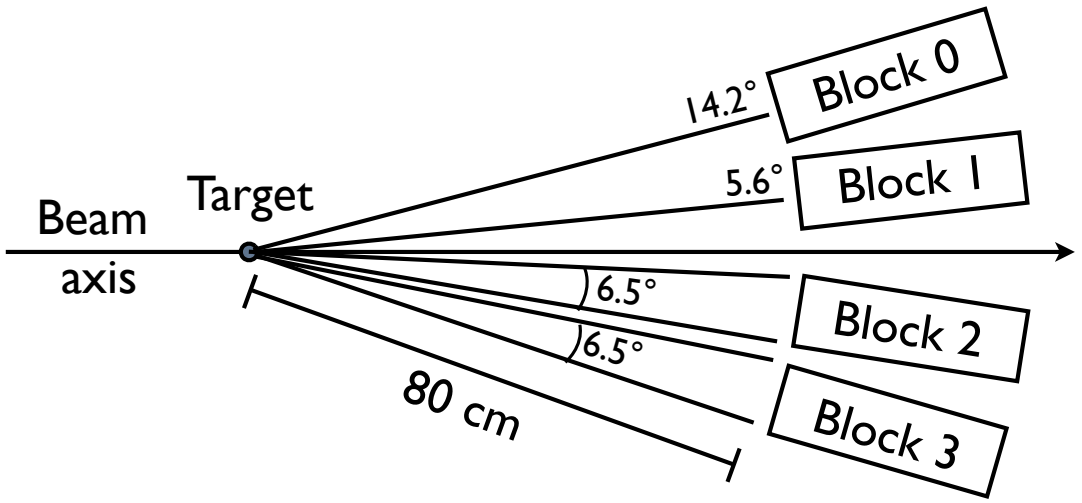


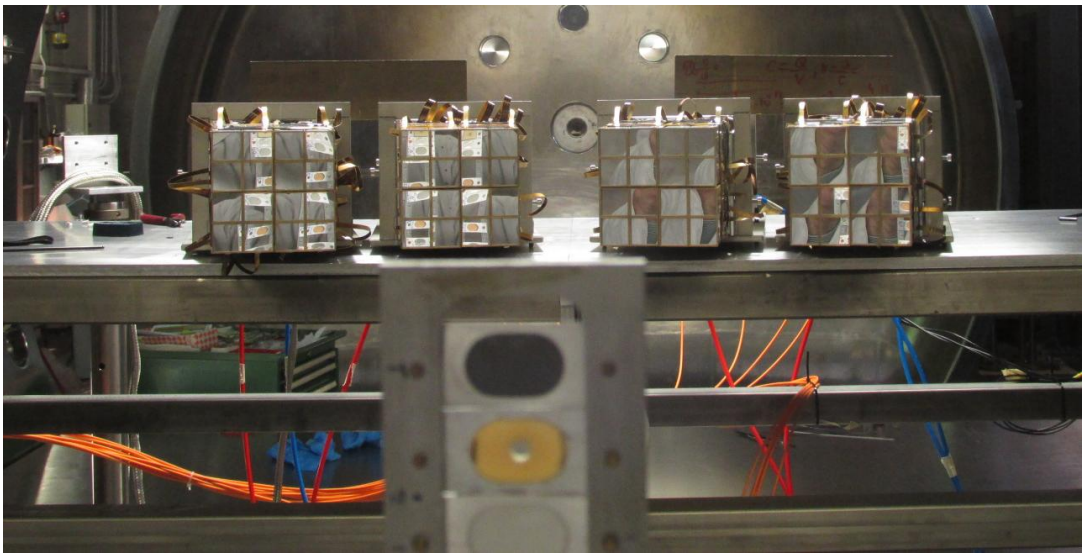

**Figure 3.1:** *The figure shows a picture of the experimental setup of the ISO-FAZIA experiment (bottom) and a sketch of its geometry (top). Four complete FAZIA Blocks were mounted inside the Ciclope Scattering Chamber of LNS in a belt configuration. The blocks are placed at a distance of 80 cm from the target. Each block covers an area of about* $8 \times 8 cm^2$ *and a solid angle of* $\sim 0.01$ *srad.*

between consecutive bunches being 120 ns. Events were acquired at a rate going from a minimum of 400 events/s to 700 events/s.

## 3.3 KaliVeda software

In handling and analysing the data acquired during the experiment, we have been supported by the $IN_2P_3$ Computing Centre of Lyon (FR) [71].

We have used an already available C++ library developed for the analysis of nuclear physics experiments, called KaliVeda [72] and based on the ROOT [73] analysis framework. KaliVeda was originally developed in GANIL (Caen, France) to provide simulation and analysis tools for the INDRA detector array [42]. It has then evolved, thanks to the addition of many other general tools of interest such as energy loss, stopping power and range calculations for ions with energy E/A = 1-100 MeV, particle identification algorithms exploiting PSA and ΔE-E matrices, physics analysis of multi-particle events and an interface to the Gemini++ statistical decay code [74].

The wide variety and general usefulness of its tools make KaliVeda a good choice for our purposes, also considering the already scheduled INDRA & FAZIA coupling in upcoming measurement campaigns at GANIL. Since the INDRA detector array uses analog electronics, it does not require the offline analysis of digitized signals. As a consequence, no such analysis was included in the Kaliveda library. FAZIA, on the other hand, features digitizer-based front-end electronics. In order to perform the usual FAZIA offline signal processing, a great effort was done to implement all the required processing algorithms, routines and procedures in the KaliVeda framework.[2]

## 3.4 Fragment identification and energy calibration

The mass number of the detected fragments is obviously a key observable in studies involving the nuclear isospin. It is worth mentioning that, since ISO-FAZIA has been the first experiment performed with the new FAZIA blocks, the whole identification and calibration procedure has been developed and applied for the first time in the present work. This section is dedicated to a detailed description of the identification and the energy calibration procedure.

### 3.4.1 Identification procedure

As already discussed in Sec. 2.2, a few different identification methods can be used to identify the fragments stopped in the different detector layers of FAZIA:

- *PSA($I_{max}$)* correlation based on Si1 signals to determine Z and A of the fragments stopped inside the first layer up to Z$\simeq$ 20;
- *PSA(Q)* correlation applied to Si1 to determine Z (of the fragments stopped inside the first layer) up to $Z$ = 36-37 (the atomic number of Kr is $Z$ = 36

[2]Part of this work has been performed during my stay in Caen (three months during 2016) as a visitor researcher.

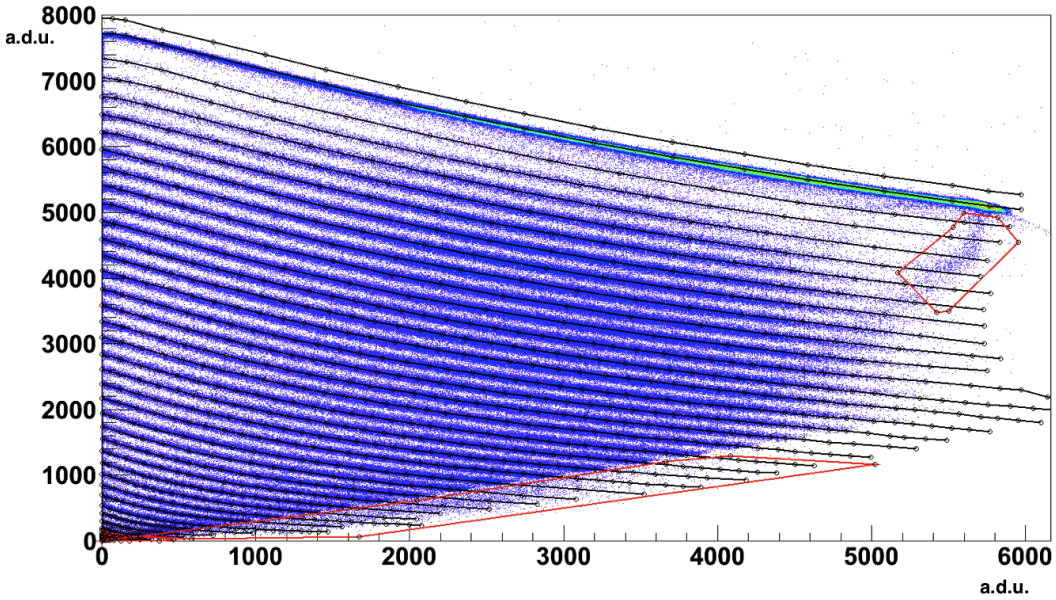


**Figure 3.2:** *ΔE-E correlation Si1-Si2. The identification grid is superimposed. Only one line for each Z was drawn and assigned a unique PID number. The graphical cut selection (in red) is needed to remove from the identification procedure the area inside the contour.*

and it determines the highest Z which can be produced in the reaction);

- ΔE-E correlation between Si1 and Si2 to identify in Z and A (up to $Z = 25$) the particles stopped inside the second silicon detector;
- ΔE-E correlation between Si2 and CsI to identify in Z and A fragments stopped inside the CsI detector;
- Fast-Slow correlation in CsI to identify in A light particles up to $Z$ = 4-5 stopped inside the CsI detector.

In the ISO-FAZIA experiment, due to the identification capability obtained with *PSA($I_{max}$)* after the optimization of the current signal processing (see Sec. 2.3), the *PSA(Q)* correlation has not been used. In fact, no gain in terms of energy thresholds and identification power was evidenced in combining both PSA techniques.

Though the correlation matrices obtained with the techniques listed above differ from one another, the various steps of the identification procedure are common to all the correlations. The first step is the production of an identification grid; starting from the correlation matrix we draw a piecewise linear curve superimposed on a visible experimental curve, corresponding in turn to given A and Z values. In our analysis, in order to obtain better identification using the KaliVeda software, we have generally used only one line for each Z, even when a few isotopic lines were clearly

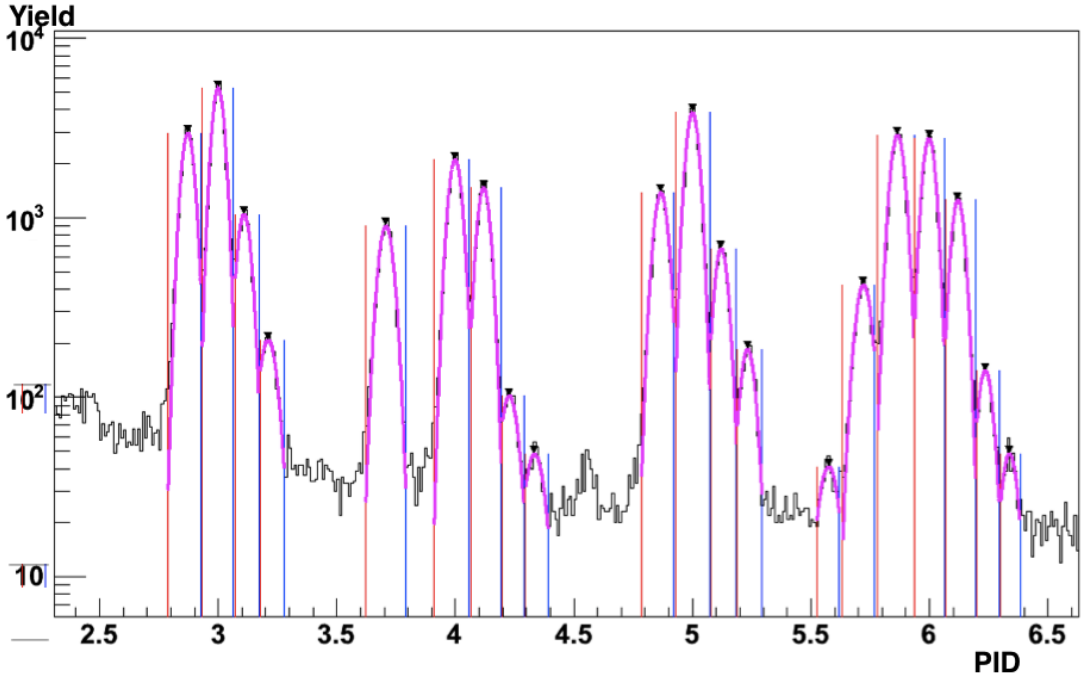


**Figure 3.3:** *PID distributions obtained by an interpolation based on the grid shown in fig 3.2. The orange and blue vertical lines correspond respectively to the lower and upper limit of the best confidence interval for identification. Elements from lithium to carbon are shown: each peak is associated to a different isotope.*

separated[3]. An example set of identification lines is shown in fig 3.2 superimposed on the Si1-Si2 ΔE-E correlation.

To each piecewise linear line we assign a number called PID or PI (Particle IDentification parameter) whose value is equal to the atomic number, Z, of the fragments associated to the underlying experimental curve. Graphical contour cuts, in red in fig 3.2, are used to exclude from the identification procedure some portion of the matrix, i.e. those inside the area determined by the contour. The excluded events would otherwise contribute to the background or degrade the identification resolution. Such events are associated to a residual number of punching through particles not eliminated by the veto condition (e.g. the veto condition for the Si1-Si2 correlation of fig 3.2 requires the CsI amplitude to be under a given threshold).

During the data analysis, a PID number is assigned to each detected fragment by interpolating between the drawn lines, basing on the event position in the correlation. The interpolation algorithm, implemented in KaliVeda, evaluates the relative distance between the point on the matrix and the 4 closer lines of the grid. After the interpolation procedure, we obtain a PID distribution as shown in fig.3.3 where every peak corresponds to a different isotope. The PID distribution shown in fig 3.3

[3]An exception, in that respect, is the Fast-Slow correlation, where a line has been drawn for each isotope. The identification via Fast-Slow will be described more in detail in sec 3.4.2.

was obtained using the grid shown in fig 3.2.

In isospin studies a correct evaluation of the neutron content of the detected fragments is quite important. In order to improve the reliability of the identification, we assign a quality code to each identified fragment as follows. In the calibration phase, a confidence interval is determined for each isotopic peak in the PID spectrum, basing on a gaussian fit of each peak. For each peak a lower and an upper limit of the "best" confidence interval is determined. In fig 3.3 we show in orange and in blue the lower and upper limit respectively for each isotope. In the data analysis, KaliVeda finds which of the PID intervals defined during the calibration phase contains the PID assigned to the analysed event and assigns to the fragment the corresponding Z and A values together with a specific quality code. Code=0 is used when the assigned A is considered totally reliable; code=1 is used when the assigned Z is considered reliable but the mass number assignment is not completely reliable (uncertainty of $\pm 1$ on A); code=2 is used when the PID value of the detected fragment falls outside any isotopic interval, so that neither Z nor A can be reliably assigned. Fragments with code=2 are not ignored in the analysis, though having them classified with a particular code allows for a better evaluation of their effect on the final results of the analysis.

### 3.4.2 Fast-Slow identification with CsI

The identification procedure applied to the Fast-Slow correlations obtained from the CsI scintillators differs slightly with respect to the standard procedure described in previous section. In fact, the Fast-Slow identification was already implemented in KaliVeda and successfully applied in measurements performed with the INDRA detector. The other identification procedures were either newly written or modified to better match with the characteristics of the FAZIA detector.

In the Fast-Slow identification grid, a piecewise linear curve is drawn for each isotope (instead of only one line for each element). In fact, the interpolation algorithm used for the Fast-Slow identification gives better results when all the isotopic lines are drawn. In fig. 3.4 we show, as an example, a Fast-Slow identification grid (black curves) superimposed over the associated matrix (left panel). The fragments falling in between isotopic lines with different Z's are ignored, as apparent in fig. 3.4 (top right), where no counts are present in the intermediate regions between isotopes with different atomic number. Using suitable hand-drawn constraints (in red in fig. 3.4) it is possible to select the region of the correlation were the identification can be accomplished.

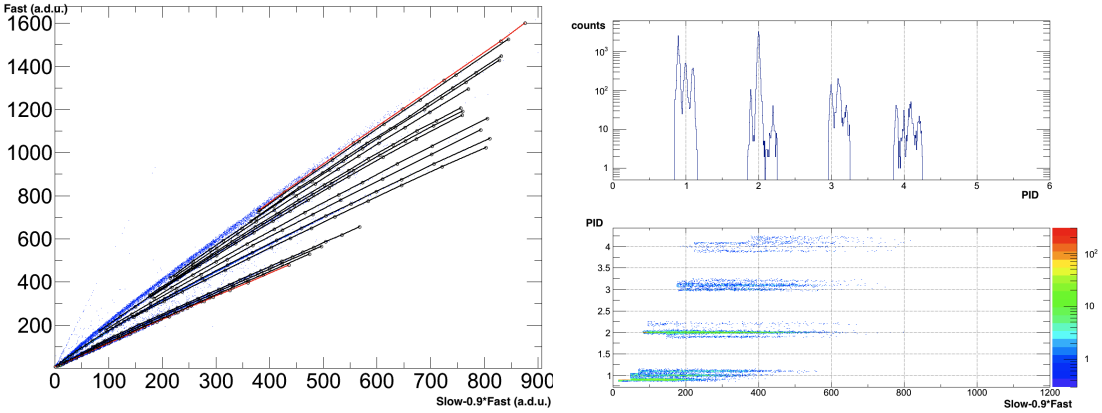


**Figure 3.4:** *Left panel: Fast-Slow correlation for a CsI scintillator with the identification grid superimposed; a graphical constraint (in red) used to remove part of the events from the identification procedure is also shown. Right panels: linearized PID-Slow correlation (bottom) and associated PID spectrum (top).*

### 3.4.3 Energy Calibration: AMI software

In the ISO-FAZIA experiment, four FAZIA blocks were used, for a total of 64 telescopes (though not all the telescopes were working correctly). This means slightly less than 320 identification grids must be produced. Hand-drawing of the piecewise linear isotopic curves is a cumbersome and time consuming task, which has required many months of work (also considering the testing and optimising phase). Meanwhile, a semi-automatic procedure for producing the identification grids is being developed by the FAZIA collaboration. In fact, at least 12 complete FAZIA blocks will be used in the next FAZIA-INDRA experimental campaign at GANIL, for which 960 identification grids must be produced, considering both PSA and ΔE-E correlations for all the 192 telescopes employed. The new semi-automatic fit procedure will produce both the energy calibration factors and the grids for the ΔE-E methods (both Si1-Si2 and Si2-CsI correlations). It is called Advanced Mass Identification (AMI) [75]. Its basic ingredient are the energy loss and range tables by Hubert et al. [76].

The fit procedure starts from a preliminary grid made of about ten lines hand-drawn on the experimental uncalibrated correlation. Then, using the energy loss calculation, it calculates new curves, one for each chosen isotope. The AMI procedure applies an energy calibration formula to the two axis variables, looking for the best matching between the estimated curves and the underlying experimental correlation. It has been devised to work both with silicon and CsI detectors, so that the calibration formula [77, 78] depends on 5 parameters: the gain factor, the recombination parameter, the nuclear interaction parameter, the delta ray energy threshold and the detector thickness. Some of these parameters are fixed and they

depend on the detector type (Si or CsI): for example, the thickness of the CsI is fixed at 10 cm and the nuclear interaction parameter is fixed at 0 for the silicon detectors.

The fit procedure produces:

- the calibration factors for all the detectors of the telescope;
- the identification grid for both for Si-Si and Si-CsI ΔE-E matrices;
- the Z and A assignment for each line of the grid;
- the "best fit" thickness for each silicon detector with an uncertainty of ± 5 $\mu$m.

When the identification and calibration procedures of the ISO-FAZIA experiment started, the AMI software was still at a preliminary stage of development and its results were not fully reliable. For this reason the grids produced by the software and the relative (Z, A) assignment have not been used in this work. We have adopted, however, the calibration factors produced by AMI for all the Si and the CsI detectors. The obtained calibration factors have been checked by exploiting the elastic peaks obtained in the energy spectra when using a gold target (the energy of the elastically scattered beam particles is uniquely defined by the beam energy and the scattering angle). The punch through energies of isotopes from Helium to Argon have also been used for checking the calibration. As usual, the energy lost the detected fragments inside the target has also been taken into account during the calibration procedure, by assuming that the nuclear interaction has happened at half the target thickness.

## 3.5 Z and A assignment

Since it was not possible to use the AMI software for identification and (Z, A) assignment, we were faced with the problem of assigning to each experimental curve in the PSA and ΔE-E correlation the correct (Z, A) values. This is not a trivial task, since many different isotopes are produced for each element and since there is no a-priori criterium to tell which ones will be produced.

However, in a ΔE-E correlation, when an experimental line extends up to the punch through (i.e. the maximum energy for the associated isotopes is greater than the punch through energy $E_{pt}$ in the second telescope layer) the Z, A values and the $E_{pt}$ are strictly related. Therefore we selected a "reference" telescope and we took note of the position of the punch through points for all the punching through isotopes (in uncalibrated units) up to Argon. We correlated the coordinates of those points with the theoretical punch through points evaluated with the Hubert energy

loss tables. We based our calculation on the nominal detector thickness[4]. Thanks to the very good linearity in energy of the Si detector response, using a linear fit we obtained the calibration factors relating the uncalibrated units to MeV for Si1 and Si2. The $E_{pt}$ values (and therefore the fit residuals) are very sensitive to the choice of the (Z, A) pair, so that an abnormally large fit residual clearly points out when a wrong assignment has been made.

The relative isotopic abundances obtained after (Z, A) assignment have been compared with previously published papers in order to verify their compatibility with the isotopic population obtained with similar systems at the same energy [79–81].

Once satisfied with the Z and A assignments obtained from Si1-Si2 correlations, we extended our work to the Si-CsI correlation and PSA correlation in Si1 using the Si1-Si2 as a guide (isotopic abundances are not expected to change abruptly for particles stopped in Si2 with respect to those stopped into the Si1 or CsI). Having performed the assignment on the "reference" telescope, it was a trivial task to extend it to the other telescopes, even more since the nominal gain and characteristics are the same for all the FAZIA telescopes.

For the future experiments, this work could be avoided because the AMI fit procedure provides us also the correct Z and A assignment based on the energy loss calculation.

## 3.6 Telescopes not fully working

Only part of the 192 detectors worked properly during the whole duration of the ISO-FAZIA experiment. There were several different causes of malfunctioning:

- electronic problems affecting a whole FEE card (e.g. trigger problems, over-current, over-temperature) or just a single channel (e.g. a broken capacitor on a preamplifier, problems with the high voltage, a noisy electronic channel);
- detector problems (e.g. broken connection between a detector and the FEE card, broken micro-bonding);
- instability of the detector performance due to acquisition problems or instability of its bias voltage.

If just one layer of the telescope is missing, the telescope is not rejected in the analysis. However, a dedicated identification and calibration procedure is needed to

[4]Before mounting the silicon pads in the FAZIA block, the thickness of one "reference" silicon detector for each wafers as been measured with a precision of $\pm 1\mu$m. This is considered the nominal thickness of all the pads obtained from that silicon wafers.

recover its information. The PSA exploits the information from a single layer, so it does not suffer from a missing layer in the telescopes; on the other hand, the ΔE-E identification is not always feasible. When one of the identification techniques can be performed, the standard procedure already described in Sec. 3.4.1 is used.

The AMI software needs a complete ΔE-E telescope in order to give correct results. When a telescope is not complete, so that AMI cannot be used, the energy calibration exploits the punch through points (i.e. the positions of the cusps in a ΔE-E correlation). The punch through energies depend on the Z and A values and on the energy of the fragment and also from the detector thickness. The Z and A assignment for a not-complete telescope is obtained by comparing the abundances of the different detected isotopes with those of a "reference" fully operational telescope placed at the same polar angle. Using the assigned Z and A values and the nominal detector thickness, the energy of the punch through points are estimated using the energy loss table by Hubert. Then, using a linear fit, the calibration factors for the detectors of the incomplete telescope are evaluated.

The full energy of the charged fragments detected by not complete telescopes has been obtained by taking into account the energy lost by the particle in the missing layer, treated as a dead layer of known thickness.

## 3.7 Detectors status in ISO-FAZIA

At the end of the identification and calibration phase, one gets the complete picture of the status of the detectors during the experiment. Figure 3.5 reports a sketch of the FAZIA blocks used in the ISO-FAZIA experiment. The working condition of each telescope is expressed by a colour code:

1. green: fully operational telescopes (total number: 24);
2. red: telescopes which were in full operation only for one of the two studied system (total number: 5);
3. purple: telescopes with a missing layer (total number: 14);
4. white: telescopes which were not used in the analysis, due to malfunctioning (total number: 21).

In view of the analysis described in Chapters 5 and 6, from the status of the detectors shown in fig. 3.5 we have derived a software filter to describe the geometric efficiency of the apparatus. The filter is needed for a better comparison of the simulation results with the experimental data and it is described in Sec. 4.4. Given the geometry of the apparatus, as shown in fig. 3.5, it is clear that its efficiency for

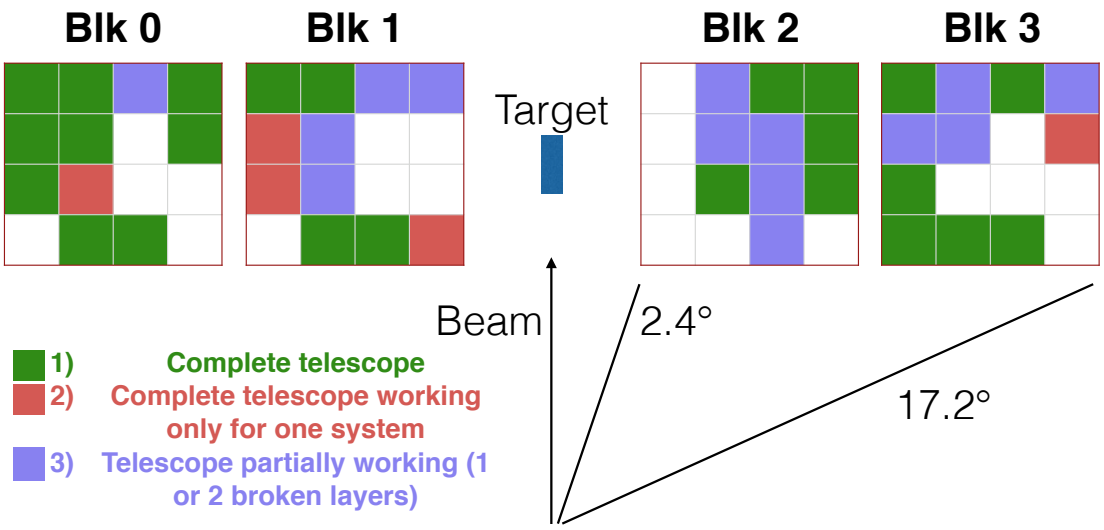


**Figure 3.5:** *Status of the telescopes employed for the ISO-FAZIA analysis, after the identification and calibration procedure has been performed. Different colours correspond to different working conditions. Green: fully operational telescopes; red: telescopes which were fully operational though only for one of the two studied systems; purple: telescopes with a missing layer.*

peripheral collisions (whose products are focused at small angles) is quite low. The efficiency improves for dissipative collisions, as it will be shown in the following.

# Chapter 4

# Simulation codes

In order to figure out the reaction mechanisms related to the charged fragment distribution experimentally observed during a nuclear collision, the comparison between the experimental results and the predictions of some theoretical models is mandatory. Very specific effects are expected at Fermi energies. In fact, this energy regime is a transition region from the mean-field dominated dynamics to a high energy region where individual nucleonic degrees of freedom and associated two-body effects dominate.

Many different models have been developed to study the possible reaction mechanisms. It is possible to classify them into two main classes:

- dynamical transport models, which describe the time evolution of the system by means of transport equations;
- statistical decay models, which consider the nucleus as an equilibrated and excited thermodynamic systems which tends towards its ground state dissipating energy by means of particle emission or other competitive mechanisms (e.g. fission or resonances) whose relative importance depends on the branching ratios of the different available channels.

The use of a pure statistical model is not appropriate except for situations in which the equilibrated system is known, e.g. complete fusion. On the other hand, microscopic transport models provide a suitable description of the dynamic phase of a nuclear collision. The coupling of a dynamic model, to study the initial dynamic evolution of the reaction, and of a statistical decay code as afterburner, i.e. to describe the de-excitation of the hot primary fragments, is usually the best compromise allowing for a reasonable reproduction of the experimental data.

Transport models can be divided into two main classes: those based on the BUU approach (for example, SMF [69] or BLOB [82]) and those based on the molecular dynamics (such as, for example AMD [4]). The first class describes directly the

evolution of the phase space density, while the second class describes the evolution of the nucleon coordinates and momenta. In this work we use the AMD model due to its capability to reproduce in a reliable way the main features of the collisions in the Fermi energy domain in all the range of possible impact parameters. We stopped the calculation at 500 fm/c, which is a sufficiently long time to assure that the dynamic phase is concluded. As a consequence, the following evolution can be safely described by means of a statistical model.

We simulate about 25000 primary events for each studied system both with asy-stiff and asy-soft parametrization. The results of the AMD simulation have been used as input tothe GEMINI++ [5] code, employed as afterburner. Around 1000 secondary events are produced for each primary event.

The coupling between AMD and GEMINI++ has shown a better agreement with the experimental data with respect to other combinations such as BLOB followed by GEMINI++. Another code used in this thesis is HIPSE, which is a phenomenological model (not belonging to any of the previously described groups) able to reproduce the absolute cross sections and the general behaviour of the macroscopic dynamic properties of the fragments produced in reactions at Fermi energies. The HIPSE code has been used to quantify the Carbon background observed in the experimental data.

## 4.1 Antisymmetrized Molecular Dynamics (AMD)

For heavy ion collisions at intermediate energy a microscopic description of the early dynamical phase of the reaction is challenging due to the competition between many different possible reaction mechanisms. The description of the time evolution of the whole system, broke down into many heavy or intermediate mass fragments together with light charged particles, requires a fully quantum many-body approach. The reaction dynamics depends on the nuclear matter properties expressed by the equation of state which depends on the mean-field of the nuclear bulk, and on the many-body correlations between nucleons in the nuclear medium.

AMD (Antisymmetrized Molecular Dynamics) is a transport model for nuclear reactions and it has been developed in 1992 by A. Ono and collaborators [4]. This model was born as the antysimmetrized version of the Quantum Molecular Dynamics (QMD) code [83, 84] including also two-nucleon collisions. In order to get an increasingly realistic description of the reaction mechanisms, during the last thirty years many improvements have been done to the model [85–87] also taking into account phenomena like clustering effects or pion production, not included in the first version of the code.

### 4.1.1 Main structure of AMD

AMD describes the dynamics of a many-nucleon system by studying the time evolution of a Slater determinant of Gaussian wave packets for A nucleons:

$$\langle \mathbf{r}_1 ... \mathbf{r}_A | \Phi(Z) \rangle \propto \det_{i,j} \left[ exp\Big\{ -\nu(\mathbf{r}_i - \mathbf{Z}_j/\sqrt{\nu})^2 \Big\} \chi_{\alpha_j}(i) \right] \tag{4.1}$$

where $\mathbf{r}_i$ are the coordinates of the single particles, $Z = \{\mathbf{Z}_i\}_{i=1,...A}$ are complex variables corresponding to the position (real part) and the momentum (imaginary part) of the centroids of the gaussian packets, $\nu$ is the width of a packet and $\chi_{\alpha_j}(i)$ are the isospin-spin states with $\alpha_i = p\uparrow$, $p\downarrow$, $n\uparrow$ or $n\downarrow$. The width parameter can be modified and in this work it has been treated as a constant value set to $\nu = (0.16 fm)^{-2}$ as suggested by A. Ono. In contrast to QMD, the AMD correctly take into account the fermionic nature of the nucleons because the Slater determinant intrinsically implements the Pauli exclusion principle.

By applying the time-dependent variational principle, eq.(4.2), the time evolution of each wave packet is determined, thus deducing the equation of motion for Z, as in eq.(4.3):

$$\delta \int_{t_1}^{t_2} \frac{\langle \Phi(Z)| \left( i\hbar \frac{d}{dt} - H \right) |\Phi(Z)\rangle}{\langle \Phi(Z)|\Phi(Z\rangle} dt = 0 \quad \text{with} \quad \delta Z(t_1) = \delta Z(t_2) = 0 \tag{4.2}$$

$$i\hbar \sum_{j\tau} C_{i\sigma,j\tau} \frac{dZ_{j\tau}}{dt} = \frac{\partial \mathscr{H}}{\partial Z^*_{i\sigma}} \tag{4.3}$$

where $\sigma, \tau = x, y, z$ and $\mathscr{H}$ is the hamiltonian operator. The equation of motion eq.(4.3) is solved using the Euler method with a time step $\Delta t = 0.75\,\mathrm{fm/c}$. The Hamiltonian requires an effective interaction in order to estimate the mean-field. In the present calculation, we employ the Skyrme SLy4 force [88] using $K = 230\,\mathrm{MeV}$ for the incompressibility of nuclear-matter and $\rho_0 = 0.16\, fm^{-3}$ for the saturation density. Two different parametrizations of the symmetry energy term of nuclear matter at normal density have been tested: the **asy-stiff**, with $S_0 = 32.0\,\mathrm{MeV}$ and $L = 108\,\mathrm{MeV}$ as slope parameter, and the **asy-soft**, with $S_0 = 32.0\,\mathrm{MeV}$ and $L = 46\,\mathrm{MeV}$.

Besides the mean field term, in the calculation of the dynamic phase of a nuclear reaction, the nucleon-nucleon collisions are extremely important, especially around the Fermi energy. In AMD, a two-nucleon collision is treated as a stochastic transition from an AMD state $|\Phi_i\rangle$ to another AMD state $|\Phi_f\rangle$. The transition is governed by a scattering probability depending on the impact parameter between the two nucleons which is proportional to the density overlap of their gaussian packets. In

calculations presented in this work, the in-medium total cross section by Li and Machleidt [89] has been used. The Pauli blocking for the scattered nucleons is taken into account in the calculations. Angular distributions are assumed to be similar to the experimental data in free space.

### 4.1.2 Transition with clustering effect

An extension of the original AMD code has been introduced by Ono [86] to take into account the formation of light clusters ($A = 2, 3$ or 4) in the final state $|\Phi_f\rangle$. In AMD, if several wave packets at the same time have the same centroid position and momentum, they are propagated in the same way by the equation of motion and tend to move together such as a cluster of particles. The formation of cluster states has been implemented in a reasonable way. In fact, if the wave packets of the nucleons in the cluster are placed randomly in the phase space, the probability to form a cluster is reduced. Particle clusterization process is treated as a particular case of nucleon-nucleon collision.

First of all, for a scattered nucleon $N$ the possibility to form a cluster with one of the nucleon $B_j$ with same spin and isospin is considered. Considering two interacting nucleons $N_1, N_2$ with a relative velocity $v_{NN}$ which form a cluster $C_1, C_2$ with two spectator particles $B_1, B_2$, the partial differential cross section to the final channel is given by:

$$v_{NN} d\sigma(N_1 B_1 N_2 B_2 \rightarrow C_1 C_2) = \frac{2\pi}{\hbar} |M|^2 \delta(E_f - E_i) \frac{p_{rel}^2 dp_{rel} d\Omega}{(2\pi\hbar)^3} \tag{4.4}$$

where M is the two nucleon scattering matrix not including cluster formation and $\delta(E_f - E_i)$ enforces the conservation of energy. This process also includes the collisions without cluster formation where $C_j = N_j$. After introducing the clusterization process the final state is still represented by a Slater determinant of nucleon wave packets. The time evolution of the many-body system does not depend on cluster formation in some states due to previous collisions. In this approach, a cluster can be easily broken when one or more nucleons inside the cluster collide with another nucleon in the system.

In nuclear matter, especially during an explosive reaction, the interaction between clusters can play a fundamental role in determining the probabilities of the different output channels of the reaction. Few clusters can form a bound state which can correspond to the ground state of light isotopes or to the Hoyle state of heavier isotopes ($C^{12}$, $O^{16}$). Even if the binding energy of these states is weak, the AMD can produce them by introducing an inter-cluster correlation as a stochastic process of cluster bonding. During the time evolution of the reaction, the bonding process

selects possible bound states of two or more clusters close in phase space. This inter-cluster correlation reduces the presence of cluster gas in the nuclear medium.

### 4.1.3 Statistical decay

The fragments generated in microscopic calculations during the first hundreds of fm/c are usually produced in highly excited states rather then in their ground states. These fragments decay by evaporating particles for a long time ($\sim 3 \cdot 10^4$ fm/c). In order to take into account this effect, the AMD tool includes also a statistical decay code which is a modified version of the CASCADE code [90] (we did not use it in this work because we preferred the widely used GEMINI++ code).

In the included statistical decay code, the partial widths of the competing decay channels for a nucleus with given excitation energy and spin $(E_1, J_1)$ into two nuclei $(E_2, J_2$ and $E_3, J_3)$ are evaluated. Each of the two nuclei can in turn be produced in an excited state.

If we run AMD for long times, some statistical decay happens anyway as a result of the dynamic code, thus modifying the produced fragment distribution. As a consequence, we decided to extend our calculations up to 500 fm/c in order to take into account the initial effect of statistical de-excitation directly produced by AMD. In this way, less excited sources are used as input to the afterburner (GEMINI++) and a better matching with the afterburner characteristics is obtained. In fact GEMINI++ is well suited for nuclei with excitation energy up to $2.5 - 3$ MeV/u.

### 4.1.4 AMD predictions for $^{80}$Kr + $^{48,40}$Ca

In this section we present some results concerning the studied systems, $^{80}$Kr+$^{48,40}$Ca at 35 MeV/u, obtained with the AMD code before applying the afterburner (GEMINI++, Sec. 4.2) or the geometrical filter (see Sec. 4.4). This section is aimed at showing the observables depending on the symmetry energy parametrization at the level of primary fragments.

The AMD calculation has been run until both 300 fm/c and 500 fm/c and we have veryfied that the obtained results are quite similar. As a consequence, in the following we present only results for a calculation time of 500 fm/c.

In fig. 4.1 the correlation between Z and the impact parameter $b$ has been drawn for the $^{48}$Ca target for all the ejectiles. We can clearly observe at large $b$ values the presence of the QP and QT as perfectly identifiable fragments together with some LCPs and IMFs, produced in binary DIC events for peripheral collisions. For a decreasing impact parameter, i.e. increasing the energy dissipated in the reaction, the QT and QP become lighter, losing more particles and fragments due to the

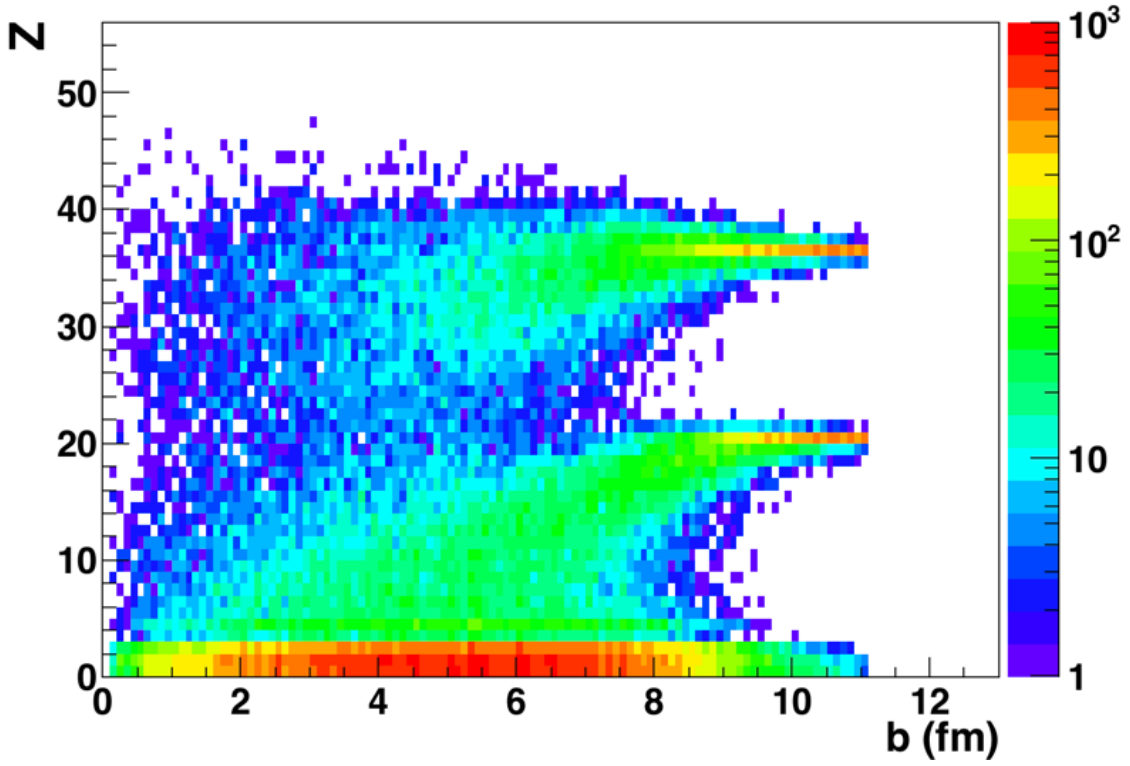


**Figure 4.1:** *Z vs b correlation for the simulated primary fragments for the* $^{80}Kr+^{48}Ca$ *reaction.*

opening of new channels, such as fast fission or fragmentation. For very central collisions the identity of the QP is lost and it is possible to observe the presence of heavy fragments with $Z > 36$, probably due to very few incomplete-fusion reactions, and IMFs, produced in multi-fragmentation processes.

In the left panel of fig. 4.2 the same Z value as in fig. 4.1 is reported as a function of the velocity $V_Z$ in the CM reference. $V_Z$ is the velocity component along the beam axis. We can observe the QP (forward emitted heavy fragment) and the QT (backward emitted heavy fragment) together with many LCPs and IMFs. In the right panel of fig. 4.2 the same correlation is reported after applying a cut on the impact parameter ($b > 5$ fm) in order to select only peripheral and semi-peripheral events, in which the binary character of the reaction is more evident.

In order to study the neutron content of the QP in binary events ($b > 5$ fm), one of the observables experimentally accessible in this work, we put some conditions on the fragment velocity and size in order to separate the QP from the other fragments, i.e. $V_Z > 0$ and $Z_{frag} > 20$. In the left panel of fig. 4.3 the charge distribution of the selected QP has been drawn for the $^{48}$Ca target only. The QP is peaked around $Z = 36$, as expected, but there is also a tail extending up to $Z = 40$.

One of the observables generally used to put into evidence the isospin transport

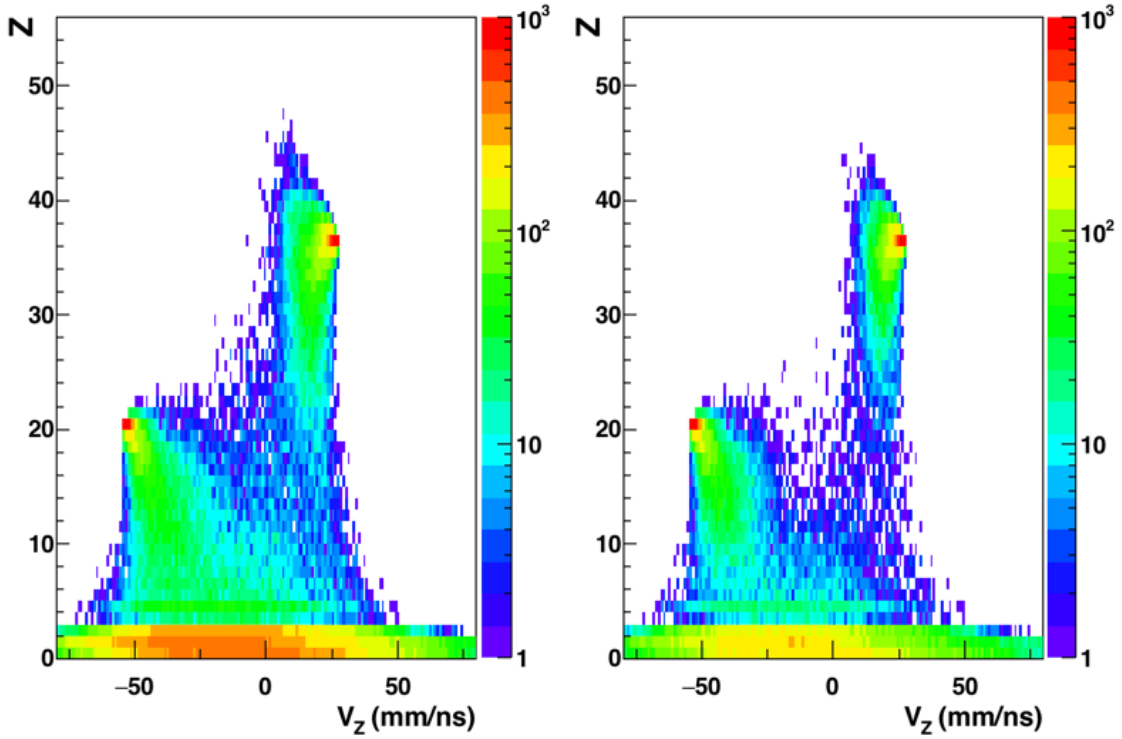


**Figure 4.2:** *Correlation Z vs fragment velocity along the beam axis in the CM reference frame for the $^{48}Ca$ target. In the right panel the same correlation is drawn with the further condition $b > 5\,fm$.*

phenomena is the average neutron number divided by Z for each element <N>/Z, calculated according to the formula:

$$\frac{< N >}{Z} = \frac{1}{Z}\frac{\sum_{i=0}^{n}(A-Z)_i Y_i}{\sum_{i=0}^{n} Y_i}$$

where $Y_i$ is the yield of each isotope and the sum is extended over all the isotopes detected for the given Z. Concerning the selected QP, the <N>/Z value has been extracted for both systems and the results as a function of the QP charge are reported in the right panel of fig. 4.3 for both the adopted parametrization for the symmetry energy term. The expected isospin diffusion effect (see Sec. 1.2.2) is clearly present and it manifests itself as a higher neutron content for the QP in the reaction with $^{48}$Ca with respect to the $^{40}$Ca case for a QP charge smaller than the projectile value. In fact, starting from an initial projectile isospin $I = 1.22$, before the collision, the AMD predicts an increase (decrease) of the QP isospin for the $^{48}$Ca ($^{40}$Ca) case as the QP charge decreases, until it reaches the value $I \sim 1.25$ ($I \sim 1.18$). The

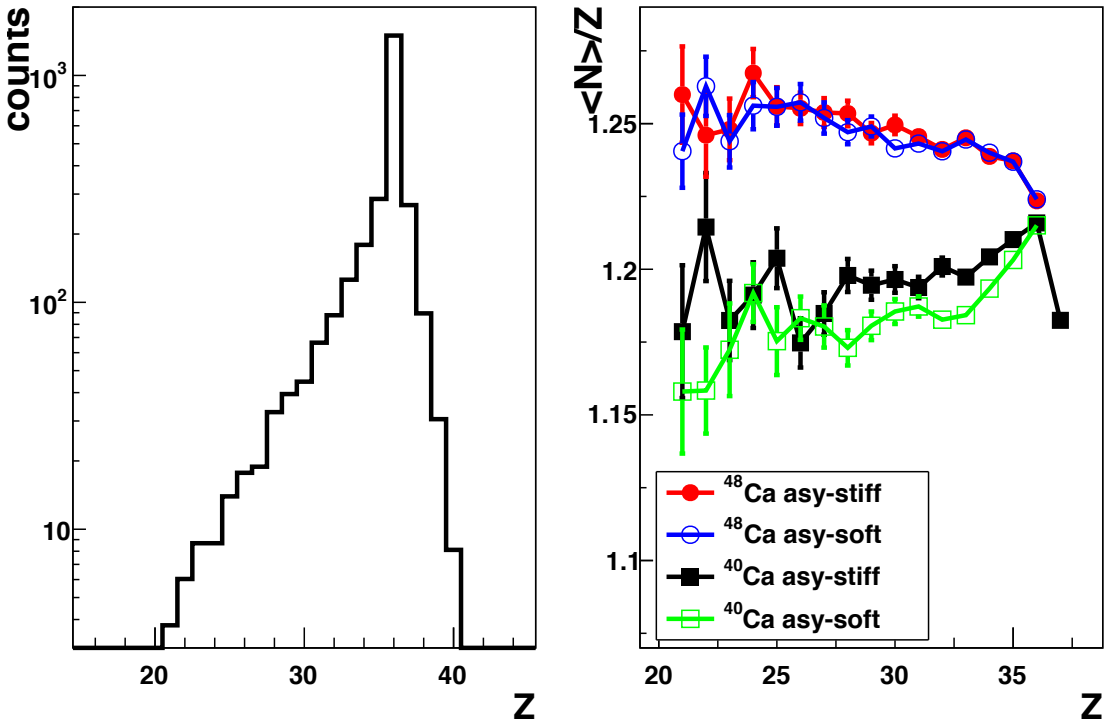


**Figure 4.3:** *Left panel: charge distribution of the QP in peripheral collisions (only the events with $b > 5$ fm have been taken into account). Right panel: <N>/Z of the selected QP as a function of the QP charge for different symmetry energy term parametrizations and for the two targets employed in this work.*

dependence on the symmetry energy parametrization is negligible for the $^{48}$Ca case and weak for the $^{40}$Ca one.

The <N>/Z of the QP can be presented also as a function of the impact parameter of the reaction. This correlation is shown in the left panel of fig. 4.4 and it again demonstrates (in a even clearer way) the isospin diffusion phenomenon and its dependence on the amount of nucleon exchange. In very peripheral collisions, where few nucleons are exchanged, the isospin diffusion is absent and $I_{QP} = 1.22$, as for the projectile. When the centrality increases, the gap between the $^{40}$Ca and $^{48}$Ca cases gets wider and wider, and the QP associated to the $^{48}$Ca target is more neutron-rich than the QP of the $^{40}$Ca one. As already observed in fig. 4.3, the effect of the different stiffness is negligible for $^{48}$Ca and very weak for the $^{40}$Ca case.

The width of the isotopic distribution of the QP ($\sigma_A$) has also been studied and plotted in the right panel of fig. 4.4 as a function of the charge. It can be evaluated

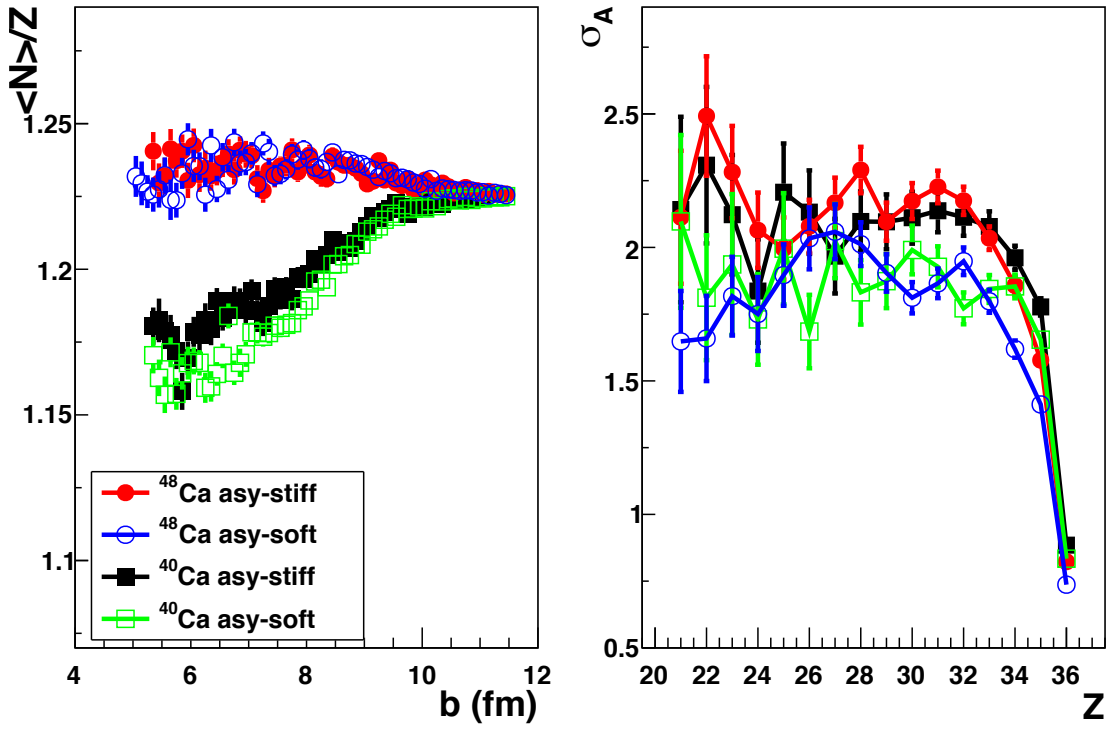


**Figure 4.4:** *Left panel: <N>/Z of the QP vs the impact parameter of the reaction. The different symmetry energy parametrization tested in the AMD code and the different systems are reported with different colors and markers. Right panel: the $\sigma_A$ of the QP isotopic distribution as a function of the charge Z for the same model parametrizations.*

as:

$$\sigma_A = \sqrt{\frac{\sum_{i=0}^{n}((A-Z)_i - \overline{(A-Z)})^2 Y_i}{\sum_{i=0}^{n} Y_i}}$$

This variable is more sensitive to the symmetry energy parametrization than the <N>/Z: especially for QP coming from the most dissipative collisions, the asy-stiff parametrization produces a wider isotopic distribution than the asy-soft one. The effect is larger in the case of $^{48}$Ca system than for the $^{40}$Ca system.

We have investigated the <N>/Z vs Z and the $\sigma_A$ vs Z also for LCP and IMFs emitted in coincidence with the QP and the QT in peripheral and semi-peripheral collisions. Many of these ejectiles corresponds to LCPs and IMFs emitted from the neck. In fig. 4.5 the <N>/Z (left panel) and the $\sigma_A$ (right panel) of these ejectiles have been plotted as a function of their charge (Z). The <N>/Z is higher for the $^{48}$Ca target than for the neutron-poor target, since more neutrons are available to

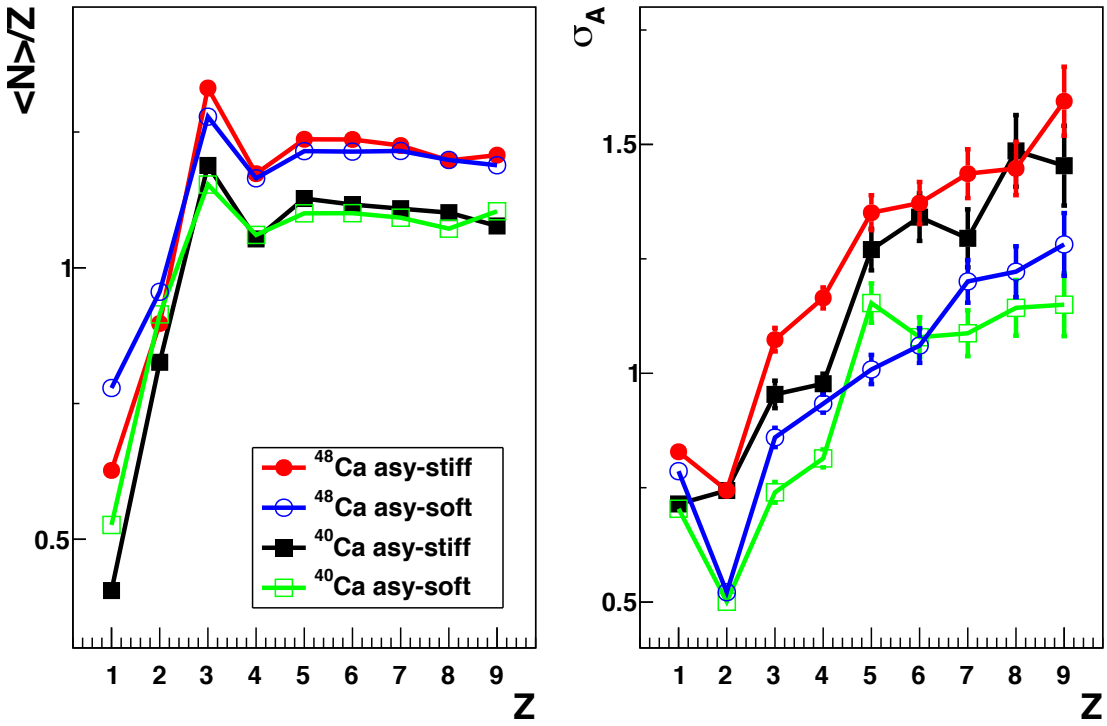


**Figure 4.5:** *Left panel: <N>/Z vs Z of the neck emissions observed in coincidence with a QP and QT. Right panel: the $\sigma_A$ of the same neck emissions as a function of the charge Z.*

the system. No significant dependence on the symmetry energy parametrization can be observed, except for $Z = 1$. On the contrary, there is a clear dependence on the asy-stiffness of the $\sigma_A$ value, with the asy-stiff case producing wider isotopic distribution. This observable seems a good candidate to give information on the symmetry energy term.

To investigate the capability of the AMD code of reproducing the isospin drift effect (see Sec. 1.2.2) we studied the <N>/Z of different particles as a function of their velocity along the beam direction ($V_Z$), see fig. 4.6. In principle, three different sources can be hypothesized for the particles of fig. 4.6:

- particles forward emitted in the CM frame in the QP rapidity region, which may come from the QP decay;
- particles backward emitted in the CM frame in the QT rapidity region, mainly associated to the fast QT decay;
- particles emitted in the the mid-rapidity region, which are produced during the neck fragmentation.

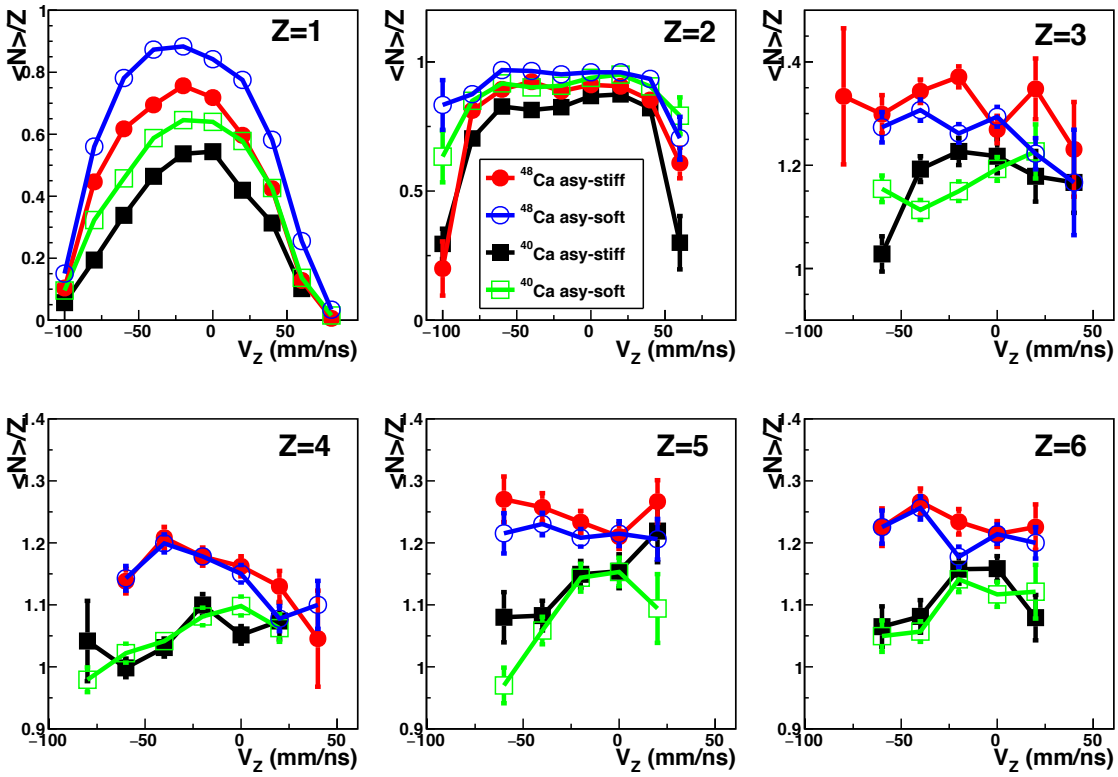


**Figure 4.6:** *<N>/Z ratio of the different particles from $Z = 1$ (top-left panel) up to $Z = 6$ (bottom-right panel) as a function of the velocity along the beam direction ($V_Z$). The different colours and markers correspond to the different symmetry energy term parametrizations and targets illustrated by the legend.*

The particles emitted by these different sources are affected by the neutron content of the emitting source. Fig. 4.6 shows the <N>/Z vs $V_Z$ plot for particles from $Z = 1$ up to $Z = 6$. First of all we can see that, with the possible exception of $Z = 2$, where the $\alpha$ particles always dominate, the <N>/Z ratio is always higher for the $^{48}$Ca case than for the $^{40}$Ca case. The main reason for this effect is obviously the higher number of available neutrons when the target is neutron-rich. However, there is also a clear effect of isospin diffusion, more evident for $Z \geq 4$: in fact the <N>/Z for the $^{48}$Ca case tends to increase with respect to the QP region moving towards the QT rapidity, while it decreases in the QT region for the $^{40}$Ca target. For $Z = 1$, an effect of neutron enrichment in the mid-velocity region, possibly due to the isospin drift, is clearly seen. Such an effect gets weaker as the charge of the ejectile increases. In fact, by looking carefully at the $^{40}$Ca data, a small bump in the mid-velocity region can be recognized for $Z = 4$, $Z = 5$ and $Z = 6$. Some sensitivity to the symmetry energy parametrization can be observed for the $Z = 1$ case, marginally surviving for $Z = 2$ and $Z = 3$ (by the way, the stiff case gives higher <N>/Z for $Z = 2$ and $Z = 3$ while the opposite is true for $Z = 1$). No

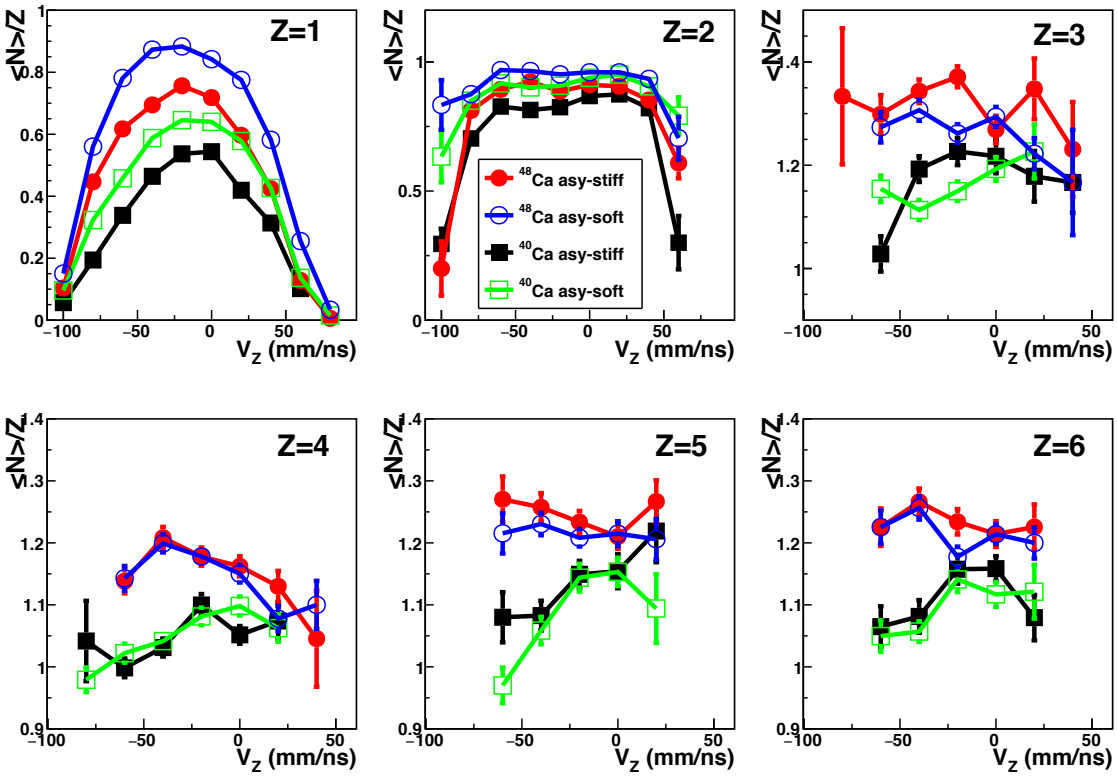


**Figure 4.7:** *Yield of ratios between different isotopic couples in coincidence with a QP as a function of the $V_Z$ velocity in the CM For all the panels the coloured curves correspond to the different symmetry energy term parametrizations as described in the legend.*

sensitivity at all is present for higher Z. Moreover, the effect of the secondary de-excitation, not included in fig. 4.6, tends to reduce all the differences and also the absolute values of <N>/Z.

To look further into the effects of isospin drift and their dependence on the stiffness, in fig. 4.7 the isotopic ratio between different pairs of light nuclei have been reported, as a function of their velocity in the beam direction. The different model parametrizations are plotted with different colors as described in the legend. Only for the d/p and t/p ratios it is possible to observe an effect of the isospin drift as a maximum of the ratio at about $V_Z = 0$, since this corresponds to a larger production of heavier isotopes. In such ratios some differences between the asy-stiff and asy-soft parametrizations can be also observed, coherently with fig. 4.6. On the contrary, all the isotopic ratios involving the $\alpha$ particles show a very similar behaviour without appreciable effects of isospin drift or stiffness dependence. In the case of the ratio $^7Li/^7Be$ only a weak dependence on the stiffness can be observed for $^{40}$Ca.

## 4.2 GEMINI statistical code

GEMINI is one of the most used statistical code in the nuclear physics community. This code has been developed by R. J. Charity [5] with the goal of describing the decay of excited nuclei in a large range of energies, angular momenta, and sizes. In this thesis we use the improved version of the original code called GEMINI++ [74] and implemented in C++ rather than in FORTRAN.

GEMINI++ accepts as input a nucleus with charge Z, mass A, angular momentum J and excitation energy $E^*$. Such a nucleus is usually one of the primary reaction products coming from the dynamic simulation code. The GEMINI++ code is run for each primary fragment to obtain all the secondary fragments which can then be compared with the experimental data.

The de-excitation of a primary fragment, treated as a compound nucleus, proceeds as a sequence of binary decays until the emission of particles is energetically forbidden or it is negligible with respect to the contribution of other de-excitation processes. The introduction of this general binary decay is necessary to describe the complex fragment formation or a fission process. In fact GEMINI++, at variance with some other statistical models [91], includes fission as possible de-excitation channel in addition to the evaporation of light particles. In GEMINI++ the emission of light particles is described by the Hauser-Feshbach evaporation formalism [24]. In light systems and for asymmetric fission in heavier system the Moretto's binary decay formalism [92] is used. Otherwise the total fission yield is obtained by the Bohr-Wheeler formalism [93].

The complete GEMINI++ description of the evaporation process requires the introduction of several parameters. A standard set of parameters is provided as default value and it was carefully tuned by the author of the code in order to reproduce experimental data coming from complete fusion reactions [74]. To fit experimental light-particle kinetic energy spectra, some thermal fluctuations of the Coulomb barrier distribution have been introduced. The barrier fluctuations may be due to fluctuations of the compound nucleus shape and/or of its density and/or of its surface diffuseness. Level densities are given by the Fermi-gas formula:

$$\rho(E^*, J) \sim \exp\left(2\sqrt{a(U)U}\right) \tag{4.5}$$

where U is the thermal excitation energy after subtraction of the pairing, rotational, and deformation energy contributions. To reproduce the strong fluctuations due to shell effects observed in the density level parameter, GEMINI++ uses the following

parametrization for the $a(U)$:

$$a(U) = \tilde{a}\Big[1 - tanh\Big(\frac{U}{\eta} + \frac{J}{J_n}\Big)\frac{\delta W}{U}\Big] \tag{4.6}$$

where $\delta W$ is the shell correction to the liquid-drop model, $\tilde{a}$ is a smoother level density parameter and $\eta$ and $J_n$ are free parameters. Taken into account the influence of the long-range correlations to the single particle level densities, the smoother parameter $\tilde{a}$ can be replaced by an effective parameter $\tilde{a}_{eff}(U)$ considering the excitation energy dependence of the level density:

$$\tilde{a}_{eff}(U) = \frac{A}{k_\infty - (k_\infty - k_0)\exp\Big(-\frac{k}{k_\infty - k_0}\frac{U}{A}\Big)} \tag{4.7}$$

GEMINI default parametrization uses $k_0 = 7.3\,\mathrm{MeV}$ and $k_\infty = 12\,\mathrm{MeV}$. The $k$ parameter defines the dependence of $\tilde{a}$ with respect to the energy and it is essentially zero for nuclei with $A < 100$, increasing roughly exponentially with A for heavier nuclei.

The capability of GEMINI++ to describe the statistical fission is a key feature in view of the physics goal of this work and of the comparison with the dynamical fission process. In order to obtain a good reproduction of the fragment de-excitation process a fine tuning of the parameters (such as thermal fluctuations widths, $k_0$ or fission delay time $\tau_f$) is important. In this thesis, however, we use the default values. In fact, in the ISO-FAZIA experiment, only very dissipative collisions, in which the excitation energy of the primary fragments is larger than the typical values at which Gemini is used ($E < 2.5\,\mathrm{MeV/u}$) can be observed. Moreover, the primary fragments are not really equilibrated sources perfectly comparable to a compound nucleus. A residual memory of the entrance channel, especially in fast fission process, may be anyway present. In this scenario, a fine tuning of the model parameters is scarcely constraining.

## 4.3 Heavy Ion Phase Space Exploration (HIPSE)

HIPSE is a phenomenological model dedicated to Heavy-Ion reactions at Fermi energies [94, 95]. HIPSE falls somewhat in between the two extreme approaches of the statistical models and of the microscopic transport models. It is defined as "a phenomenological event generator allowing a detailed comparison with experimental data and accounting for both dynamical and statistical effects" (cit. [94]).

The description of an event is divided in three steps:

1. **the approaching phase**. For a given beam energy $E_B$ a classical two-body

dynamics is assumed to describe the approaching phase of the two nuclei. Indicating with $R$ the nuclear radius, the potential used for $r \geq R_{projectile} + R_{target}$ consists of a Coulomb term $V_c(r)$, calculated assuming two uniformly charged spheres, and a nuclear term $V_N(r)$ corresponding to the proximity potential [96]. The potential dependence on the beam energy is phenomenologically taken into account by choosing the correct value of $V(r = 0) = \alpha_a V_{A_T A_P}$, where $V_{A_T A_P}$ is a tabulated value [94] and $\alpha_a$ is a free parameter of the model which keeps into account the lack of knowledge of the nucleus-nucleus potential at large overlap.

2. **the fragment formation phase**. The maximum overlap between the two partners depends on the impact parameter and on the value of $\alpha_a$. The nucleons inside the projectile and the target are sampled through a Metropolis algorithm, assuming a symmetrical geometry and taking into account the Pauli blocking. As a starting point to describe the reaction, a participant-spectator picture is used [13, 14], which considers the nucleons outside the overlap region as Quasi-Projectile (QP) and Quasi-Target (QT). In order to keep into account the experimental observation of a strong deviation from such a simplified approach, an exchange of a fraction $x_{tr}$ of nucleons from QP and QT to the overlap region is allowed. The possible formation of composite clusters at mid-rapidity from the available nucleons in the overlap region is tested. If energy and momentum conservation laws are satisfied for the new cluster, the fragment is built and its position and momentum are recalculated.
   Nucleon-nucleon collisions are also taken into account. The number of these collisions is defined as a fraction $x_{coll}$ of the total number of nucleons in the overlap region $A_{over}$: $N_{coll} = x_{coll} A_{over}$. The collisions occur in the participant region and an averaged nucleon-nucleon cross section ($\sigma_{eff}(E_b)$) is used: $x_{coll}$ and $\sigma_{eff}(E_b)$ are free parameter of the model. During the collision, the two nucleons exchange momentum, losing memory of the entrance channel and leading to the formation of a composite state.
   At the end of this step we obtain all the fragments, including the QP and the QT, together with their kinematical quantities. This time is considered the $t = 0\,\mathrm{fm/c}$ of the dynamics.

3. **the exit channel and the after-burner phase up to detectors**. Up to $50\,\mathrm{fm/c}$ the fragments are propagated under the effect of the Hamiltonian $H = \sum \frac{P_i^2}{2mA_i} + \sum_{i<j} \mathbf{V_{A_i} A_j}(|\mathbf{R_i} - \mathbf{R_j}|)$. The standard Woods-Saxon potential is considered for the nuclear interaction. Then, when the system configuration is less compact, a test of possible cluster fusion or reaggregation is performed. The system is propagated until the potential energy becomes positive ($E_{pot} >$

0). This condition corresponds to the end of the dynamic phase and the beginning of the de-excitation phase dominated by the Coulomb interaction. The total energy balance in the center of mass is given by $E_0 = Q + E_{kinetic} + E_{pot} + E^* + E_{rot}$ where Q is the Q value of the reaction, $E_{rot}$ is the sum of the rotational energies and $E^*$ is the excitation energy of the fragments.
The propagation of the excited fragments in the Coulomb field is performed by means of SIMON [97], which is an afterburner code based on the statistical model. SIMON takes into account all the possible decay channels from neutron evaporation up to symmetric fission.

The HIPSE model offers a complete dynamical description of the nuclear reactions, considering all the particles emitted from the very early stage of the collision up to the statistical de-excitation of the secondary decay fragments. It uses only three important free parameters: the percentage of nucleons transferred between the projectile and the target $x_{tr}$, the potential hardness $\alpha_a$ and the nucleon-nucleon collision percentage $x_{coll}$. The validity of the hypothesis used in this phenomenological model are limited to the Fermi energy range and deviations between the model and the experimental data are expected for a beam energy above 100 MeV/u.

## 4.4 Geometric filter

In order to perform a correct comparison between the simulated secondary events and the experimental data, a "geometric filter" which reproduces via software the geometrical coverage and the detection efficiency of the used apparatus is needed. This requirement is especially important in the ISO-FAZIA experiment due to the reduced angular acceptance. The geometric filter also takes into account the energy thresholds for the different used identification techniques (see Sec. 2.4). Apart from the completely operational detectors, also the partially working detectors (see fig. 3.5 of Chapter 3) are taken into account in order to reproduce the actual efficiency of the apparatus.

The secondary events produced by GEMINI++ are filtered to obtain calculated quantities directly comparable to the experimental data. In fig. 4.8 the number of fragments $N_{frag}$ with $Z > 5$ has been reported in black for the complete $4\pi$ simulation (AMD + GEMINI++) and in red after applying the geometric filter. Due to the small angular coverage of ISO-FAZIA experimental apparatus, a sizeable fraction of the reaction products cannot be detected and consequently the two distributions appear very different. A sizeable reduction of the fragment multiplicity is evident, thus showing the importance of the geometric filter in order to compare the experimental and the simulated data. The same observation justifies the impossibility

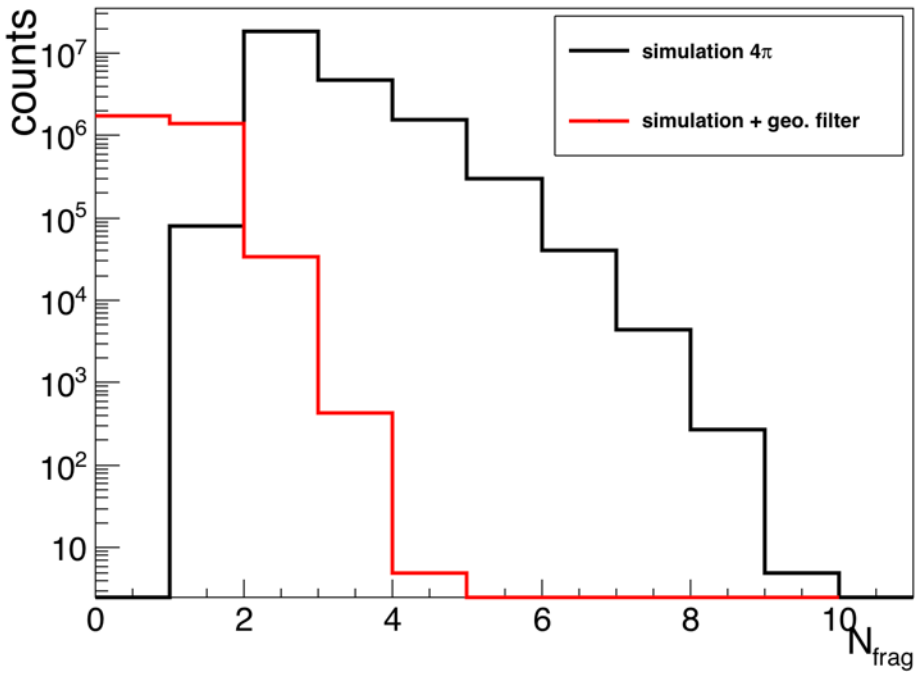


**Figure 4.8:** *Multiplicity spectra of fragments $N_{frag}$ for $^{48}Ca$ as a target for the complete $4\pi$ simulation (AMD + GEMINI++) before (black) and after (red) applying the geometrical filter.*

of exploiting global variables or the common event selection techniques in order to classify the different reaction mechanisms.

# Chapter 5

# Data analysis: event selection

After the calibration and identification procedure, described in detail in Chapter 3, the events accepted for the following analysis contain at least one particle identified in charge (and in mass when possible). The information about the number of identified particles for each event is expressed by the multiplicity parameter $M$. From the measured kinetic energy of each reaction product, we can obtain its velocity, either by means of the true mass (when available) or by means of the mass estimated according the the EAL parametrisation (see Sec. 1.1.2) [10]. In order to evaluate the different components of velocity and momentum some knowledge of the trajectory of the particle (e.g. expressed in cylindrical coordinates) is also needed. The granularity of the FAZIA blocks (every telescope covers a solid angle of 62 msrad around the beam axis) allows for obtaining the angular information on the trajectory of the detected particles with an uncertainty of $\pm 0.7°$ in polar angle and a variable uncertainty between $\pm 2.4°$ and $\pm 16.6°$ in azimuthal angle, respectively for the largest and the smallest polar angles covered by the apparatus.

## 5.1 Preliminary selection

The ISO-FAZIA experiment is aimed at observing forward emitted reaction products, in order to study the isotopic composition of the QP and of the related fragments. During the entire ISO-FAZIA experiment the trigger multiplicity was set to $M = 1$, since an hardware problem on the FEE prevented to acquire data with higher multiplicity triggers. In fig. 5.1 the multiplicity spectra for both the studied systems (in black $^{48}$Ca and in red $^{40}$Ca) are shown. In order to remove from the analysis the elastic scattering events only the events with multiplicity $M > 1$ have been accepted (shaded area in fig. 5.1); indeed, in the case of elastic scattering, the recoiling target nucleus could not be detected. In fig. 5.1 the total event number and that with $M > 1$ for both spectra are reported. Rejecting all the events with $M = 1$

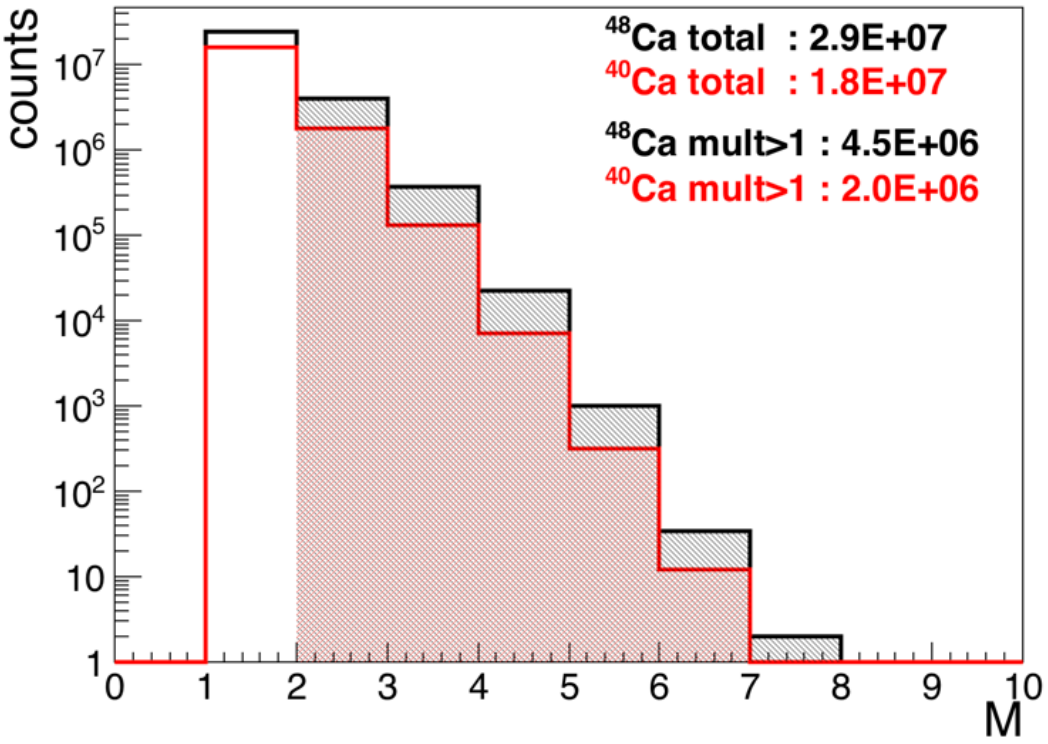


**Figure 5.1:** *Multiplicity spectra for both targets: in black $^{48}Ca$, in red $^{40}Ca$. The total integral of the spectra and the integral corresponding to $M>1$ events are also reported. The shaded areas corresponds to the events with $M>1$ accepted for the analysis .*

the statistics has been reduced to about 15% for the $^{48}$Ca target and to about 10% for the $^{40}$Ca target.

In order to discard spurious events, some consistency conditions have been introduced. Since there are events in which the total collected charge $Z_{tot}$ (the total charge summed over all the detected particles) is larger than the maximum charge of the system $Z_{sys} = Z_p + Z_t = 56$, we require the rejecting condition to be satisfied: $Z_{tot} \leq Z_{sys}$. Furthermore, for every detected fragment, consistency of the partial energy deposited in the different telescope layers with the total measured energy is required. The total energy of each particle is experimentally given by the sum of the energies deposited in each detection layer. Thanks to the energy loss tables [76], starting from the total energy, and knowing Z and A, it is possible to calculate the expected energy deposited in each layer. The particle is accepted only if the difference between the experimental and the calculated energy for each layer is within 0.1 MeV. Applying these two cuts, only 0.1% of the total collected events are discarded.

## 5.2 General overview of data

In the left panel of fig. 5.2 the correlation between the charge (Z) and the velocity in the laboratory frame ($V_{lab}$) for every detected particle, for the events with M > 1, is shown for the reaction on the $^{48}$Ca target; the figure extends down to $Z = 1$. The two arrows in the plot represent the CM velocity ($V_{CM}$) and the beam velocity ($V_{beam}$) respectively. The correlation is similar to those observed in many previous experiments carried out at Fermi energies [40, 98, 99]. An enhancement of the statistics in the QP region (Z slightly lower than the projectile's charge and velocity close to the beam velocity) is evident, as expected. The additional information coming from the PSA technique (see Sec. 2.3 and Ref. [11]) allows for a reduction of the identification velocity thresholds with respect to previous studies, thus giving access to the velocity region well below the CM velocity. We also notice the presence of relatively heavy fragments at velocity close to $V_{CM}$. In the right panel fig. 5.2 the same correlation for the AMD simulation, performed with the stiff parametrisation, and GEMINI++ as afterburner is shown for the sake of comparison. The simulation reproduces well the general features of the experimental correlation; however, we observe an evident underestimate of heavy fragments with velocity close to the CM velocity.

In fig. 5.3 the projections on the x-axis (left panel) and y-axis (right panel) of the two correlations of fig. 5.2, corresponding to the $V_{lab}$ and Z distribution respectively, are shown using black points for experimental data and red points for the simulation. The two experimental distributions are overall fairly well reproduced by the simulation except for a slightly different behaviour of LCPs. Indeed the simula-

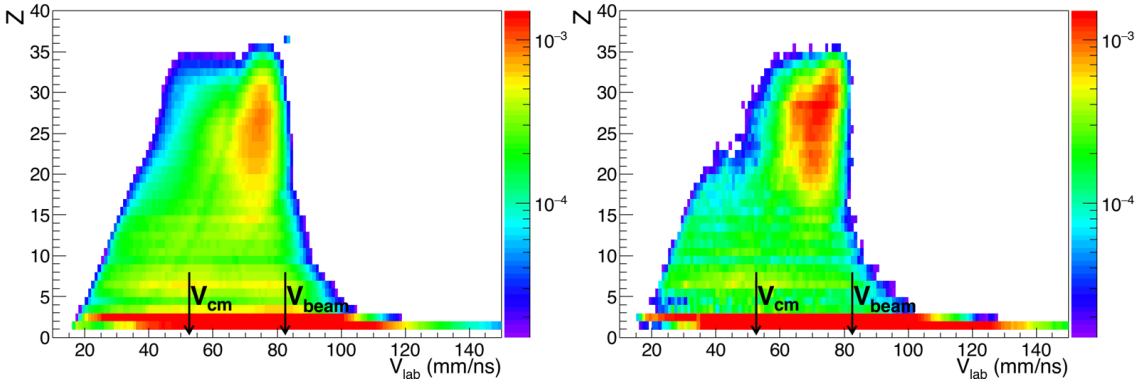


**Figure 5.2:** *In figure the correlations between the charge Z and the velocity in the laboratory frame ($V_{lab}$) are shown; left panel: experimental data; right panel: simulated events with using the AMD code (asy-stiff parametrization) plus GEMINI++. Only particles for M > 1 events have been included in the plot. The two correlations have been normalized to their integral.*

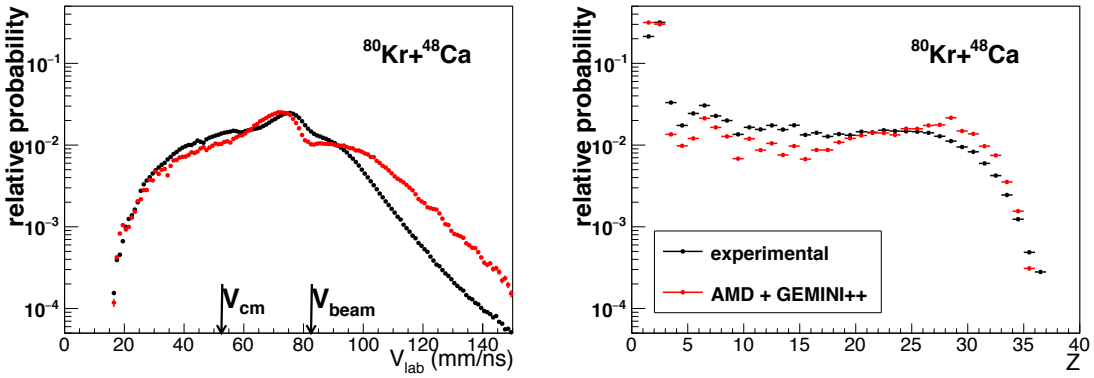


**Figure 5.3:** *In the left (right) panel the $V_{lab}$ (Z) distribution of the detected particles corresponding to the x-projection (y-projection) of the Z vs $V_{lab}$ correlations of fig. 5.2 is shown. In both panels the experimental data are drawn with black points and the simulation data with red points.*

tion presents a harder tail at high velocities corresponding to an overproduction of energetic protons, above 90 mm/ns.

## 5.3 Selection of the reaction mechanisms

In order to study the different reaction mechanisms, we need to classify and characterize the collected events. We recall here some definitions: we label "fragments" or IMF (Intermediate Mass Fragments) the particles with $Z \geq 3$ and LCP (Light Charged Particles) the particles with $Z < 3$, e.g. isotopes of Hydrogen and Helium.

The collected events have been sorted into three main classes of reaction already described in Chapter 1:

- **Central Collisions (CC)**: these reactions are characterized by the presence of a main heavy fragment (possibly the remnant of an excited system like an evaporation residue coming from an incomplete fusion process) located at velocities close to that of the CM, or by the presence of some heavy IMF (fragments produced in a multi-fragmentation reaction) again close to the CM velocity. The limited solid angle coverage of the four FAZIA blocks prevents an accurate characterization of these central events.

- **Deep Inelastic Collisions (DIC)**: these reactions are characterized by the presence of two heavy fragments corresponding to the quasi-projectile (QP) and the quasi-target (QT). The QP is focused in the forward direction with velocities close to the beam velocity and the QT fragment is emitted in the backward direction in the CM frame with velocities below that of the CM Due to the low energy threshold for detection and to the reduced angular coverage

of the ISO-FAZIA experiment, the detection of the QT is strongly suppressed, especially for the less violent collisions. For this reason the selection of the DIC events has been divided in two sub-classes: **QP-only** if only the QP is detected, **QP-QT** when both DIC fragments are detected in coincidence.

- **Quasi-Projectile fission (QP-FIS)**: these reactions are characterized by the presence of two fragments with the sum of their charges close to the QP charge and with relative velocities compatible with the fission systematics [100].

The events selection procedure is of course the same for both systems (target of $^{48}$Ca and $^{40}$Ca); moreover the two reactions are quite similar so that their general features are expected to be quite similar. For this reason in this section we show the results only for the system with larger statistics ($^{48}$Ca), showing the correlations for $^{40}$Ca only in some specific interesting case. Furthermore, we always show the model predictions obtained running the AMD code with an asy-stiff parametrization of the symmetry energy term (it offers a better agreement with the experimental data as it will be discussed later on in Chapter. 6) plus GEMINI++ as afterburner. All simulation events presented in this and in the following Chapter, unless otherwise specified, have been filtered through the geometric filter of the apparatus (see Sec. 4.4).

For the sake of clarity, a flowchart of the event selection procedure has been sketched in fig. 5.4. The various types of reaction mechanisms are described in detail in Sec. 5.3.2 and Sec. 5.3.3.

### 5.3.1 Study of the $\theta_{flow}$ angle

A very useful tool to distinguish the different reaction mechanisms occurring in a heavy system at Fermi energy is the flow angle $\theta_{flow}$ [101].

In order to obtain $\theta_{flow}$, the construction of the momentum tensor $T_{ij}$ is required:

$$T_{ij} = \sum_{n=1}^{M} \frac{p_i^n \cdot p_j^n}{p^n} \qquad with \qquad (i,j = 1,2,3) \tag{5.1}$$

where $p_i^n$ and $p_j^n$ are the $i$-th and $j$-th Cartesian component of the momentum $\vec{p^n}$ in the CM frame of the *n-th* fragment of the event. Diagonalizing the $T_{ij}$ tensor, three eigenvalues $\lambda_i$ and three eigenvectors $\vec{e_i}$ are found. The $\theta_{flow}$ is defined as the angle between the eigenvector $\vec{e_i}$ corresponding to the largest eigenvalue $\lambda_i$ and the beam direction $\hat{u}$:

$$\theta_{flow} = arcos(|\vec{e_i} \cdot \hat{u}|) \tag{5.2}$$

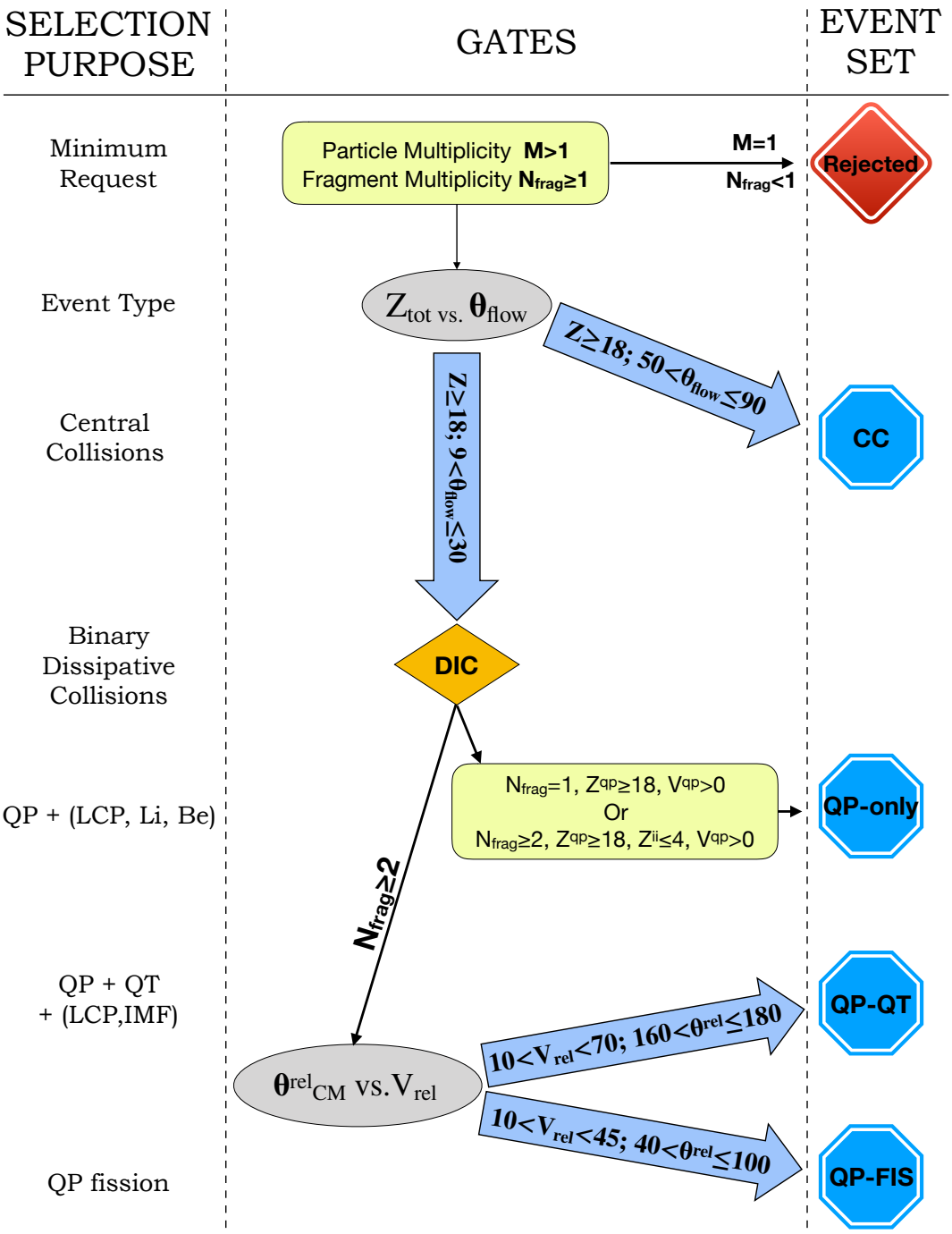


**Figure 5.4:** *A sketch of the flowchart of the event selection procedure is reported. Starting from the minimal request to process an event, the correlation used to classify them are reported together with the label associated to each event set. Details about the selection procedure are given in the text.*

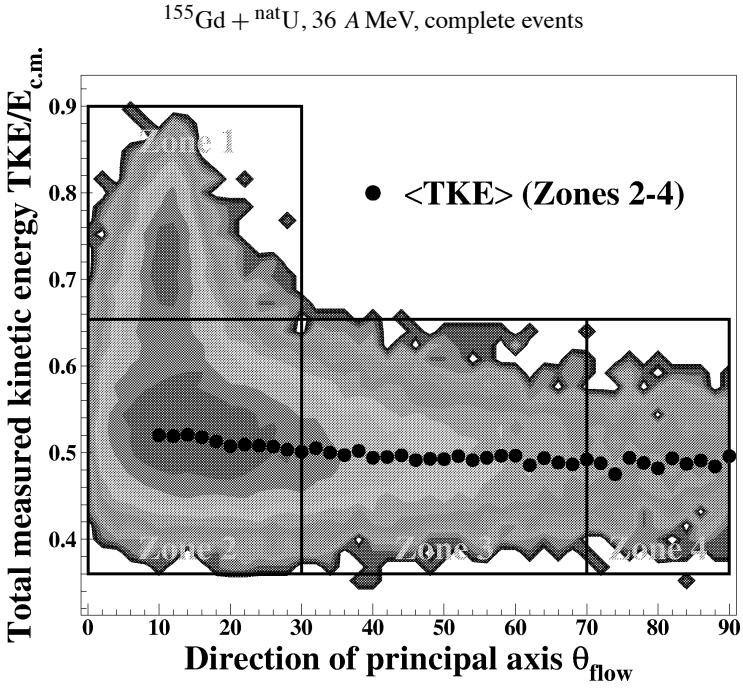


Fig. 7. 'Wilczyński diagram' for complete events: logarithmic intensity scale representing measured cross section as a function of total measured c.m. kinetic energy (as a fraction of the available centre of mass energy) and 'flow' angle or direction of the event principal axis, $\theta_{\rm flow}$. The four zones indicated are used to classify complete events (see text). For events in Zones 2 to 4 the mean value of TKE is indicated (points) for each $\theta_{\rm flow}$ bin.

**Figure 5.5:** *Figure and caption taken from J. D. Frankland* et al.*, Nuclear Physics A 689 (2001) [103].*

The flow angle is a good observable to sort the different class of events, as shown in previous studies [102–104]. In fig. 5.5, taken from the paper of J. D. Frankland *et al.* [103], the authors show the correlation between the Total Kinetic Energy (TKE) and the $\theta_{flow}$ for the reaction $^{155}\mathrm{Ga} + {}^{nat}\mathrm{U}$ at 36 MeV/u studied with the INDRA detector [42]. While the strongly dissipative collisions show a flat distribution in $\theta_{flow}$, the more peripheral collisions are located mainly at low angles. This means that the $\theta_{flow}$ is related to the degree of dissipation in the collisions.

In particular, the $\theta_{flow}$ dependence on the impact parameter b has been investigated by means of the AMD simulation. In the left panel of fig. 5.6 the correlation b vs $\theta_{flow}$, normalized to the integral, is shown for all simulated events (without geometric filter). The model predictions are in good agreement with previous observations confirming the dependence of $\theta_{flow}$ on the centrality: a flat distribution for central collisions and a peaked behaviour for semi-peripheral reactions.

$\theta_{flow}$ is a global observable which is usually employed when the geometrical coverage of the experimental apparatus is large. In fact the more complete is the event, the higher is the sorting capability of $\theta_{flow}$. Here we want to prove the

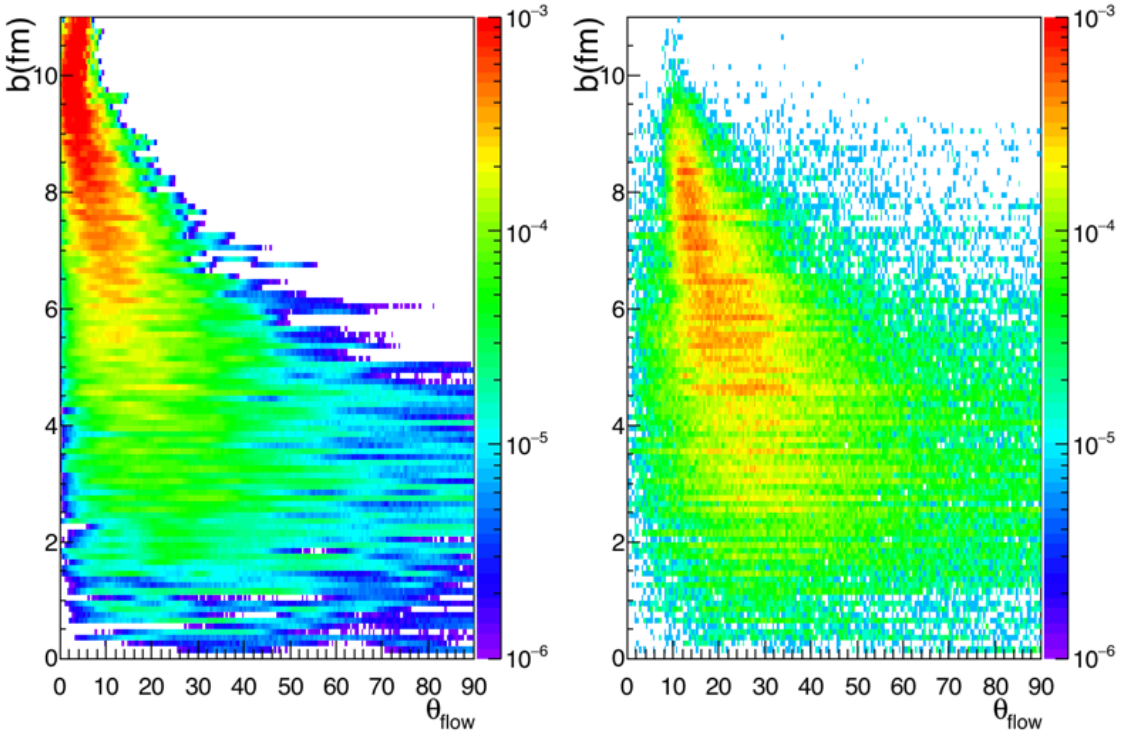


**Figure 5.6:** *Correlation between the impact parameter of the reaction and the $\theta_{flow}$ evaluated on the event with multiplicity $M \geq 2$ for simulated data. In the left panel the complete $4\pi$ simulated data are shown, while in the right panel the same data are reported after the application of the geometric filter (see Sec. 4.4) which reduce the initial statistics to about 2%.*

reliability of this observable when used with our reduced angular coverage apparatus. In the right panel of fig. 5.6 the b vs $\theta_{flow}$ graph is shown after applying the geometric filter (see Sec. 4.4). The main effects of the geometric filter are a cut at large impact parameters and a slight spread of the distribution along the $\theta_{flow}$ axis. However, the general behaviour of the correlation is preserved and thus its capability to distinguish between more peripheral and more central events. This surviving selectivity of the $\theta_{flow}$ is in some sense expected, considering that in the case of low multiplicity events $\theta_{flow}$ corresponds to the direction of the biggest fragment ($\theta_{big}$) with respect to the direction the beam axis. This is demonstrated by the narrow correlation $\theta_{flow}$ vs $\theta_{big}$, shown in the left panel of fig. 5.7 for the $^{48}$Ca target. The mean value of the absolute difference, calculated event by event, between the two angles $\theta_{flow} - \theta_{big}$ has been reported as a function of the multiplicity parameter M in the right panel of fig. 5.7. The error bar reported in the figure is the statistical error associated to the experimental counts. We can observe that the highest the multiplicity, the highest the difference between these two quantities and thus, in the case of events

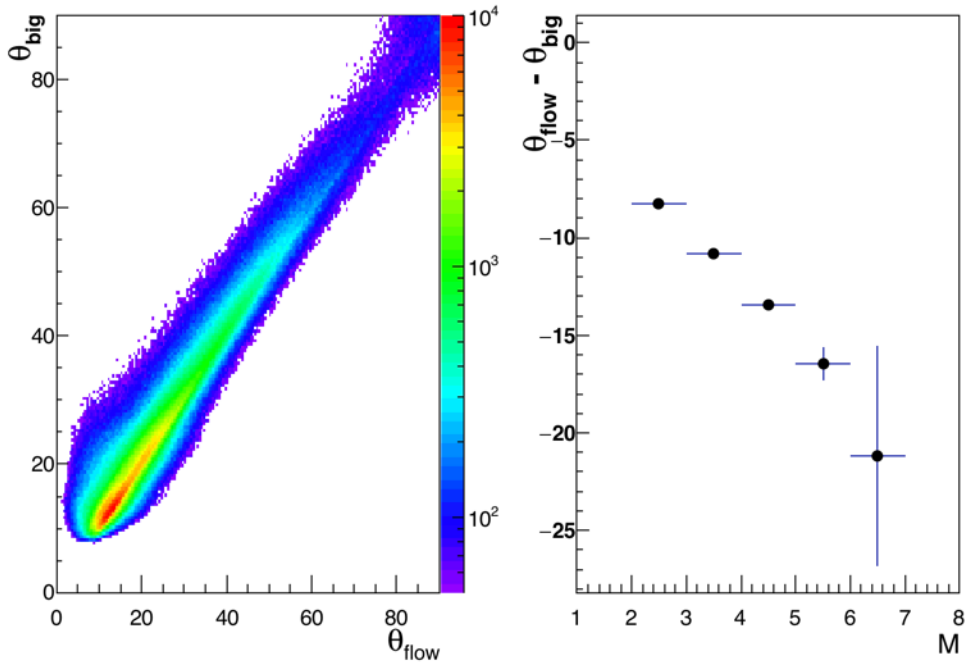


**Figure 5.7:** *In the left panel the correlation between $\theta_{big}$ (the angle between the direction of the biggest fragment and the beam axis) and $\theta_{flow}$ is shown. In the right panel the mean value of the absolute difference between $\theta_{flow}$ and $\theta_{big}$ is reported as a function of the event multiplicity. Only the statistical error contributes to the error bars reported in the right panel.*

with multiplicity $M > 1$ the use of $\theta_{flow}$ is always preferred with respect to $\theta_{big}$.

### 5.3.2 CC events

A first event selection is performed by exploiting the correlation between total detected charge $Z_{tot}$ and $\theta_{flow}$ under an additional condition on the fragment number, i.e. $N_{frag} \geq 1$. In fig. 5.8 the experimental $Z_{tot}$ vs $\theta_{flow}$ correlation (left panel) is compared with the simulation (right panel). Also in this case the model reproduces in a satisfying way the general shape of the correlation.

The red right in fig. 5.8 represents the gate used to select the **CC** events: $18 \leq Z \leq Z_{tot}$ and $50 < \theta_{flow} \leq 90$. In fig. 5.9 the Z vs $V_{lab}$ correlation for the biggest fragment of a CC events is shown for experimental (left panel) and simulated (right panel) data. The two arrows represents the CM velocity ($V_{CM}$) and the beam velocity ($V_{beam}$) respectively. We observe that the correlation is distributed around $V_{CM}$ and that it widely spread in Z (range in $Z = 10 \div 37$).

Another indication of the centrality of this selection is given by the the velocity distribution of particles in coincidence with the biggest fragment. In fig. 5.10 we

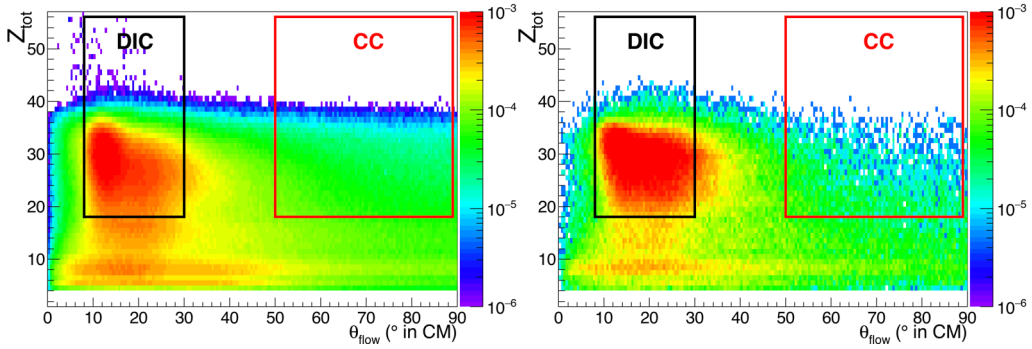


**Figure 5.8:** *Correlation between the total detected charge $Z_{tot}$ and $\theta_{flow}$. The left panel shows the experimental correlation and the right panel the AMD+GEMINI++ simulation. The black left rectangle corresponds to the selection of less dissipative collisions, the red right rectangle corresponds to more central collisions. The two plots are normalized to their integrals.*

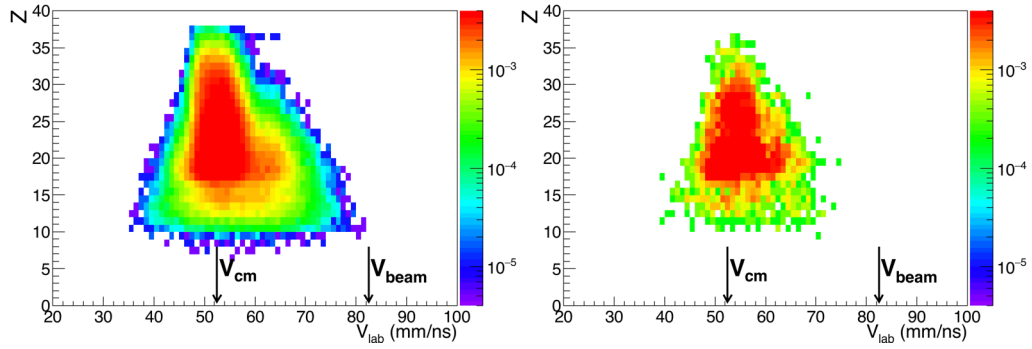


**Figure 5.9:** *For CC events, correlations between the charge Z and the velocity in the laboratory frame $V_{lab}$ of the biggest detected fragment are shown: left panel, experimental data; right panel, simulation. The two plots are normalized to their integrals.*

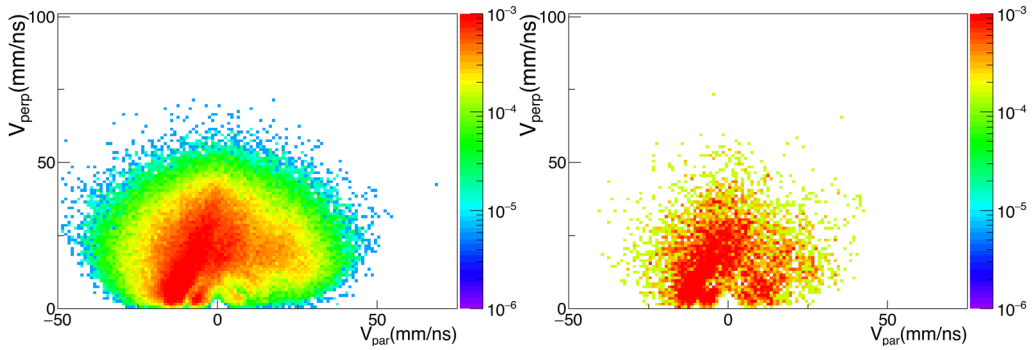


**Figure 5.10:** *Central events (CC): correlation $V_{par}$ vs $V_{perp}$ of the velocity components of $\alpha$ particles with respect to the QP direction in the CM Left (right) panel: experimental (simulated) data. The correlations are normalized to their integral.*

show the $V_{par}$ vs $V_{perp}$ plot for $\alpha$ particles ($\alpha$ particles are produced with the largest yield): $V_{par}$ and $V_{perp}$ are the velocity components with respect to the QP direction in the CM reference. The experimental data show a single emitting source centered around the center of mass as expected in a central collision. The yield thickenings and clusters seen in the data are due to the discontinuous geometric efficiency. These effects are correctly taken into account in the simulation which rather faithfully reproduce the shape of the distribution. The low statistics, as already said before, is the consequence of the scarce production of this type of central collisions in the model.

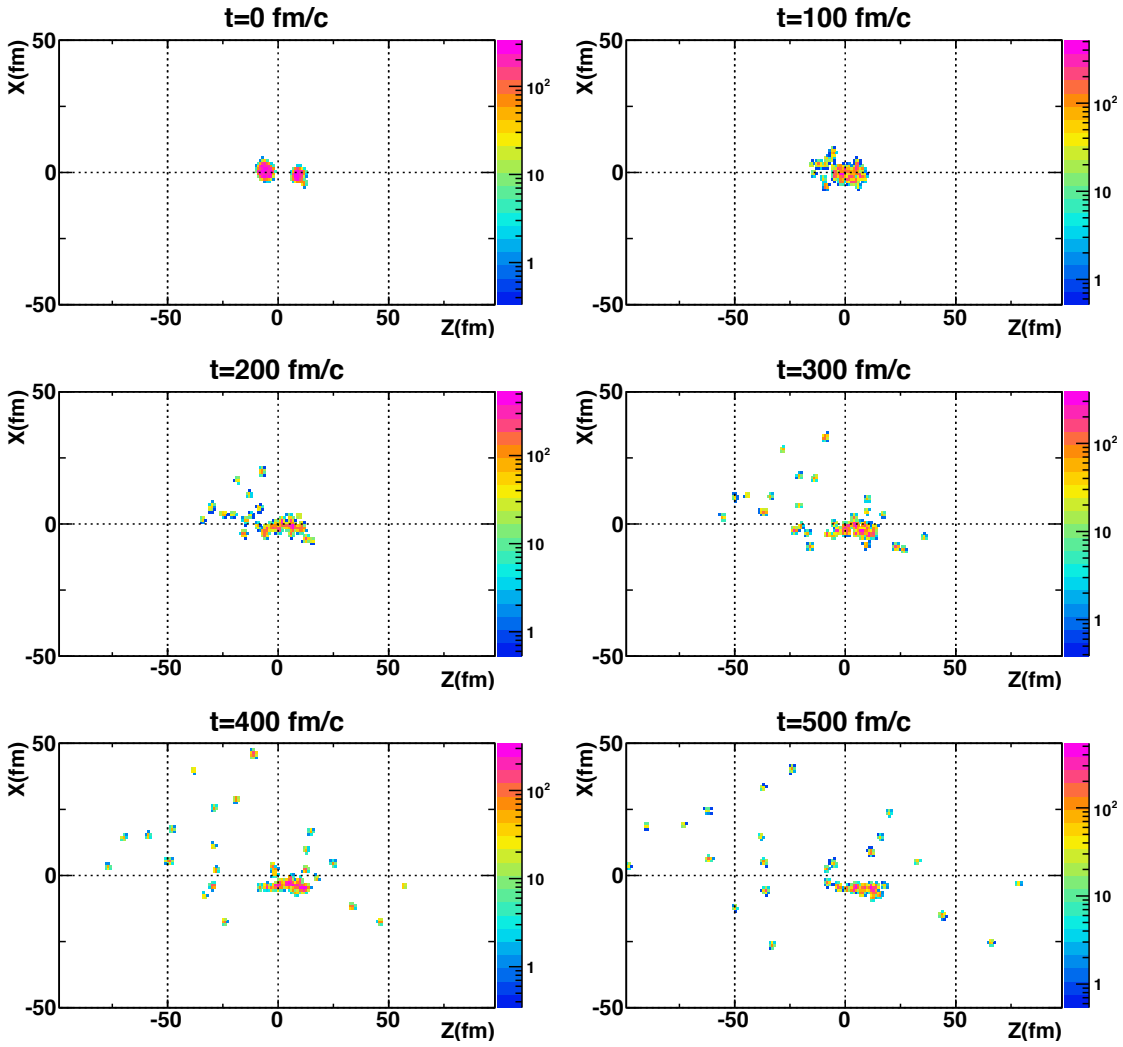


**Figure 5.11:** *Time evolution of a simulated central event (impact parameter $b = 1.6\,fm$) modelled with the AMD code. Six spatial X-Z density distributions are reported (Z axis is the beam direction), taken at different times (in fm/c) up to 500 fm/c. The shown event satisfies the condition for the CC selection and corresponds to a kind of incomplete fusion event. The colour scale corresponds to the density distribution of the nucleon gaussian packets.*

The simulation reproduces realistically the experimental correlation and gives us the possibility to figure out the topology of the selected class of events. Going through the simulated events, we verified that two main event types satisfy the CC condition:

- A primary big fragment (i.e. a hot pre-evaporation fragment) is accompanied by some LCP or light IMF. In fig. 5.11 the time evolution (up to 500 fm/c) of a representative simulated event of this kind is shown. It is a very dissipative collision that can be interpreted as an incomplete fusion with only one big deformed fragment at the end of the dynamical phase. The incomplete fusion mechanism for this kind of systems was indeed already observed in the

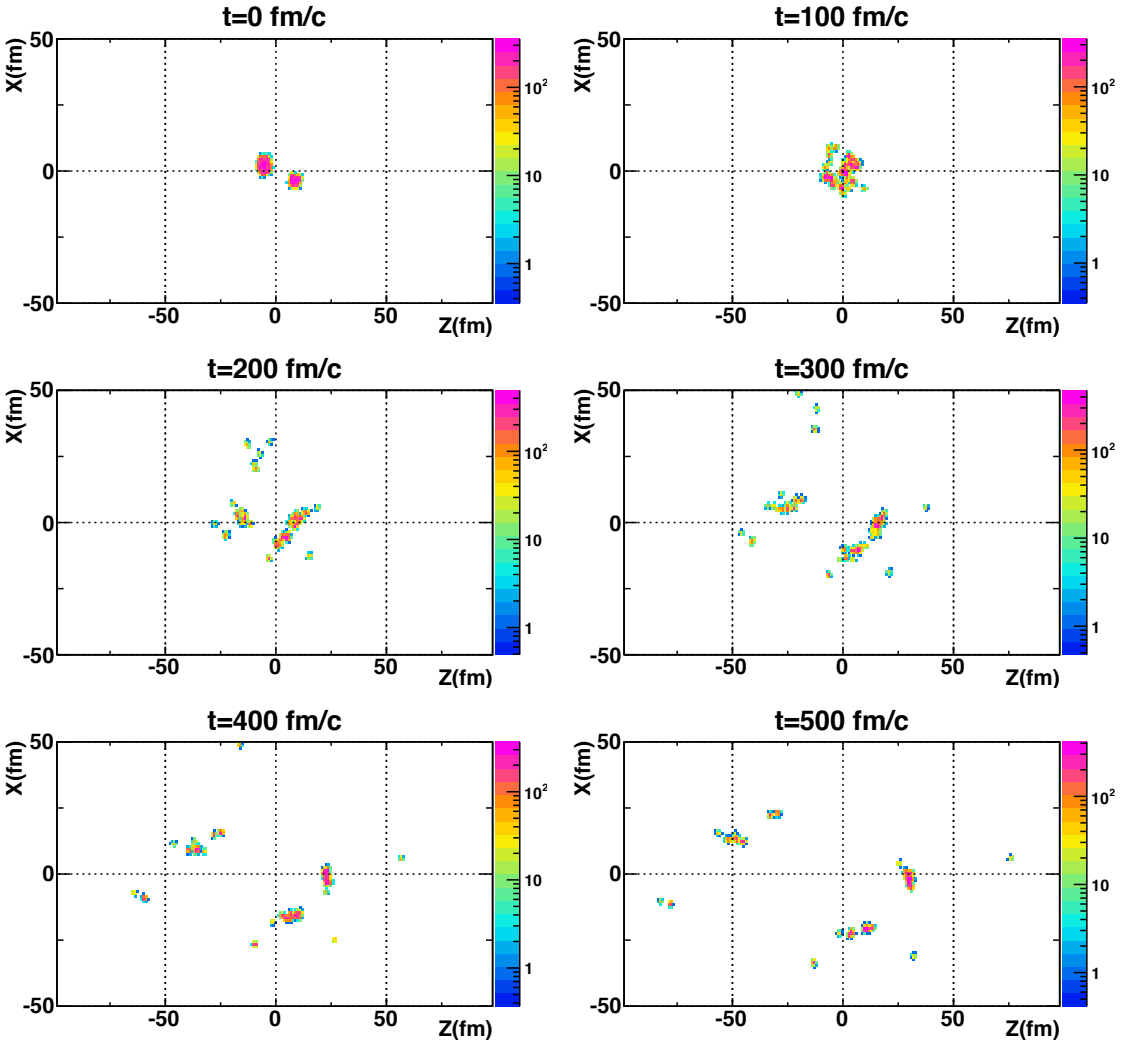


**Figure 5.12:** *Time evolution of a simulated semi-peripheral event (impact parameter $b = 5.6\,fm$) modelled with the AMD code. The six snapshots are as in the previous figure. The shown event corresponds to a kind of multi-fragmentation event. The colour scale corresponds to the density distribution of the nucleons gaussian packets.*

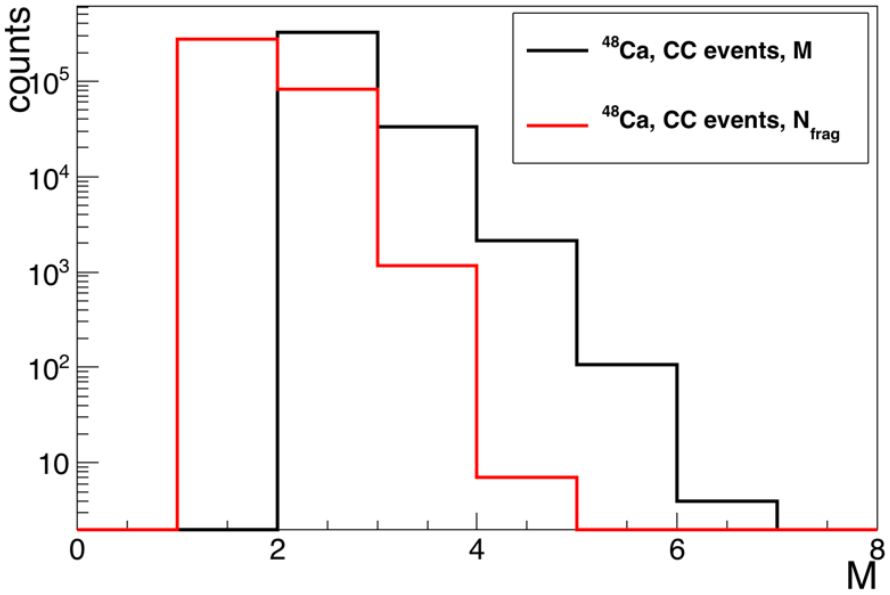


**Figure 5.13:** *In black the multiplicity distribution and in red the fragment multiplicity distribution of events included in CC event set.*

literature [20, 21].

- The primary fragments consist of two or more heavy IMF (Z$\sim 20 \div 25$) emerging from the multi-fragmentation of an excited system. In fig. 5.12 the time evolution of such an event is followed up to 500 fm/c.

In fig. 5.13 the multiplicity $M$ and the fragment multiplicity $N_{frag}$ of the events inside the CC selection has been drawn in black and red respectively for the $^{48}$Ca system. The multiplicity is generally lower with respect to the expected values for a multi-fragmentation [105, 106]. This is not surprising considering the relatively low acceptance of the FAZIA array in this experiment. We remind in this respect the severe shrinking of the multiplicity distribution evidenced by the simulations (fig. 4.8).

Nevertheless, the low event completeness ($\sim 50\%$) of the acquired data prevents a reliable identification and separation of these reaction processes and experimentally we are not able to go into further details for these central events types due, as said, to the insufficient angular coverage of the apparatus.

### 5.3.3 DIC selection

The black rectangle in fig. 5.8 is the gate used to select the DIC events: it corresponds to $18 \leq Z \leq Z_{tot}$ and $9 < \theta_{flow} \leq 30$. In fig. 5.14 the Z vs $V_{lab}$ correlations for experimental (left panel) and simulated (right panel) events for all the particles

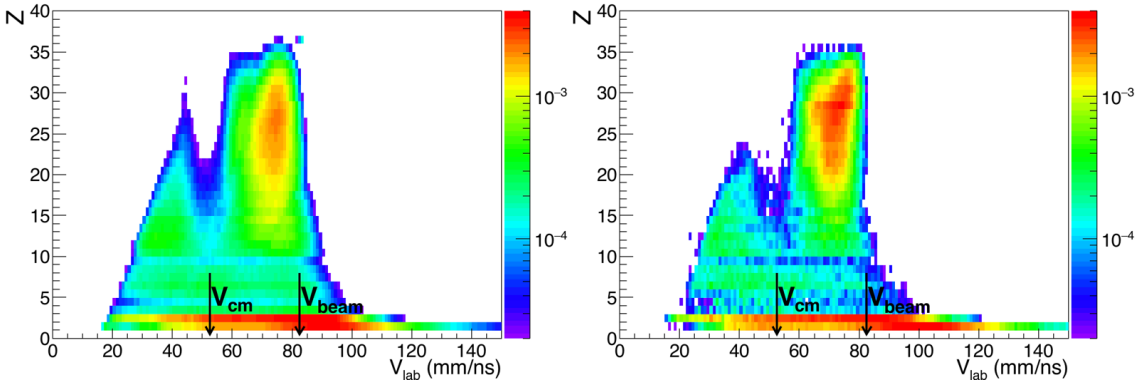


**Figure 5.14:** *Z vs $V_{lab}$ correlation for the DIC selection events; left experimental data, right simulated data. A residual contribution of CC events is still present. The two plots are normalized to their integral.*

satisfying the DIC condition are shown. The correlations feature an intensification around the QP region and a residual background of central events in both the experimental data and the simulation, as expected on the basis of previous considerations (see Sec. 5.3.1). In order to better discriminate the two event types (thus reducing the central events background in the DIC class) the use of other selective observables would be needed (e.g. LCP multiplicity [107] or transverse energy [105, 106]). Due to the reduced angular coverage of the FAZIA apparatus however, we are not able to use one of these global observables. Nevertheless, the difference of the QP velocity with respect to the velocity of fragments coming from a multi-fragmentation type reaction (see fig. 5.14) allows for the discrimination between these two class of events by means of a simple cut on the velocity of the biggest fragment ($V_{CM}^{qp} > 0$).

In order to take into account the events in which just the QP is detected in coincidence with a LCP or a very light IMF ($Z^{ii} = 3, 4$ where $Z^{ii}$ identifies the second biggest fragment detected in the event) which are not included in the fission-like events (see below), we classified as **QP-only** all the events which satisfy the following conditions:

$$\begin{cases} N_{frag} \geq 2 \\ Z^{qp} \geq 18 \\ V_{CM}^{qp} > 0 \\ Z^{ii} = 3 \, or \, 4 \end{cases} \quad \text{or} \quad \begin{cases} N_{frag} = 1 \\ Z^{qp} \geq 18 \\ V_{CM}^{qp} > 0 \end{cases} \tag{5.3}$$

In panel a) of fig. 5.15 the Z vs $V_{lab}$ correlation of the biggest detected fragment ($Z^{qp} \geq 18$) in this class of event for the experimental data (panel d for simulation) is shown. This QP-only events set mainly contains less dissipative DIC events in

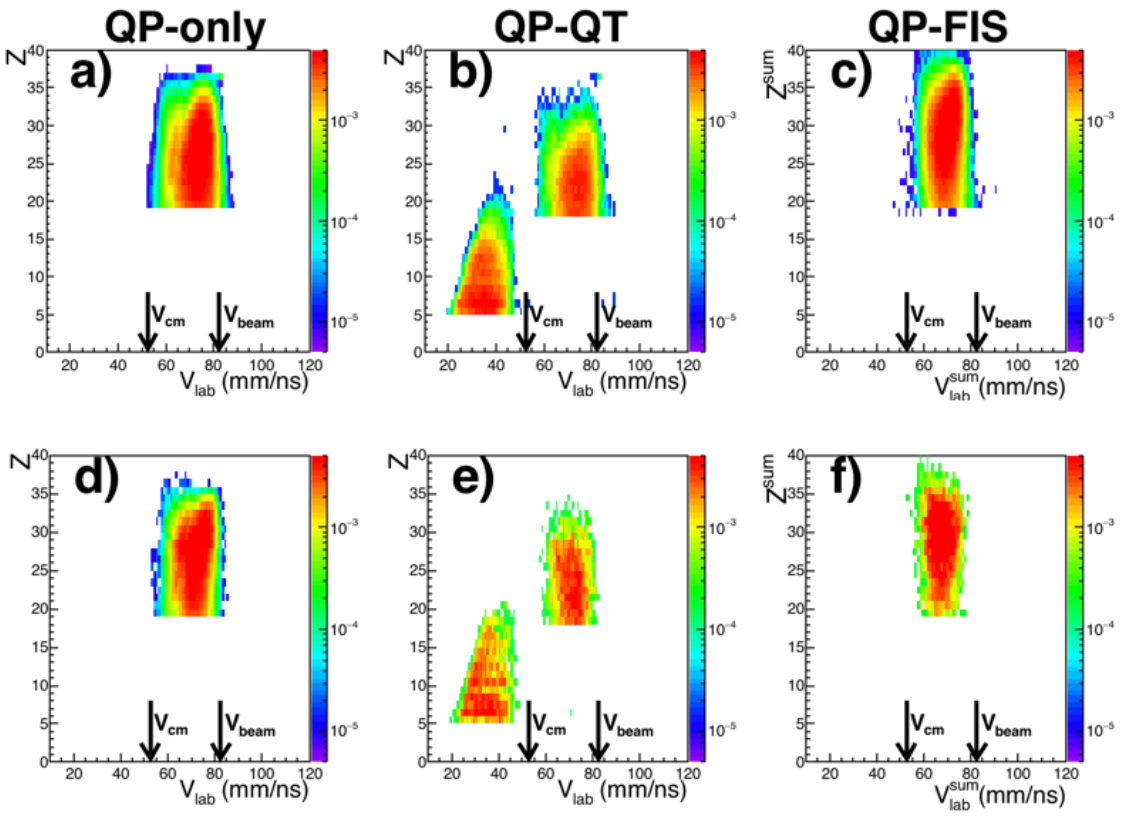


**Figure 5.15:** *Z vs $V_{lab}$ correlation for the different dissipative event subsets. Panels a, b, c (d, e, f) correspond, respectively, to the three selected groups labeled as QP-only, QP-QT and QP-FIS for experimental (simulated) results. See text for details about the different event sets. Each correlation is normalized to its integral.*

which the QT is not detected in coincidence with QP because its phase-space is not included in the experimental acceptance.

The $V_{par}$ vs $V_{perp}$ correlation for the $\alpha$ particles with respect to the QP direction in the CM has been drawn in fig. 5.16 for QP-only selected events. The experimental and simulated data are reported in the left and right panel respectively. The Coulomb ridge for the $\alpha$ emitted by the QP is evident in the picture. The corresponding ridge for QT is strongly affected by the limited efficiency: we can detect only the $\alpha$ particles emitted at forward angles by the QT source. As noticed above, the regions with anomalous intensity are due to the geometrical acceptance and they are nicely reproduced by the filtered simulation. A relevant contribution of particles in the mid-velocity region is also detected as expected for these type of collisions (e.g. refs. [17, 105, 106]).

In order to disentangle CC events from the more abundant DIC events for $\theta_{flow} < 30$, let's consider now the events where at least two fragments $N_{frag} \geq 2$ have been detected with the second $Z^{ii} \geq 5$. We now consider the correlation between the

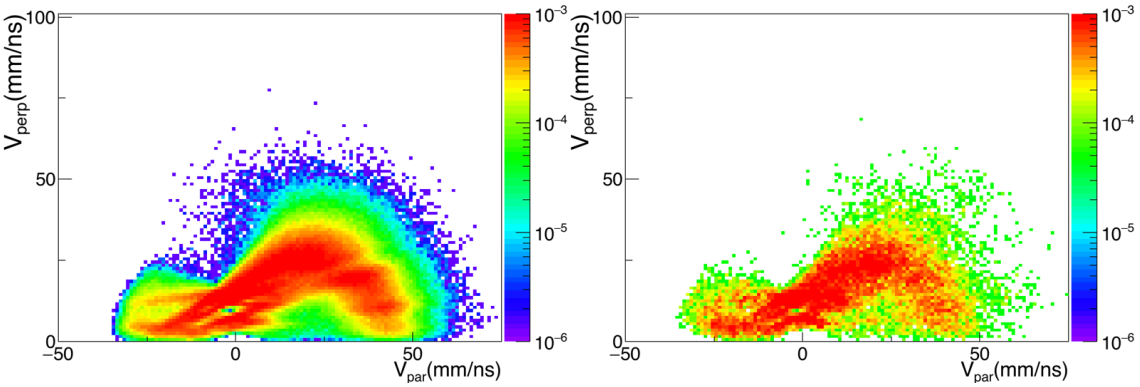


**Figure 5.16:** *QP-only selection: $V_{par}$ vs $V_{perp}$ plot in the CM system for $\alpha$ particles with respect to the QP direction. In the left (right) panel the experimental (simulated) data are shown. The correlations are normalized to their integral.*

relative angle ($\theta^{rel}_{CM}$) in the CM frame and the relative velocity ($V_{rel}$) of the two biggest fragments of the event which is shown in fig. 5.17 (experimental data in the left panel and simulation in the right panel).

Two different regions can be distinguished in the plots:

- red rectangle ($160° < \theta^{rel}_{CM} < 180°$ and $10\,\text{mm/ns} < V_{rel} < 70\,\text{mm/ns}$); in this region the two fragments are produced in opposite directions in the CM frame with a rather broad range of relative velocities having a maximum at about $35 \div 40\,\text{mm/ns}$;
- black rectangle ($40° < \theta^{rel}_{CM} < 100°$ and $10\,\text{mm/ns} < V_{rel} < 45\,\text{mm/ns}$); this gate includes fragments reseparating under the effect of the Coulomb repulsion (this picture is compatible with the systematics of fission events studied by Viola [100]).

The first event set is compatible with deep inelastic collisions in which the QT is emitted in the backward direction and the QP in the forward direction in the CM frame. The Z vs $V_{lab}$ correlation for the two biggest detected fragments in this class of events is shown in panel b) of fig. 5.15 for the experimental data and in panel e) for the simulation. Two different locations associated respectively to the QT and QP fragments clearly show up: this class of DIC events will be called **QP-QT** in the following. The correlation is concentrated at slightly lower velocities and charges with respect to the QP region as it appears in the QP-only correlation shown in panel a), as expected. To further clean up the QP-QT selection two other conditions are imposed: $V^{qp}_{CM} > 0$ (in order to reject events in which only QT and another smaller fragment, maybe coming from the QP evaporative chain, are detected in coincidence) and $Z^{ii} \geq 5$ (to discard events in which the QP is detected in coincidence with a fragment coming from the QP or QT evaporative chain).

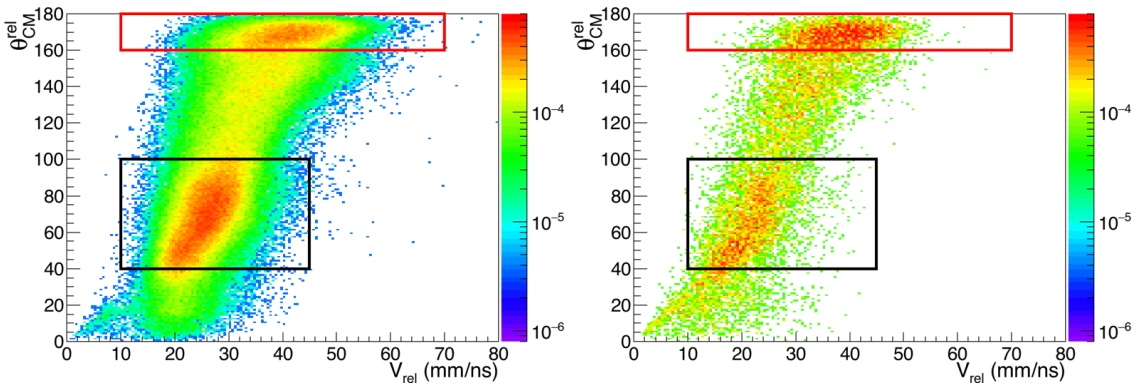


**Figure 5.17:** *Correlation between the relative angle ($\theta^{rel}_{CM}$) in the C.M frame between the two biggest fragments in the event and their relative velocity ($V_{rel}$) for events belonging to the DIC selection. In the left (right) panel the experimental (simulated) correlation is shown. The black rectangle corresponds to events coming from QP fission (QP-FIS), the red one corresponds to events where both QT and QP are detected in coincidence (QP-QT). The two correlations are normalized to their integral.*

The second class of events can be ascribed to the process of quasi-projectile fission. In panel c) (panel f) of fig. 5.15 the experimental (simulated) correlation between the charge $Z^{sum}$ and the laboratory velocity $V^{sum}_{lab}$ of the QP as reconstructed from the two fission fragments quantities is shown. The correlation looks very similar to that corresponding to the QP case (panel a) thus reinforcing the hypothesis of QP fission for this class of events. This sub-class of DIC events will be called **QP-FIS** in the following. To further clean up the QP-FIS selection, we impose also that $Z^{sum} \geq 18$ (this condition corresponds to the fixed lower limit for the QP reconstructed charge) and $V^{sum}_{lab} > 0$ (to reject events in which a QT fission is detected).

The experimental velocity plots for the $\alpha$ particles emitted in the two dissipative collision subsets are shown in fig. 5.18. Due to the low probability of detection of this class of events (see also Sec. 5.3.7 for more details), the acquired statistics is lower with respect to the other event sets. The statistics of the simulated events is "a fortiori" not high enough to get a meaningful correlation. The correlation for the QP-QT events shows clearly the presence of an emitting source centred around the QP velocity together with the forward emission from the QT. Comparing this plot with the same plot for the QP-only class of event (left panel in fig. 5.16), we observe a very similar behaviour but with a clearer definition of the emission from the QT source. This is a further support for the hypothesis that events classified in the QP-QT and QP-only classes are actually of the same type.

Unlike the QP-QT case, for QP fission events the Coulomb circles are not clearly

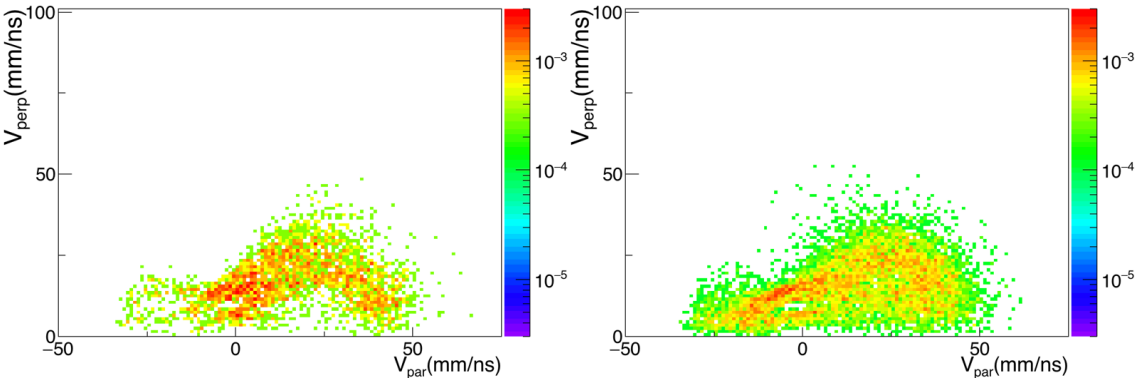


**Figure 5.18:** *Correlation between the parallel ($V_{par}$) and perpendicular ($V_{perp}$) components of the velocity of the $\alpha$ particles with respect to the QP direction in the CM. In the left (right) panel the experimental data for the selection QP-QT (QP-FIS) selection is drawn. The correlations are normalized to their integral.*

defined. In fact, including all the possible configurations without any conditions on the two fission fragments, a great number of different emitting sources contribute to the same correlation, which also includes the $\alpha$ particles evaporated from the fission fragments after the fission. The presence of all these different sources justify the spread of the Coulomb ridge around the QP.

In order to better appreciate and quantify the differences in the three DIC selections shown in panel a, b and c of fig. 5.15, the Z and $V_{lab}$ distributions are presented in fig. 5.19, in blue, red and green for the QP-only, QP-QT and QP-FIS selections respectively. We observe that the $V_{lab}$ distributions for the QP-only and the QP-QT subset peak at about the same value of $74 \pm 1$ mm/ns while the QP-FIS maximum is somewhat lower ($69 \pm 1$ mm/ns). As for the maxima of the Z distributions, we note that they peak at 26.5, 30.7 and 22.6 for QP-only, QP-FIS and QP-QT respectively

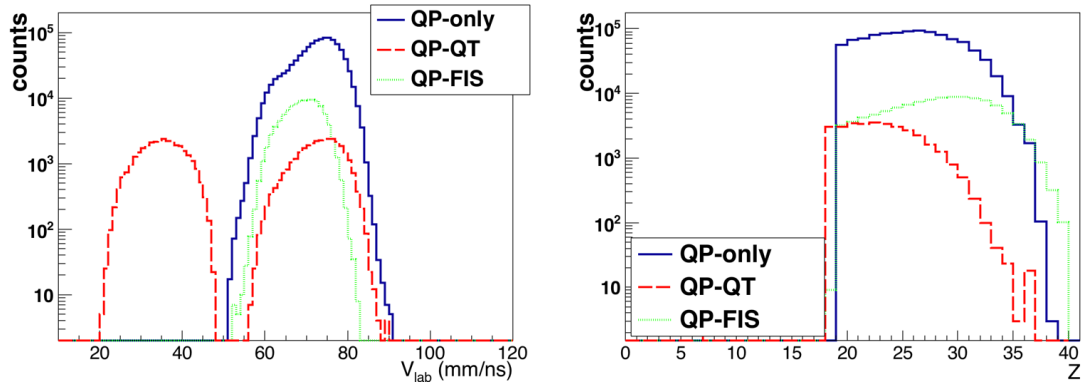


**Figure 5.19:** *Experimental distribution of $V_{lab}$ (left) and Z (right) for the main fragment of the three selected event subsets (see fig. 5.15). The three different colors refer to the three event selections. The distributions are not normalized.*

with an uncertainty of 0.5 unit of charge.

A general observation, therefore, is that the apparatus is sensitive in any case to rather dissipative collisions (peripheral reactions are suppressed). Indeed, the final QP remnants are quite lighter than the projectile: more than ten charge units are missing with respect to the initial charge (Z = 36). In some more detail, when the QP fissions, the summed reconstructed final charge is on average slightly heavier than in the case of the evaporation channel (four unit of charge more). Finally, the QP-QT class of events includes slightly more dissipative collisions than the QP-only class as evidenced by the lower QP charge.

### 5.3.4 Centrality estimation

Because of the limited angular coverage of the FAZIA apparatus, it is not possible to detect complete events and exploiting completeness to follow the evolution of the reaction mechanisms as a function of the event centrality expressed through a suitable global variable. Nevertheless, after observing the good overall capability of the AMD model to reproduce various experimental observables (see figs. 5.8, 5.9, 5.14, 5.17, 5.15), the model itself can be exploited to estimate the impact parameter ranges associated to the different event classes. Events were simulated in a b range from 0 to 12 fm but, though the apparatus (geometric filter) imposes a sharp cut for quasi-elastic events (zero efficiency for b > 11 fm).

In fig. 5.20 the impact parameter distributions corresponding to the different classes of events according to the simulation are reported, with different colors. As already noticed, it appears that our analysis selects in general very dissipative collisions and that the peripheral collisions are suppressed by the geometrical coverage of the experimental apparatus. The impact parameter spans almost the same interval for the different classes. However, the CC class, as expected, slightly favours more central events and the QP-only class extends toward less dissipative collisions, up to above 10 fm. The QP-FIS and QP-QT events show a very similar behaviour with approximately flat b distributions between ∼1 and ∼9 fm.

### 5.3.5 Argon contamination of the main beam

The Superconducting Cyclotron K800 (CS) of LNS[1] was set up to deliver a $^{80}$Kr beam with a charge status q = 22+ ($\frac{q}{A}$ = 0.275) in the Ciclope scattering chamber

[1]In a cyclotron the quantity k is a parameter which is defined as k = $\frac{B^2}{2}R^2_{max}$ where B is the intensity of the magnetic field and $R_{max}$ is the cyclotron maximum radius. The energy per nucleon of the delivered beam depends on the effective charge status q and mass A of the projectile and on the k-parameter according to the formula $\frac{E}{A} = k(\frac{q}{A})^2$. k = 800 is the maximum nominal value possible for the CS at LNS.

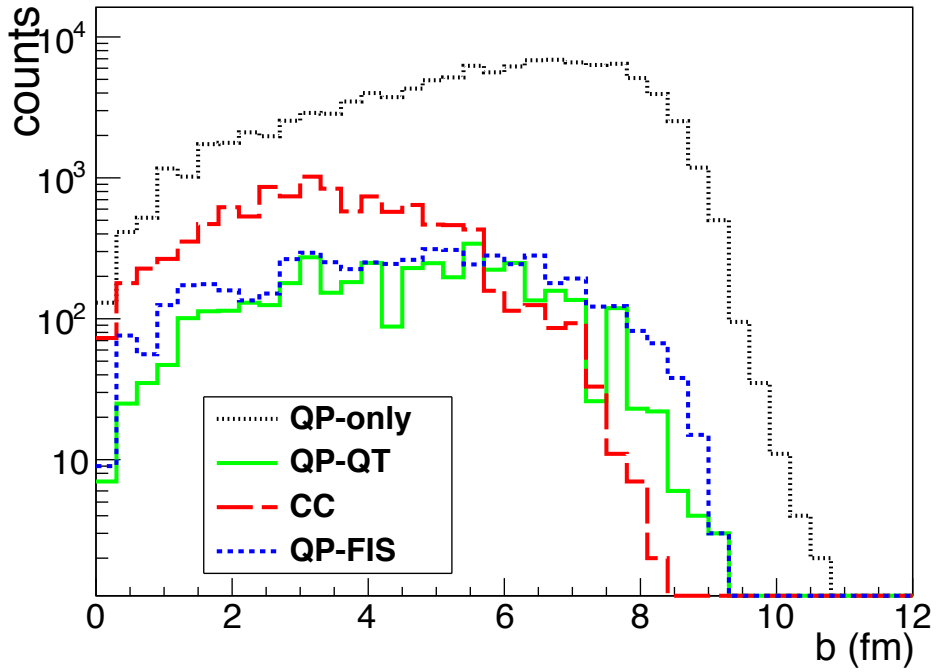


**Figure 5.20:** *Impact parameter (b) distributions for events simulated with the AMD code plus GEMINI++ for $^{80}Kr + ^{48}Ca$. The various event classes are represented by different colors: in black the QP-only, in green the QP-QT, in red the CC and in blue the QP-FIS selection.*

where the FAZIA array was placed. During the last part of the experiment (around the second half of the $^{80}\mathrm{Kr} + ^{40}\mathrm{Ca}$ system) we observed a contamination of the main Kr beam by a spurious Ar beam. While the krypton gas tank contained an enriched $^{80}$Kr gas; the Electron Cyclotron Source (ECR source) used during the ISO-FAZIA experiment unfortunately kept memory of a previous experiment with Ar beam [108]. A $^{40}$Ar isotope with a charge status q = 11+ has the same $\frac{q}{A} = 0.275$ and receives the same acceleration than a $^{80}\mathrm{Kr}^{22+}$, ion thus reaching the same energy per nucleon and consequently the same velocity ($\frac{E}{A} \propto v^2$).

In order to carry the particles from the source to the different experimental chambers, magnetic dipoles and quadrupoles are installed inside the beam-line. The effect of the quadrupoles is to focus in the orthogonal plane with respect to the beam direction; it is mandatory to avoid the broadening of the beam. The dipoles are used to deflect the beam trajectory. Every dipole, characterized by a magnetic field B and a curvature radius R, selects a unique nuclear species with a fixed ratio A/q according to the formula:

$$R = \frac{mv}{qB} \propto \frac{A}{q}$$

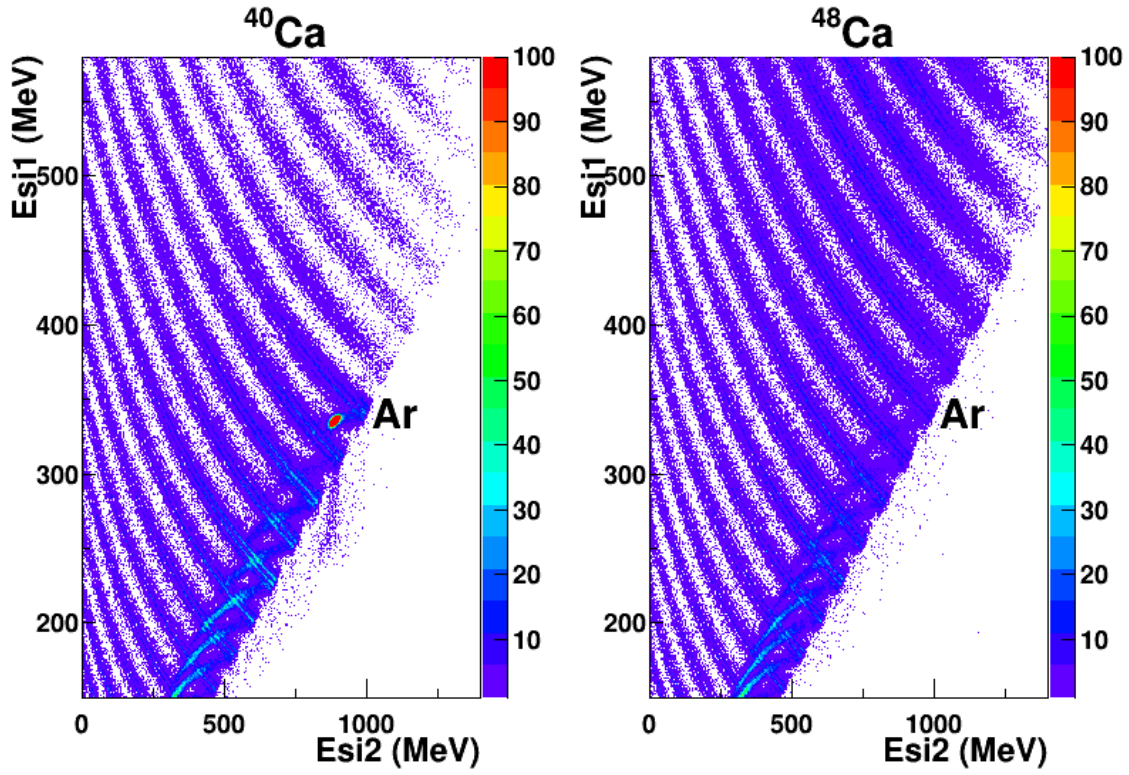


**Figure 5.21:** *ΔE-E (Si1-Si2) correlations for $^{40}Ca$ and $^{48}Ca$ targets on the left and right panel respectively. The plots are expanded around the region of charge distribution between $Z\sim 10$ and $Z\sim 22$. The label indicates the experimental curve corresponding to the argon isotopes. The $^{48}Ca$ correlation is homogeneously populated while in the $^{40}Ca$ system, the argon elastic peak is evident.*

where m and v are the mass and the velocity of the particle respectively. Having the same $\frac{q}{A}$, the same velocity and a negligible mass defect difference, the two isotopes $^{40}Ar^{11+}$ and $^{80}Kr^{22+}$ are undistinguishable by the dipoles and this fact justifies the possibility to observe argon contamination of a krypton beam on the detectors.

As already said in Chapter 2 and 3, ISO-FAZIA was the first experiment of the FAZIA Collaboration dedicated to a physics goal after the R&D phase. A great number of new software tools and new analog features of the FEE cards were tested for the first time on such a big number of detectors (four complete blocks acquired in coincidence). Moreover, also the beam focalisation has been very complicated due to previous problems on the SERSE ion source. For these reasons, at the end of the experiment, it was decided to accept the beam even with its argon contamination, which produced some intensification for $Z \leq 18$ of the Z, A ridges observed in the online control plots.

In fig. 5.21 we show a comparison between the ΔE-E Si1-Si2 correlation obtained for the two systems $^{40}Ca$ and $^{48}Ca$ in left and right panel respectively. In the $^{48}Ca$

| | B2Q4T2 (4.6°) | | B3Q1T1 (11.7°) | |
|---|---|---|---|---|
| $^{40}$Ca | First half | Sec. half | First half | Sec. half |
| total counts | $2.18\times 10^5$ | $7.70\times 10^5$ | $1.65\times 10^5$ | $3.94\times 10^5$ |
| $Z<18$ | $9.84\times 10^4$ | $5.11\times 10^5$ | $1.62\times 10^5$ | $3.91\times 10^5$ |
| $Z>18$ | $1.13\times 10^5$ | $1.89\times 10^5$ | $2.36\times 10^4$ | $3.45\times 10^4$ |

**Table 5.1:** *In the first raw of the table the total counts of the ΔE-E Si1-Si2 correlations (an example is shown in fig. 5.21) are reported for the first and second half of the $^{40}$Ca system without and with argon contamination, respectively. The values are reported for two telescopes at different polar angles. In the second (third) raw the counts below (above) the Ar ridge are reported.*

case there are no hints of contamination. Instead, for the $^{40}$Ca system the argon ridge (pointed out by a label) shows a clear evidence of the elastic scattering due to the spurious argon beam.

To quantify the argon contamination, the populations of ions in the regions below and beyond the argon ridge have been compared exploiting the ΔE-E Si1-Si2 correlations. The same quantity has been evaluated for two different detectors: one close to the beam which detects the argon elastic peak (B2Q4T2 centered at $\theta = 4.6°$), one more backward (B3Q1T1 around $\theta = 11.7°$ and not reached by elastically scattered projectiles). In tab. 5.1 we report the accumulated statistics in the two telescopes, in the first half data set of the $^{40}$Ca reaction, with no evidence of argon contamination ("First Half"), and for the second part of the measurement, with argon contamination ("Sec. Half") for both detectors. For each telescope, normalizing the two data sets of the experiment to the counts with $Z>18$, we can estimate the excess of counts of $Z<18$ by subtraction.

We thus found that for the second half of $^{40}$Ca experiment the $^{40}$Ar contamination was around 40% of the total. Nevertheless, we decided to use all the acquired statistics for the $^{40}$Ca system counting on the strong suppression of the argon contribution obtained by imposing a lower limit on the QP charge to $Z>18$.

### 5.3.6 Carbon background

During the ISO-FAZIA experiment we used two different calcium targets of 500 $\mu$g/cm$^2$ thickness manufactured at Laboratori Nazionali di Legnaro (LNL) of INFN. The stable isotope is $^{40}$Ca with 96.94% of natural abundance while $^{48}$Ca is unstable with a very long half-life of $6.4\times 10^{19}$ y. Calcium is an alkaline earth metal and it is chemically reactive. When it is exposed to the air, it very rapidly forms a gray-white coating of calcium oxide and calcium nitride. In order to prevent the formation of these compounds which degrade the target purity, a great attention is dedicated to

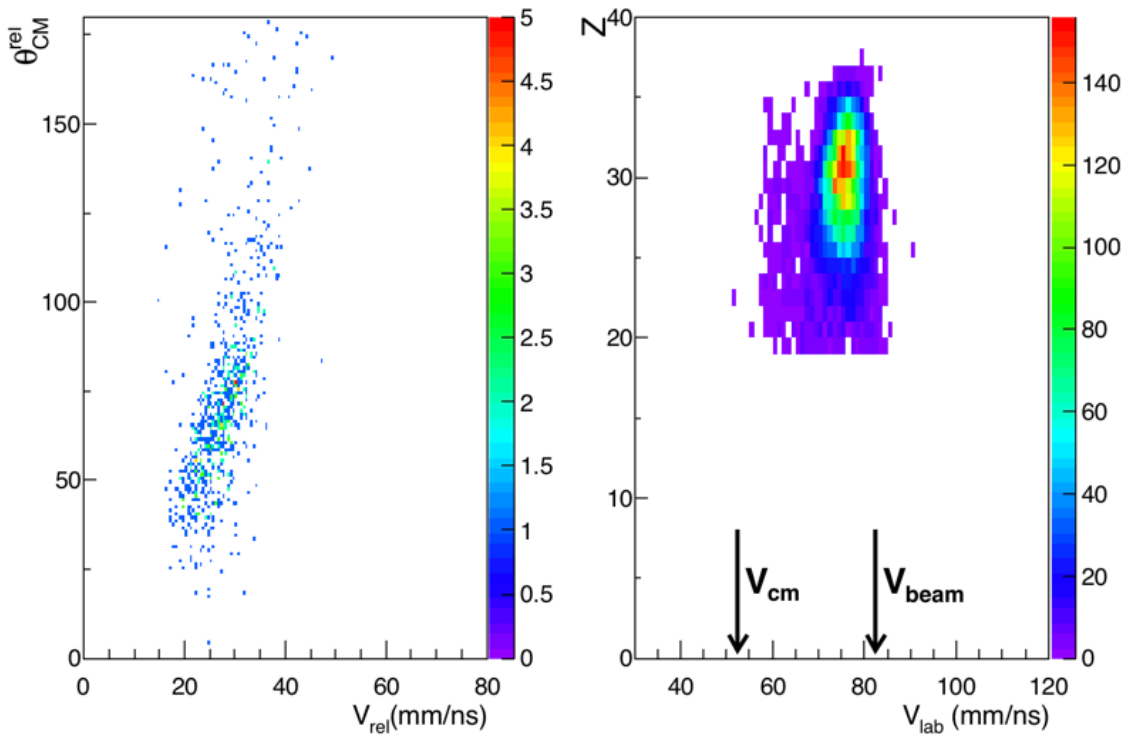


**Figure 5.22:** *Results for the $^{80}Kr + ^{12}C$ reaction. In the left panel the correlation between $\theta^{rel}_{CM}$ and $V_{rel}$ between the two biggest fragments in the events selected as DIC (see sec. 5.3 for the definition) is shown. In the right panel the Z vs $V_{lab}$ correlation obtained for events satisfying the QP-Only selection is shown.*

reduce as much as possible the calcium target exposure to the air. For instance, it is stored in a dedicated box until the definitive mounting in the scattering chamber. Moreover, the calcium foils have been covered with carbon backing ($10\,\mu g/cm^2$) on both sides in order to avoid a direct contact between calcium and air.

The carbon backing preserves the target but it also contaminates its purity. During the experiment a series of measurements using a $^{12}$C target have been performed to study the $^{80}$Kr + $^{12}$C reaction at 35 MeV/u in order to estimate its background contribution to the systems $^{80}$Kr + $^{48,40}$Ca. Unfortunately, the statistics accumulated was not enough to perform a reliable direct subtraction of the carbon contribution from the spectra obtained for the calcium systems.

In the left panel of fig. 5.22 we report the correlation $\theta^{rel}_{CM}$ vs $V_{rel}$ obtained for the two biggest fragments in the events belonging to the DIC selection (see sec. 5.3 for more details) for the system $^{80}$Kr + $^{12}$C, assuming the kinematics of $^{80}$Kr + $^{48}$Ca. Comparing the results with the same correlation in the left panel of fig. 5.17 obtained for $^{48}$Ca target, we deduce that DIC events in which we observe the fission of QP (QP-FIS) are affected by the presence of carbon in the target; on the contrary,

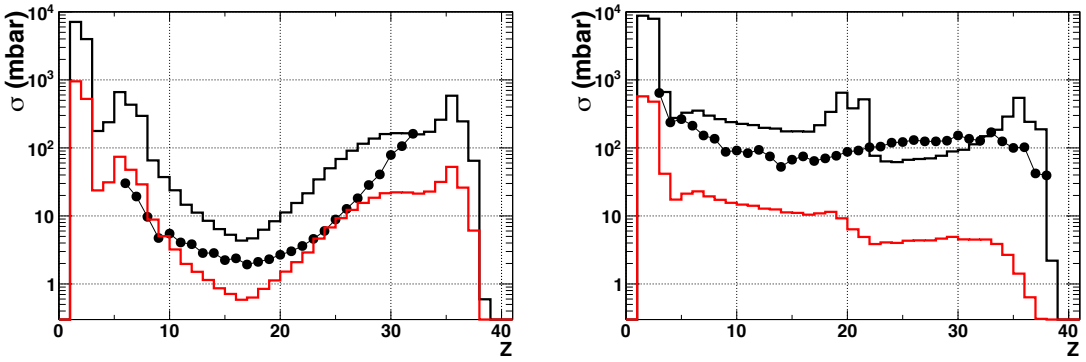


**Figure 5.23:** *Cross section for $^{80}Kr + ^{12}C$ (left panel) and $^{80}Kr + ^{48}Ca$ (right panel) from HIPSE calculations: black curves are simulations run in the range $b = 0 \div 12\,fm$ while red curves refer to the range $b = 0 \div 8\,fm$ ($b = 0 \div 7\,fm$) for calcium (carbon). The black dots are the experimental $\sigma$ reported in [20] for $^{80}Kr + ^{12}C$ and $^{80}Kr + ^{nat}Ti$ respectively.*

binary QP-QT events are poorly contaminated (by detecting also the target, in QP-QT events we can clearly distinguish reactions on carbon from those on calcium).

In the right panel of fig. 5.22, for the data acquired with $^{12}$C as a target, the Z vs $V_{lab}$ correlation for fragments satisfying the QP-only selection is shown. The correlation is similar to that shown in panel a) of fig. 5.15 obtained for $^{48}$Ca target. We conclude that also the QP-only selection is contaminated by the reaction on carbon. Instead, central collision events (CC), show different kinematical properties and are distinguishable in the two systems. We can neglect any carbon contamination in CC selection.

In order to estimate the contribution of carbon contamination we performed a simulation using the HIPSE code (already described in 4.3). Around 6 million events for both $^{80}\mathrm{Kr} + ^{12}\mathrm{C}$ and $^{80}\mathrm{Kr} + ^{48}\mathrm{Ca}$ reactions have been accumulated. To verify the reliability of the HIPSE simulation in reproducing the experimental data at a sufficient level, in the left and right panels of fig. 5.23 the total cross sections obtained from the simulation are reported as black curves for $^{12}$C and $^{48}$Ca respectively. The black full dots in fig. 5.23 are the experimental values of the total cross section measured by Faure-Ramstein [20] on $^{80}\mathrm{Kr} + ^{12}\mathrm{C}$ (left panel) and $^{80}\mathrm{Kr} + ^{nat}\mathrm{Ti}$ (right panel) at 35 MeV/u. Obviously, the $^{nat}$Ti reaction is not exactly the studied reaction on $^{48}$Ca but it is rather close to it (Z = 22 instead of Z = 20) and it has been chosen for the sake of comparison with the HIPSE simulation due to the lack of data on $^{48}$Ca in the literature. The Faure-Ramstein experimental apparatus [20] was not able to detect the peripheral collisions due to its limited geometrical efficiency. To take into account this limitation of the experimental data, in both panels of fig. 5.23 specific HIPSE calculations in limited ranges of impact parameter have been drawn (in red), namely b= 0÷8 fm for the calcium system and b= 0÷7 for the carbon one, to exclude

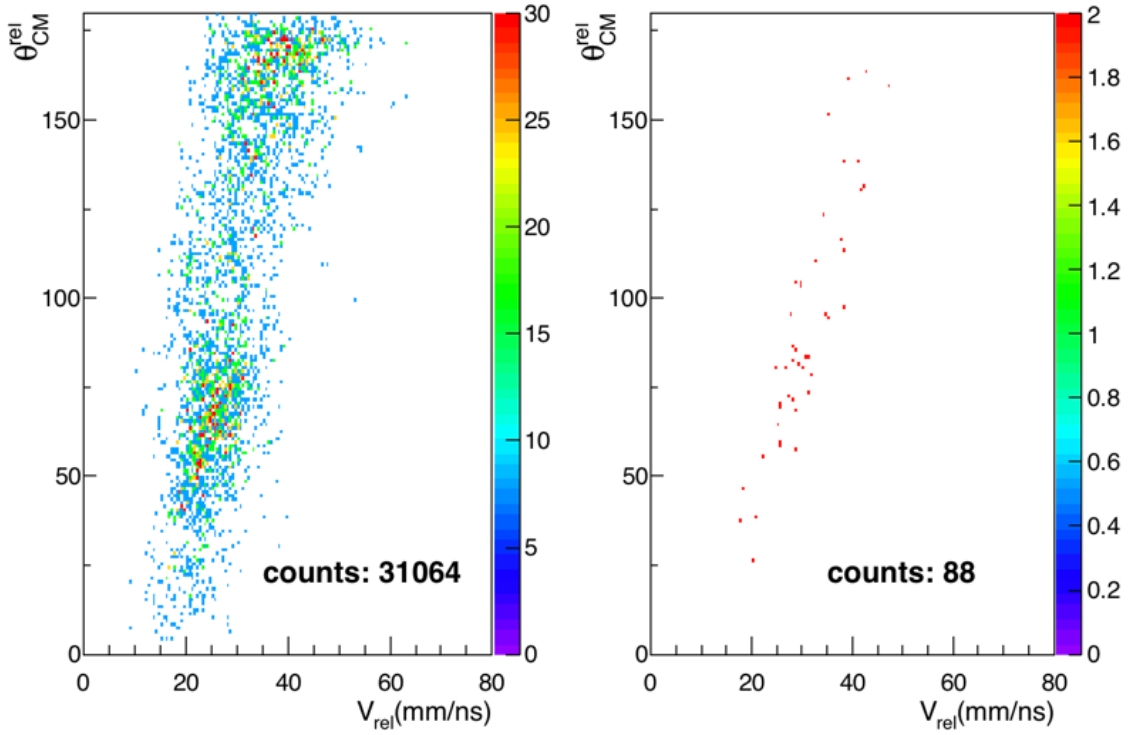


**Figure 5.24:** *Correlations $\theta^{rel}_{CM}$ vs $V_{rel}$ evaluated for the two biggest fragments in the DIC event selections for HIPSE simulation are shown for $^{80}Kr+^{48}Ca$ and $^{80}Kr+^{12}C$ systems in the left and the right panel respectively. In figure the number of counts reported for the two panels, after applying the normalization factors described in text on the $^{12}C$ system.*

peripheral collisions. These values have been chosen as the optimal values to obtain a good agreement between the shape of the HIPSE cross section distribution and the experimental data found by Faure-Ramstein. The HIPSE distributions (without peripheral reactions, red curves) have been normalized to the experimental data with a unique average factor F for each system (2 for $^{12}$C, 8 for $^{48}$Ca).

In fig. 5.24 the experimental correlations $\theta^{rel}_{CM}$ vs $V_{rel}$ constructed with the two biggest fragments in the event satisfying DIC selection for HIPSE simulation of $^{80}\mathrm{Kr}+^{48}\mathrm{Ca}$ system (left panel) and $^{80}\mathrm{Kr}+^{12}\mathrm{C}$ system (right panel) are shown. We remind that $^{80}\mathrm{Kr}+^{12}\mathrm{C}$ has been analysed taking the kinematics of $^{48}$Ca in order to exactly mimic the spurious features introduced by the $^{12}$C collisions. Besides the already described F factor, another scale factor of 20/500 has been applied to the $^{12}$C spectrum to take into account the relative mass abundance of the two isotopes in the target. In the figure the integral evaluated after applying the scaling factors are reported. The contamination of $^{12}$C in QP-FIS events is be estimated to be about 3‰.

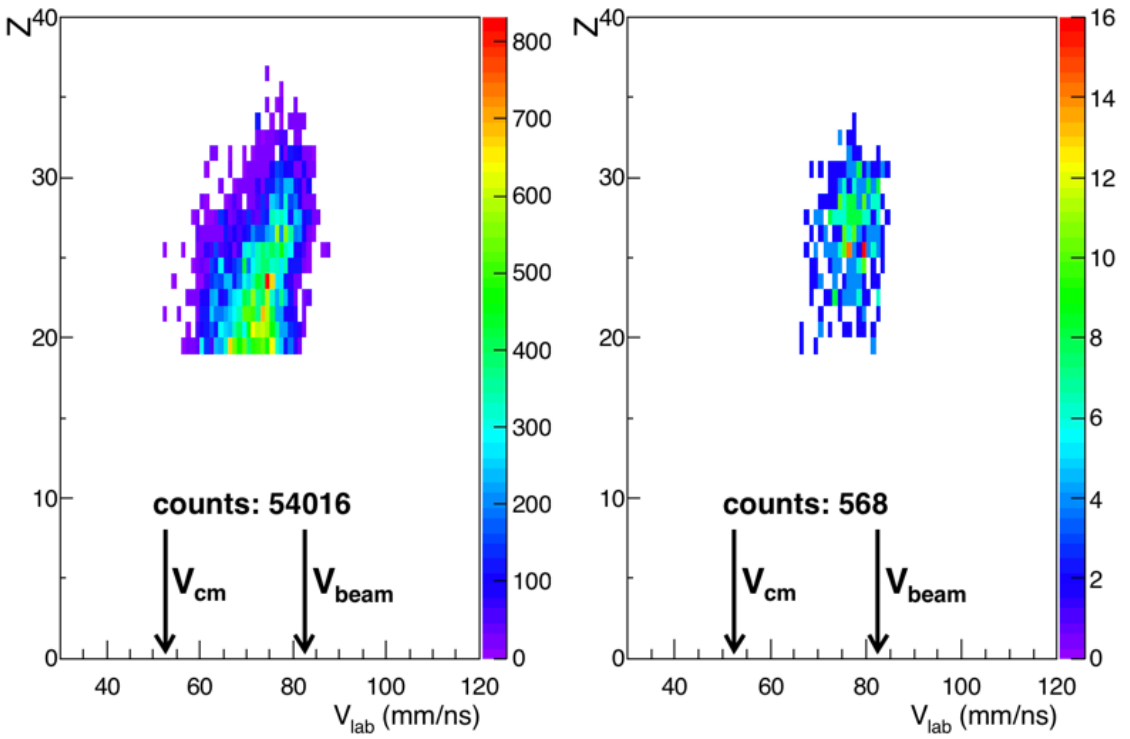


**Figure 5.25:** *The Z vs $V_{lab}$ correlation, evaluated for fragments satisfying the QP-only conditions for HIPSE simulation is shown for $^{80}Kr+^{48}Ca$ and $^{80}Kr+^{12}C$ systems in the left and the right panel respectively. In figure the number of counts reported for the two panels, after applying the normalization factors described in text on the $^{12}C$ system.*

In order to estimate the carbon contamination in the QP-only selection, the same procedure has been performed on the Z vs $V_{lab}$ correlation. In fig. 5.25 the correlations for fragments satisfying the QP-only selection for HIPSE simulation for $^{80}\mathrm{Kr}+^{48}\mathrm{Ca}$ in the left panel and for $^{80}\mathrm{Kr}+^{12}\mathrm{C}$ in the right panel are shown. After applying the proper scaling factors, the relative counts of the correlations suggest a $^{12}\mathrm{C}$ contamination of 1% on the QP-only event selection.

Since it is a phenomenological code, HIPSE is able to reproduce the main characteristics of heavy ion reactions from low (10 MeV/u) to relatively high energies (100 MeV/u), but it is not able to describe the fine details, which require more refined codes, with a stronger theoretical basis, such as AMD. For example, we have verified that HIPSE is able to reasonably reproduce the experimental cross sections for the reactions $^{80}\mathrm{Kr}+^{12}\mathrm{C}$ and $^{80}\mathrm{Kr}+^{nat}\mathrm{Ti}$ at 35 MeV/u except for a normalization factor. Therefore, we used HIPSE just as a means to estimate the overall carbon contamination. We did not use directly AMD to simulate Kr+C because of the very long calculation time necessary to have a reasonable amount of statistics. No

attempt has been made to use HIPSE to subtract the carbon background from the acquired data. Anyway, the obtained HIPSE results suggest that the carbon contamination can be neglected in the following analysis and does not invalidate the conclusion of this work.

### 5.3.7 Relative abundance of the reaction mechanisms

In the ISO-FAZIA experiment, the experimental apparatus does not include a dedicated detector for beam current normalization. Such a detector is usually placed at small polar angles in order to detect elastically scattered beam particles (Rutherford scattering). Data from such a detector, together with the well known Rutherford cross section, are then used in the estimation of the absolute cross section. The lack of this information in ISO-FAZIA prevents the estimation of the absolute cross section of the different reaction mechanisms. We can anyhow study the relative abundance of the different nuclear reaction mechanisms, selected on the basis of the conditions reported in the previous Sections.

The relative percentages of the different reactions mechanisms for the two studied systems have been compared with the model predictions. The results are quoted in tab. 5.2. The percentages are evaluated with respect to the total number of selected events for each system. From tab. 5.2 the following observations can be done:

- on the experimental side, the dominant event class is the QP-only, which represents most of the measured yield. The coincident detection of two nuclei, either from QP fission or from binary collisions, is strongly unfavoured due to the limited acceptance and, in case of fission, to the low production probability. The events compatible with central collisions are anyway a sizeable fraction of the collected data. We thus confirm the known scenario for these heavy-ion

| | Experimental Data | | Model calculation | |
|---|---|---|---|---|
| Target | $^{48}$Ca | $^{40}$Ca | $^{48}$Ca | $^{40}$Ca |
| Total events | $1.4\times10^{6}$ | $2.0\times10^{5}$ | $1.1\times10^{5}$ | $7.4\times10^{4}$ |
| QP-only | 75.6% | 57.4% | 87.4% | 85.1% |
| QP-QT | 2.4% | 2.1% | 3.0% | 2.9% |
| QP-FIS | 8.0% | 7.2% | 4.5% | 4.7% |
| CC | 14.0% | 33.3% | 5.1% | 7.3% |

**Table 5.2:** *Experimental (first and second columns) and simulated (third and fourth columns) percentages of the different reaction mechanisms with respect to the total number of selected events evaluated for each studied system. The ratios are evaluated for all charged particles satisfying the event selection conditions (see text).*

reactions: the largest contribution is from DIC collisions, where the excited QP in some cases undergoes a fission-like split;

- there is a rather large difference between the fractions of the CC and QP-only subsets for the different targets for experimental data. Essentially, $^{40}$Ca gives more CC events than $^{48}$Ca and this excess reflects in a reduced yield for the QP-only subset. Although we have no definitive explanation, we cab think about two reasons; first, due to the lower grazing angle for $^{40}$Ca reaction many QPs could enter, undetected, the forward angle hole around the beam axis; second, a larger tendency of the n-poor Kr+$^{40}$Ca system to produce charged fragments, even for central collisions;

- as for the model, it fairly well reproduces the branching ratios of the event sets thus confirming the good overall quality of the AMD plus GEMINI simulations. However, the model tends to underestimate the CC and the QP-FIS events (by more than a factor two).

# Chapter 6

# Data analysis: Isospin transport and reaction mechanisms

As already mentioned in Sec. 1.2.2, one of the most common techniques used to highlight the isospin transport phenomena occurring during the dynamical phase of the reaction is the comparison between two colliding systems featuring the same projectile nucleus and different isotopes of the same element as a target. This approach allows to indirectly investigate the symmetry energy term of the nuclear EOS, in particular for nuclear matter far from normal conditions.

Although some of the following arguments have been already introduced elsewhere in this work, we believe it useful for the reader to get back to the subject in detail just before discussing the experimental results.

One of the main goals of the ISO-FAZIA is the study of the isospin dynamics, in an attempt at extending further the existing rich literature (including also a previous work of the FAZIA collaboration [40]); moreover, another intended goal is to include in the analysis, for the first time, also events where a QP breaks apart into two main fragments (QP fission-like). In the ISO-FAZIA experiment, a $^{80}$Kr beam and two Ca targets, $^{40}$Ca and $^{48}$Ca, were used. As a consequence, a difference in the <N>/Z of the QP is expected when the two reactions are compared, because of the isospin diffusion. This is the most general expectation one has on the first moment of the mass distributions. Moreover, by looking at the midvelocity region, one should detect fragments that are more neutron rich than the corresponding ions emitted with projectile-like velocity. This is a well assessed expectation, demonstrated by lots of previous results at Fermi energies [40, 99, 109, 110]. In semiperipheral reactions, the dynamics produces fluctuations of the mean-field which produce pieces of nuclear matter ("neck") in between two main partners; these latter, at energies lower than Fermi energies, are the typical QP and QT of DIC collisions. Also, the midvelocity fragment production has features similar but not equal to those of the fission of one of

the two main nuclei. The similarity with low-energy fission gradually grows with the size of the neck; the process becomes slower, the angular distribution becomes less peaked (not anymore aligned or less aligned) and a pair of fragments is found which more closely resembles the two fission fragments from a bigger parent nucleus. In our case, specifically, we expect events compatible with a deformed strongly aligned QT-IMF-QP system, where the IMFs have peculiarities typical of midvelocity emissions. Moreover, we could also expect events where a pair of fission fragments from either the QP or the QT are more easily recognized. For experimental reasons we will concentrate only on the QP fission cases. We note that these events are in any case produced with low statistics because they are related to the fission of a medium-mass nucleus (a Kr-like excited system) which is unfavoured on a statistical ground, being overwhelmed by the evaporation of neutrons and particles.

In the ISO-FAZIA experiment, we therefore expect an evolution of the characteristics of the fragments when moving from the QP to the QT region. Schematically, in the QP sector the emissions (i.e. LCP and IMF or even the fission fragments) should mantain features related to the initial Kr-like nuclei. For the midvelocity system, instead, one should observe a strong focusing and a relative neutron richness with respect to the QP-emitted species for both target cases, but with an additional excess of neutrons in the case of the $^{48}$Ca target. Finally, moving to the QT phase-space zone, particles and fragments could present differences related to their origin from a neutron deficient (N=Z) or from a neutron rich calcium nucleus.

This simplified scheme is indeed quite more complicated in the reality because of the action of various microscopic mechanisms: the exchange of independent nucleons in the mean-field during the contact phase, assumed valid at lower bombarding energies, is not the unique process; because of the fast time scale of the reaction at 35 MeV/u, nucleon-nucleon collisions are for sure contributing to the process.

On top of the already complex dynamics, through which the interaction proceeds leading the system towards some equilibrium (if collision time allows), there is the contribution of fast emissions of particles and even fragments. At Fermi energy this sizeable contribution of fast particle emissions during the collision cannot be neglected. Clearly, this emissions modify, for each step of the collision, the chemistry and the energy balance of the interacting system thus making the description of the whole phenomenology very complex.

It is thus evident the need of sophisticated models which include details of both the dynamics and the statistical decay from the various excited sources. It is also clear that the resulting behaviour of the isospin observables as a function of some ordering parameter of the source phase-space (QP, QT, midvelocity) is far from trivial. To perform this kind of studies the optimal class of events is the QP-QT in which both QP and QT are detected, possibly with other LCP or IMF coming from

the neck. However, the low statistics accumulated for this class of events requires that also the QP-only selection, in which the QT has not been detected, is used for the analysis. When possible, the two event sets are kept distinguished in the following.

## 6.1 Experimental observables and limitations

Among the isospin observables, we will consider henceforth the already defined <N>/Z and $\sigma_A$ (see Sec. 4.1.4). They are related to the first and second moments of the mass distribution of a given element, as detected by the FAZIA telescopes. Although the mass distributions are measured long after the decay from the excited primary species, some information on the isospin dynamics during the collision survives. This last affirmation is supported by model calculations as it will be shown later on.

We observe that we can discuss isospin variables pertaining to the remnants of the original sources (QP and QT) or just to the emitted species (LCP and IMF). In our experiment, the observation is limited, apart from the geometrical acceptance, by the thresholds associated to the identification techniques. The isotopic identification of QP remnants is available up to about $Z = 23 - 25$, while the charge domain is completely accessible. Further the measured mass distributions are for fragments and charged particles mainly coming from the decay of primary species. Therefore, as such, the measured distributions are affected by the previous decay steps of the various sources and they do not directly represents the primary distributions.

In principle, one should study the isospin (and other) variables after disentangling the various sources, namely the QP, the QT and the midvelocity source and, in the case of QP fissions, the fission fragments themselves. Unfortunately, the phase-space separation of the various sources and their emission can be only partial. The most contaminated emissions are those of $Z = 1, 2$ particles, being their emission momenta quite large with respect to the velocity separation between the two major sources (QP, QT). The origin of IMFs, in general, can be better identified but not on an event by event basis. The separation of the sources is a big task for the data analysis as it was discussed in Chapter 5. However, one should be conscious of the limitations of the schematic separation of the event classes and of the emitting sources. In particular, the conditions used to define the event classes (QP-only, QP-QT, QP-FIS) are in part arbitrary and also influenced by the uncomplete detection of the events, due to the limited acceptance. For instance, the detection of a fragment (Z=3, 4, 5) in the midvelocity region can be seen as a tail of the QP fission process towards strongly asymmetric splits. Thus, the separation of the QP-FIS set and the

QP-only with one light fragment in the direction of the QT is somewhat questionable. On the other hand, we know that most QP-only events should be quite similar to QP-QT events because the two sets represent the binary dissipative collisions; only in a fraction of the cases the two main fragments QP-QT have been detected. Even rarer are the cases, that exist, of triple coincidences QP-QT-IMF, which could be labeled as QP fissions (or a QT fissions), fully detected. As a consequence of these considerations, in the following we will discuss the results with continuous cross references among the discussed contexts.

## 6.2 Neutron abundance of QP remnants

The isospin value of the beam projectiles is $I = 1.22$ ($^{80}$Kr). This value is almost halfway between the isospin of the two Ca targets, $I = 1.0$ and $I = 1.4$ for $^{40}$Ca and $^{48}$Ca respectively. Our data can't follow the evolution of the isospin exchange between the QP and the QT from peripheral to central collisions. Indeed, the ISO-FAZIA apparatus detects mainly rather central collisions, missing the most peripheral ones. Moreover, the accessible isotopic distributions are limited to $Z \sim 25$, thus for QP remnants quite lighter than the projectile value $Z = 36$; this means that very dissipative collisions are selected when studying the isospin variables for QP itself. With these remarks in mind, we show in fig. 6.1 the <N>/Z of the QP as a function of the QP-charge, for both systems. For the sake of comparison, the results obtained for QP-only and QP-QT event sets are reported separately. The x-axis range is limited between $Z = 18$ and $Z = 25$. The former is an arbitrary limit for a QP remnant (assumed to get rid of the Ar contamination of $^{40}$Ca, see Sec. 5.3.5); it corresponds to half the charge of the Kr. The value $Z = 25$ instead is the upper limit for the isotopic identification of the FAZIA telescopes (see Sec. 3.4). In the figure the reference <N>/Z values are also reported: they are the equilibrium values 1.29 and 1.14 for the two reactions Kr+$^{48}$Ca,$^{40}$Ca and 1.22 for the Kr projectile. The first observation is that the curves are below the references in all cases; both are lower than the input value for $^{80}$Kr and, in particular, the results for the $^{48}$Ca target are much lower (1.14 vs.1.29) than the average system value. The difference is much less (1.13 vs. 1.14) for the reaction on $^{40}$Ca. This is due to the combined action of the dynamics (part of the nuclear matter is fastly emitted from the system and it can be more neutron rich in the case of the neutron rich system) and of the evaporation from the eventually formed hot source. Within the statistical model, it is well known that hot neutron rich nuclei tend to approach a region in the N-Z nuclide chart (EAL, see Sec. 1.1.2) which is close to the $\beta$-stability line. Of course, this decay path is shorter (and thus the <N>/Z differences are less) for nuclei which

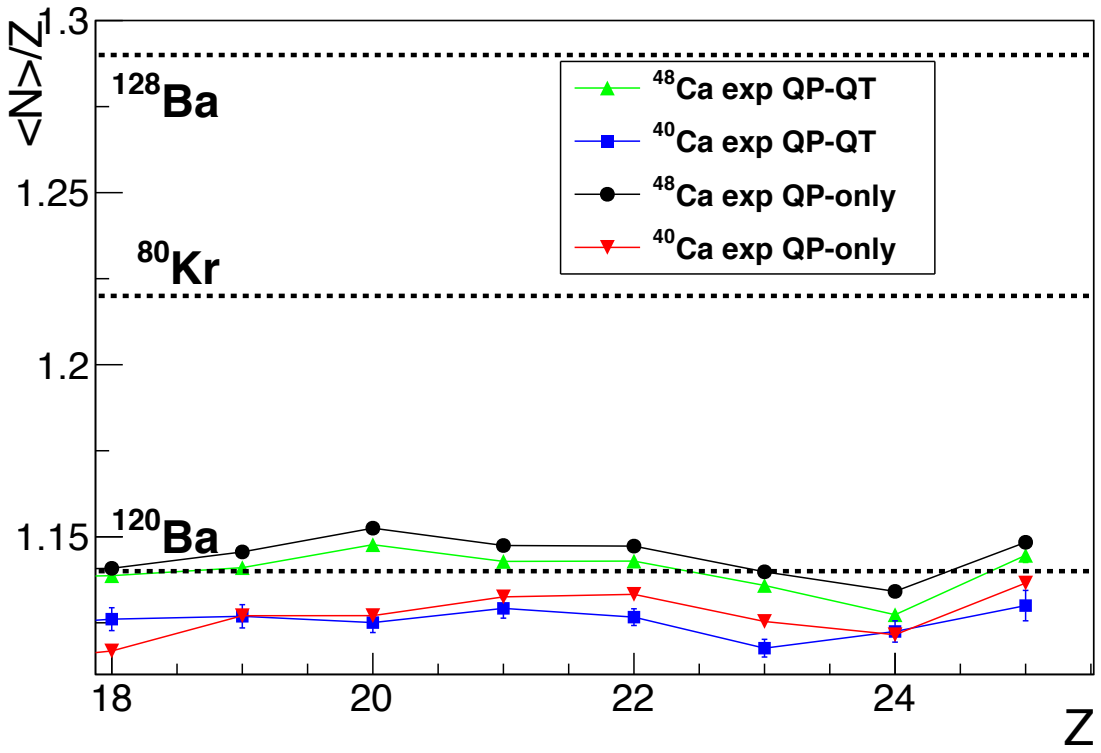


**Figure 6.1:** *The experimental <N>/Z of the QP as a function of the QP charge for the system $^{48}Ca$ ($^{40}Ca$) for different event sets: QP-QT with green upwards triangles (blue squares) and QP-only with black circles (red downwards triangles). The dashed lines corresponds to the equilibrium values for the two reactions $^{80}Kr$+$^{40,48}Ca$ and for the $^{80}Kr$ projectile.*

are closer to the EAL. The different (average) evaporation could be responsible for the small difference observed for the two classes, QP-only and QP-QT, reported in fig. 6.1, with the former showing slightly larger neutron abundances. This can be due to the fact that the QP-QT class selects more central collisions where the energy deposition in the system is larger. The consequent evaporation is larger and the isotopes, on average, get closer to the final destination on the EAL.

Although quite reduced with respect to the projectile, the <N>/Z of the QP produced using the target ($^{48}$Ca) is still higher than for the neutron-deficient one ($^{40}$Ca). This is a clear hint that an isospin diffusion occured. In case of no diffusion, the isospin of the QP should be the same for both targets and the two curves should overlap. This observation is in good agreement with previous studies [8, 40, 111]. The gap between the two curves corresponds to an average neutron difference of 0.4 neutrons.

The comparison with model predictions is shown in fig. 6.2 where the experimental <N>/Z of the QP (for the QP-only class) are drawn together with the

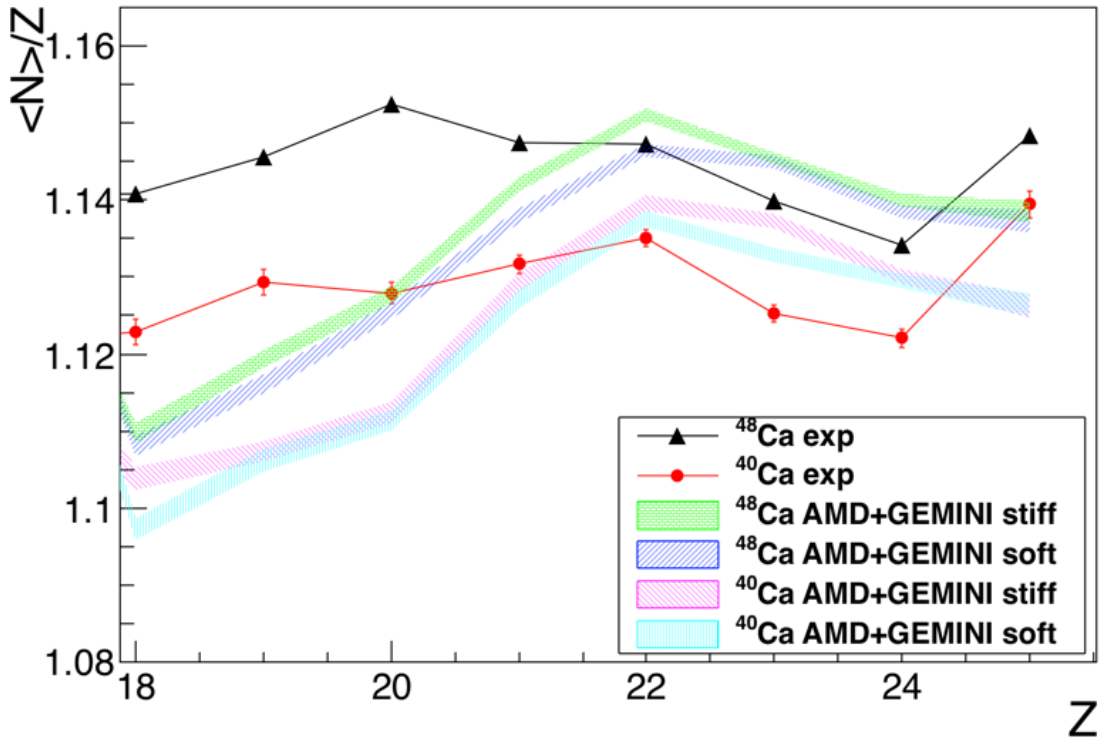


**Figure 6.2:** *The experimental <N>/Z of the QP for the QP-only event set has been plotted as a function of the QP charge (in black and red for $^{48}Ca$ and $^{40}Ca$ systems respectively). The model predictions for the two tested parametrizations (asy-stiff and asy-soft) have also been reported for both systems with different colours and shaded styles as described in the legend.*

same quantities evaluated for the model, using two recipes (asy-stiff and asy-soft, see Chapter 4) for the stiffness of the $E_{sym}$. The Y-axis range has been expanded with respect to the previous figure to evidence the details. In the figure the model predictions have been represented as shaded bands whose widths are the statistical errors. The sensitivity to the stiffness of $E_{sym}$ results to be very weak for this observable. The model correctly predicts the drop of the N/Z values observed in the data with respect to the "reference" values: from this point of view the combined effect of the dynamics and (even more important) of evaporation is well taken into account. The simulation gives reasonable <N>/Z values for Z $\geq$ 21 while it fails for lower Z.

## 6.3 General aspects of the isospin of IMFs

The study of the neutron content of the fragments and in particular of the abundant midvelocity emissions is quite interesting. Within transport models, indeed, the

midvelocity region is supposed to reach, during collisions, sub-saturation density values, thus favouring the process of isospin-drift (see Sec. 1.2.2), i.e. the production of more neutron rich fragments [104, 109, 110, 112, 113]. The level of neutron richness depends on the shape of the $E_{sym}$ as a function of $\rho$. The AMD model is based on a microscopical description of the nuclei and also includes some $E_{sym}$ parametrizations (see Sec. 4.1). Hence it should present some sensitivity for this variable. We thus study the isospin of the light fragments detected in coincidence with the QP; initially we show results of IMF integrating over their emission angle (i.e. without any specific request on the emission direction of the IMF). Then, we will attempt a better identification of their origin, exploiting both their belonging to the various event classes and additional arguments on the emission pattern. In this way we can offer an overview of the present data and compare them with previous systematics.

In fig. 6.3 the experimental <N>/Z values for IMFs starting from lithium are presented, for the two employed targets. The new data are presented together with previous published results at Fermi energies [40, 111]. The present data are shown

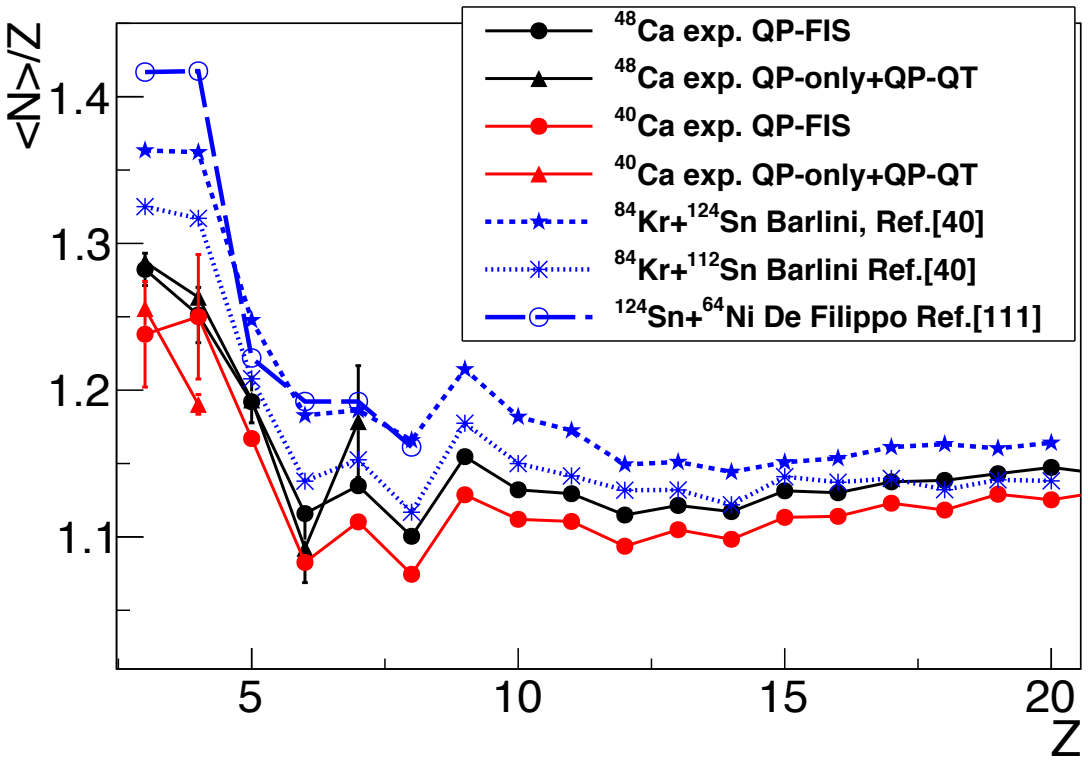


**Figure 6.3:** *Experimental <N>/Z of the IMFs as a function of their charge Z for the two Ca targets: in black for $^{48}$Ca and in red for $^{40}$Ca; triangles are for QP-only+QP-QT; circles are for QP-FIS events. Other experimental results taken from the literature are reported in the figure.*

separately for the IMF of the set "QP-only + QP-QT" and for the set "QP-FIS" (bins containing less than 10 counts have been excluded). The $Z = 1, 2$ particles have not been included in the plot due to their strong evaporative component. At a first glance, the present data behave similarly to the already published results. The data reflect a general property of light IMFs: the measured mass distributions are rather independent of the source and of the details of the production mechanisms. This behaviour is related to the general fact that evaporation dilutes the initial neutron richness and that primary light ions don't possess too many isotopes. However, differences can be observed when looking closer. The ISO-FAZIA data associated to the less neutron rich and lightest system, lie below the other points. The most neutron rich and heavy combination ($^{124}$Sn + $^{64}$Ni) gives the highest values in the plot (though it stops at $Z = 8$ due to the identification limits of the used apparatus). We also observe that, for the present results, the Z range of IMFs belonging to the two event sets is different. In the "QP-only + QP-QT" set we are looking at the small companion of the two main partners (the QP and the QT). Within the "QP-FIS" set we expect to observe a fragment which sometimes is again the smallest one in the event and sometimes it is just the smallest partner of the QP fission (and thus not very small). We will again consider the fragment isospin balance in the QP fission scenario later on; for now we restrict to the case "QP-only + QP-QT" and we compare the data for the lightest fragments with the model predictions.

In fig. 6.4 the experimental value of <N>/Z of the IMFs for the two targets $^{48}$Ca and $^{40}$Ca (left and right panel respectively), has been reported as a function of their charge, from $Z = 3$ to $Z = 7$. Unfortunately, due to the limited acceptance of the apparatus and to the sharp drop of the yields with fragment size, the collected statistics is not large; this is even more true for the $^{40}$Ca target: only lithium and beryllium have sufficient statistics to be analyzed. We observe that fragments with $Z = 5, 6, 7$ (for $^{48}$Ca target) belong to the QP-QT subclass which contains the most complete events: QP-IMF-QT. The simulated data are reported on the same plots as green and blue points for the asy-stiff and asy-soft parametrizations respectively. The low statistics for the simulated data, due to the very long time needed to generate a single event, limits the comparison to the lightest fragments. Within this limitation, we observe that the asy-stiff prescription is in better agreement with the experimental data. The isospin study can also be extended to the second moment of the isotopic distributions (as suggested in Sec. 4.1.4). The $\sigma_A$ observable is supposed to be more sensitive to the $E_{sym}$ behaviour, as implemented in the AMD code, than the <N>/Z of the fragments. In fig. 6.5 the $\sigma_A$ of the mass distributions has been plotted as a function of the charge Z for the same IMFs as in fig. 6.4.

The larger width of beryllium, quite well reproduced by the simulation, is due to the lack of detected $^{8}$Be ions which decay in two $\alpha$s. This obviously increases

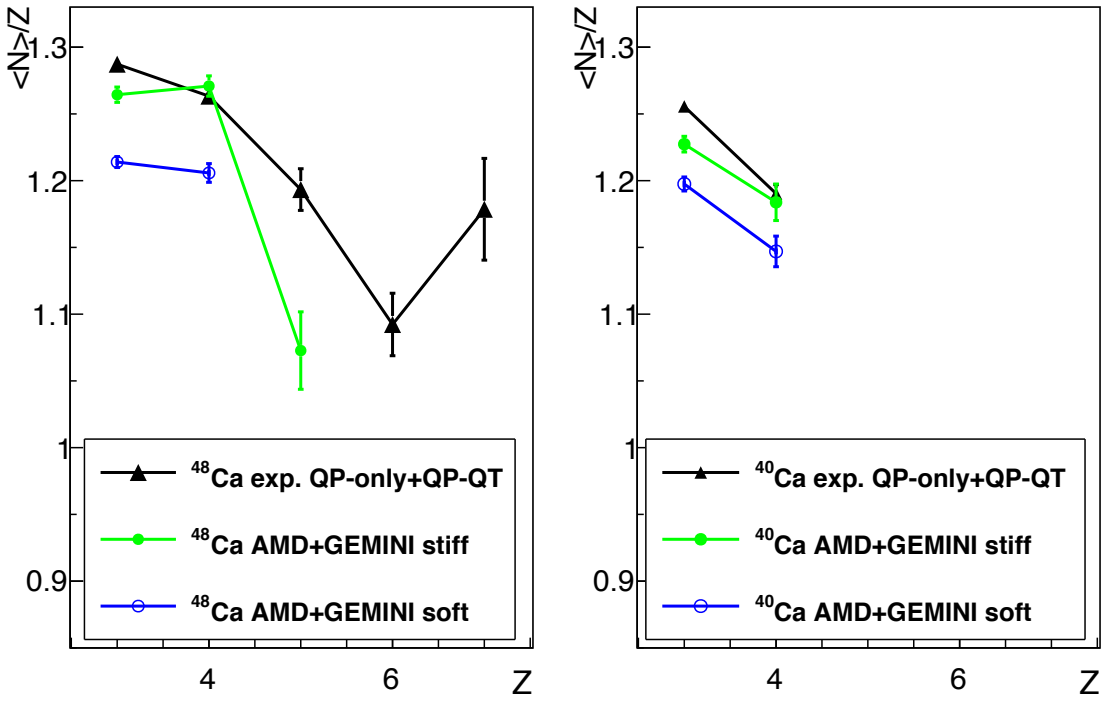


**Figure 6.4:** *$<N>/Z$ vs. $Z$ for the lightest IMFs detected in QP-only and QP-QT event classes. On the left (right) panel the data for the $^{48}Ca$ ($^{40}Ca$) target are drawn. Model results are also reported: green (blue) lines correspond to the asy-stiff (asy-soft) parametrization of the symmetry energy term.*

the mass width with respect to adjacent fragments. The comparison with AMD plus GEMINI++, though restricted to just two elements, supports the asy-stiff parametrization (green shaded region). As for the first moments, we can thus conclude that there is a hint for a stiff behaviour of $E_{sym}$ vs. $\rho$.

## 6.4 Isospin in Central collision events

Before investigating the neutron abundance of fragments produced in binary collisions, we show briefly some results about the IMFs emitted in central events which, much probably, come from a distinct kind of reaction mechanism, typical of most violent collisions. Indeed CC events could reflect the decay of a (unique) transient hot source (possibly expanding and multifragmenting) formed after an incomplete fusion reaction mechanism. The probability of this mechanism at our energies is relatively high (e.g. $200 - 400$ mbarn are reported by [114]). A satisfying investigation of CC events is not affordable in ISO-FAZIA data. Indeed, as already said in Sec. 5.3.2, the limited angular coverage of the FAZIA apparatus prevents a charac-

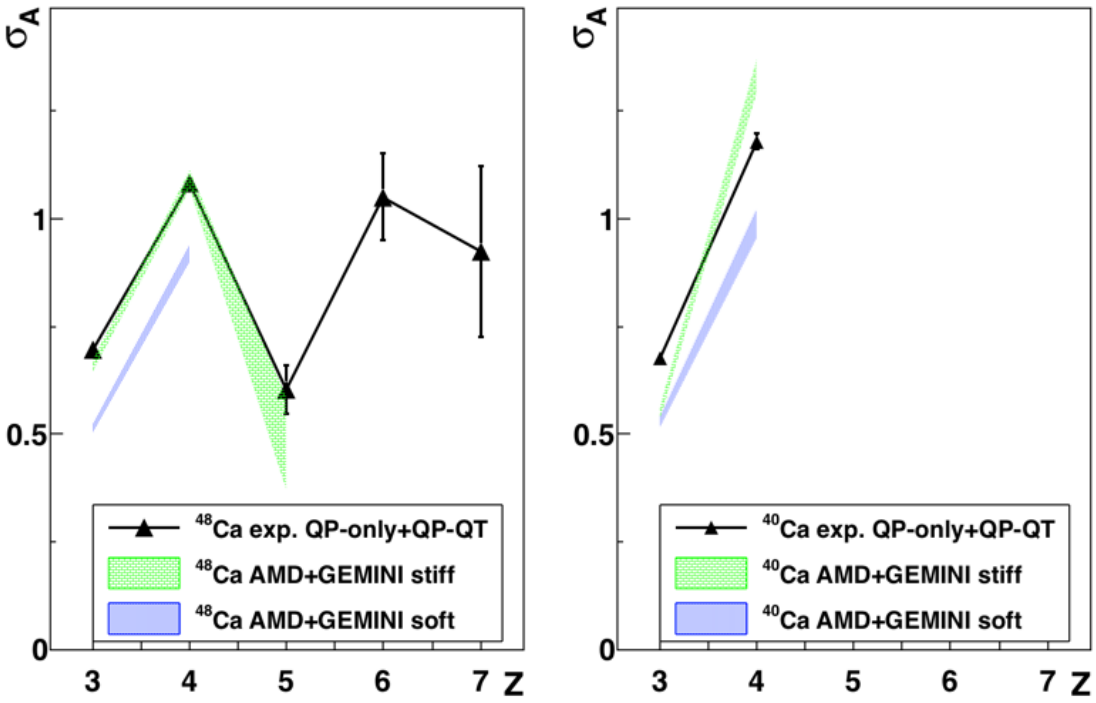


**Figure 6.5:** *Width ($\sigma_A$) of the isotopic distributions as a function of the charge Z for reactions on $^{48}Ca$ (left panel) and on $^{40}Ca$ (right panel). The model predictions are reported as shaded green (asy-stiff) and blue (asy-soft) regions. Only points for which one has at least 10 counts have been plotted.*

terization of these central explosive collisions, featuring fragments emitted in a wide angular range from a source travelling at CM velocity. Nevertheless, we present the neutron content for the ejectiles in CC-events in fig. 6.6 where the <N>/Z vs Z is reported for the heavier detected fragment of the event. The results are quite similar to those for QP sources, previously discussed: the ratios are much lower than the reference values (drawn as dashed horizontal lines), which correspond to the total colliding systems for the two used targets. Evaporation, and possibly fast emissions, flattens down the mass distribution, for each element. Even for this most dissipative event class, we observe that the more neutron-rich target ($^{48}$Ca) produces fragments slightly richer in neutrons with respect to the neutron-poor one ($^{40}$Ca). The primary sources, either normal density decaying composite nuclei close to barium ions ($Z = 20 + 36$) or expanding multifragmenting systems, preserve memory of the neutron abundance in the ingoing channel.

The study of the CC class of events was not one of the goals of this work and a deeper investigation of these processes has been postponed to other future experiments where the FAZIA telescopes will be coupled with the INDRA multidetector,

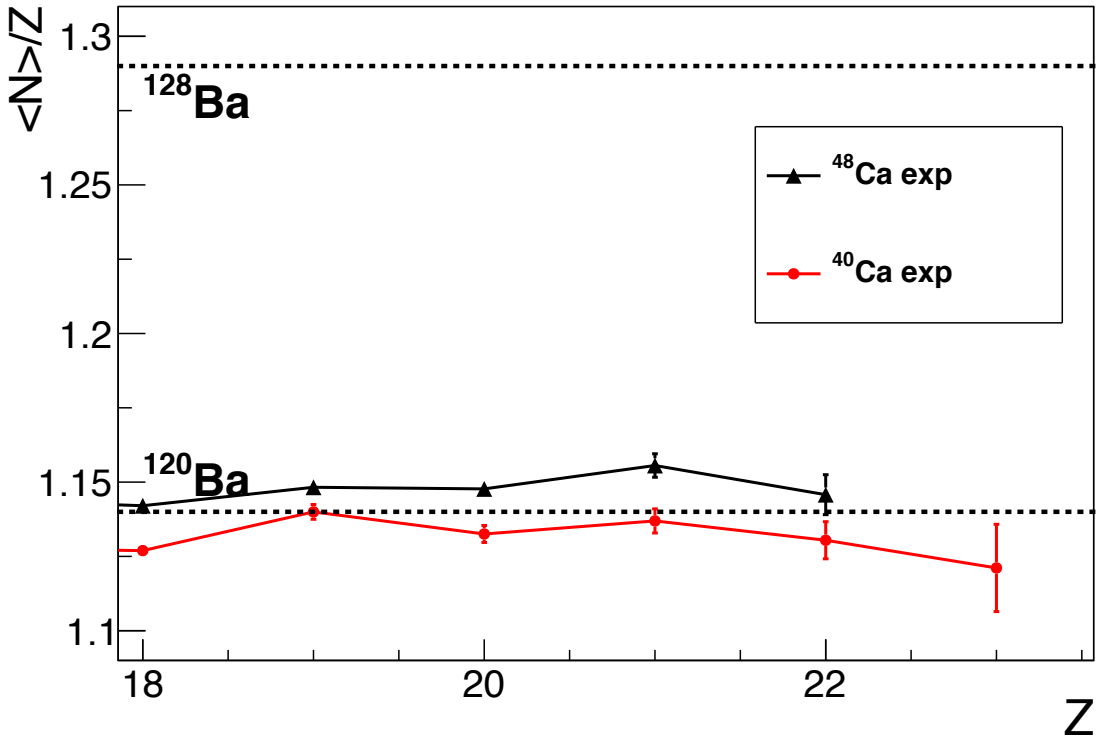


**Figure 6.6:** *Correlation between the <N>/Z of the heavier fragment in a CC class of events with respect to its charge Z. In black and red the results for $^{48}Ca$ and $^{40}Ca$ are reported respectively.*

at GANIL, thus reaching an acceptance larger than 80% of the full solid angle.

## 6.5 Isospin and emission pattern

Recently, the study of the isospin dynamics in binary collisions was enriched by new results coming from very detailed analyses for the mass-symmetric system $^{70}Zn$+$^{70}Zn$ [28, 115] where the isotopic distributions of the QP remnants and the neck fragments were both measured. This was also the leading idea behind the ISO-FAZIA experiment proposal, presented to the Program Advisory Committee of LNS in 2013. Considering the neck fragments emitted after the fast rupture of a deformed QP, the authors of the cited papers try to determine the relaxation time of the isospin unbalance which is produced during the collision due to the preferential neutron migration towards the low-density midvelocity region. The relaxation times and other features of this complex scenario of formation and rupture of a neck are related to the details of the $E_{sym}$ term of the EOS far from normal density. Thus these precise measurements, correlating fragment phase-space and isospin, are quite promising as a way to advance in this studies. The case considered by the authors

was specifically devoted to the isospin drift; in fact, since their colliding system is symmetric, the initial neutron unbalance is zero and no diffusion can contribute to the increase of the neutron richness at midvelocity. Instead, the ISO-FAZIA experiment was devoted mainly to verify the QP behaviour (production, evaporation, fission) when changing the neutron content of the target. In this case both isospin diffusion (already verified and discussed before) and drift play a role. To go into further details it is thus necessary to undertake a more detailed analysis and to consider other correlations, in order to better characterize the origin and the properties of the fragments (see Sec. 4.1.4).

We will concentrate on the IMFs starting from $Z = 3$ up to values that correspond to an almost symmetric fission of the QP. From the isospin dynamics point of view, one would like to have access to the isotopic distributions of both forward emitted fragments (QP + neck or both QP fission fragments), possibly in coincidence with a third partner (an other IMF or a QT remnant). In ISO-FAZIA, mass identification is limited to QP charge below $Z = 23 - 25$. However, for the study of the neck also the very asymmetric configurations, which are the most investigated in the past, are very important because they result in the fastest neck ruptures, corresponding to larger isospin unbalance between the small and big remnants of the split. Also, being due to fast ruptures, the QT-IMF-QP configurations are the most polarized ones, with the three objects almost aligned along the separation axis. In the following we first discuss the lighest fragments in coincidence with a QP and then we move to the QP fission class, which extends to the more symmetric fission configurations.

In order to better identify the fragment origin we can use two ordering variables. The first is $V_{par}$, i.e. the laboratory velocity component along the beam axis. The beam direction, when other reference directions are not available or recognizable, is a natural choice to express the directionality of the reaction. Sometimes, the flight direction of the measured QP is used as a reference instead of the beam. At Fermi energies these two directions are close to each other (the QP flight polar angles are less than six degrees). The second ordering variable implies a "clear" fragmentation time-scale. It can be calculated when one associates a pair of fragments to a split following the previous separation of QP from QT. In this scenario, the QP-QT separation axis is surely the reference direction; if the deformed QP, with an attached neck remnant, breaks into two pieces, the separation axis of this second binary system forms an angle with respect to the QP-QT separation axis, called $\alpha$ and given by:

$$\alpha = acos \frac{\vec{\mathbf{v}_{CM}} \cdot \vec{\mathbf{v}_{rel}}}{\|\vec{\mathbf{v}_{CM}}\| \|\vec{\mathbf{v}_{rel}}\|} \tag{6.1}$$

$\alpha$ is the angle between the direction of the center of mass velocity of the original

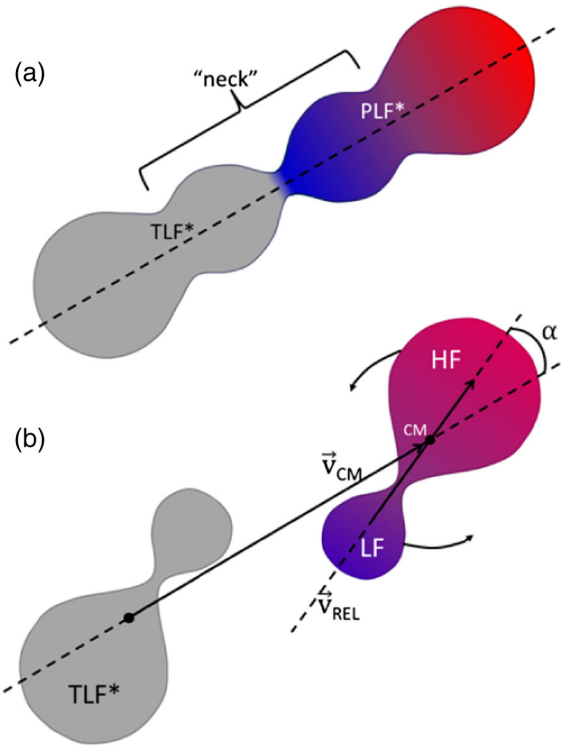


FIG. 1. Illustration of dynamical deformation and decay. Panel (a) shows the deformed PLF* and TLF* system before rupture of the neck. Panel (b) shows a later time after the PLF* and TLF* system has separated. The PLF* has rotated relative to the TLF* separation axis ($\vec{v}_{\rm CM}$) and is itself about to break up into two fragments (**HF** and **LF**). The time the PLF* lives before breaking up is measured by the angle $\alpha$. The color denotes the composition with blue indicating neutron richness and red indicating relative neutron deficiency.

**Figure 6.7:** *Cartoon and caption taken from A. Jedele* et al.*, Phys. Rev. Lett. 118 062501 (2017) [28].*

scissioning nucleus ($\vec{\mathbf{v}_{CM}}$) and the direction of the relative velocity ($\vec{\mathbf{v}_{rel}}$) between the two fragments of the second split. A sketch of these scenarios is given in fig. 6.7 taken from Ref. [28]. As usually assumed in these studies, we assume $\alpha = 0$ when the lighter fragment produced by the QP split is aligned towards midvelocity (i.e. the CM). It is namely this alignement which typically shows the most striking isospin features (neutron enrichment) of the light fragment. The opposite orientation corresponds to the case in which the lighter fragment flights in front of the bigger partner. Much probably, light fragments ($Z = 3, 4$) in these latter configuration are emitted through the 'standard' statistical decay of a hot spinning QP source.

In a semi-classical picture, the $\alpha$ angle is related to the time scale of the process: the smaller the $\alpha$ angle, the faster the fission mechanism, provided we can assume

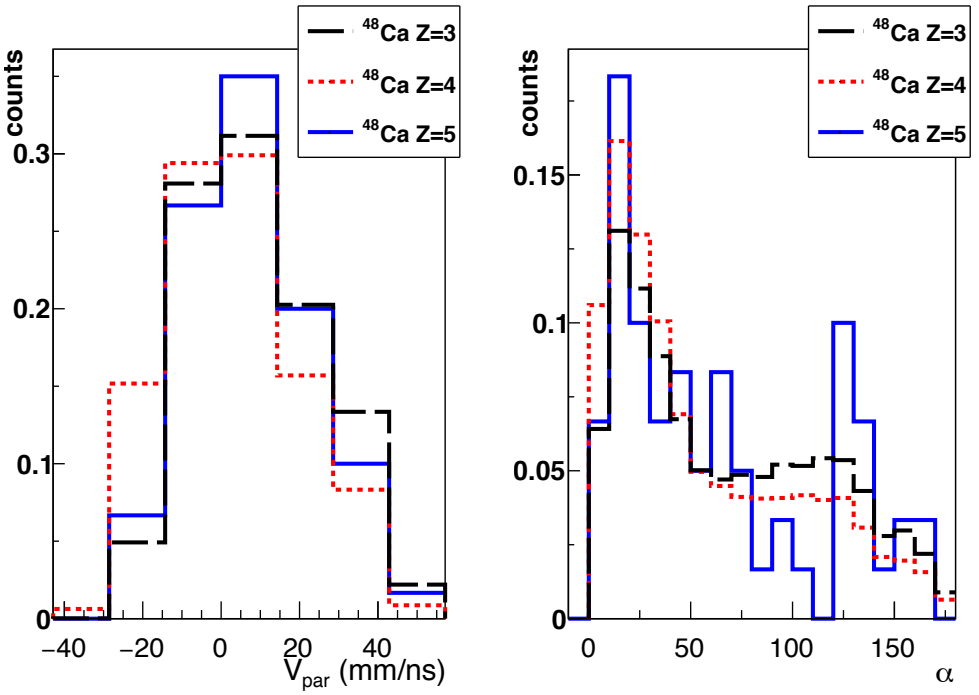


**Figure 6.8:** *Left: Experimental $V_{par}$ distribution for Z=3, 4, 5 in coincidence with a QP for the reaction on $^{48}Ca$. Right: for the same events and ions, the $\alpha$ angle distributions are shown.*

for a given event set a rather constant angular momentum (i.e. rotation velocity). Let's consider now the emission of the lightest fragments in our data. In fig. 6.8 the experimental $V_{par}$ distributions for $Z = 3, 4, 5$ have been reported (for the $^{48}$Ca target). Here, the parallel component has been calculated with respect to the QP velocity in the CM frame. We can see that these IMFs are mostly emitted (around 60%) at midvelocity with a important tail extending more towards the QP region. The QT velocity is at farther distance but some contributing evaporation from the QT cannot be excluded [17]. The right panel shows the $\alpha$ angle distributions for the same IMFs. Such distribution shows that these fragments are mainly produced by the fast splitting of deformed QP. The polarization towards midvelocity of these systems is clearly confirmed with a dominant peak around 20°.

We can now go on and look at the neutron content of these fragments as a function of their emission pattern. This is done in fig. 6.9 where <N>/Z vs. $V_{par}$ is drawn for Lithium (upper panel) and beryllium (bottom panel) observed in coincidence with a QP for the two target reactions ($^{48}$Ca, black triangles and $^{40}$Ca, red squares). Events are for the QP-only and QP-QT selections. The model predictions are drawn as bands with different coloured/shadowed areas to encompass the statistical errors. Here, the main feature, in agreement with other previous findings in the literature, is that for both targets the neutron content increases when moving from

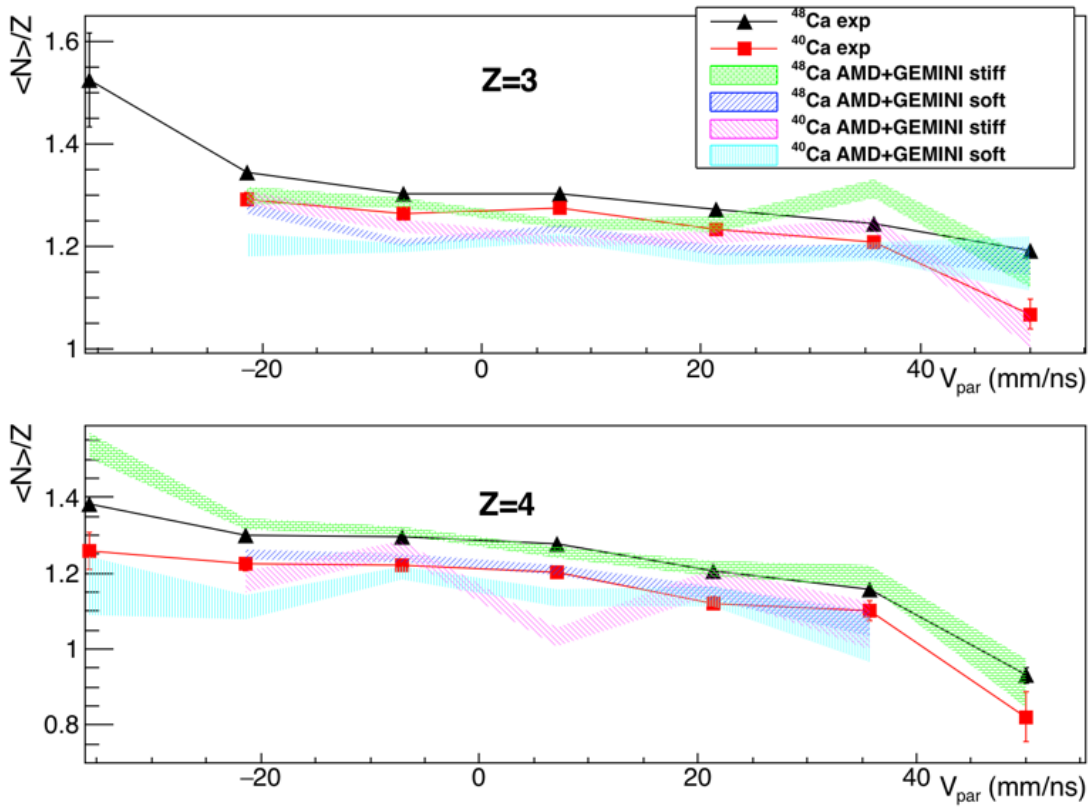


**Figure 6.9:** *$<N>/Z$ vs $V_{par}$ for lithium (top panel) and beryllium (bottom panel) detected in coincidence with a QP (QP-only and QP-QT event sets). The experimental points are marked with black triangles and red squares for $^{48}Ca$ and $^{40}Ca$ respectively. The shaded areas correspond to the model predictions.*

QP velocity towards midvelocity. Fragments formed in the supposed low-density regions are more neutron rich than those formed in the QP region. This effect can be interpreted as an isospin drift effect. We stress here, as a reference example, the very similar isospin behaviour of IMF with $Z = 3, 4$ in the collision $^{58}\mathrm{Ni} + ^{24}\mathrm{Mg}$ at 34.5 MeV/u (figs 2 and 3 of ref [104]).

The fact that the ratios for the $^{48}$Ca target are larger than those for $^{40}$Ca, is the already mentioned hint for isospin diffusion: also in the QP velocity region lithium and beryllium are produced with different isotopic distributions (see Ref. [116] for an example of a similar result).

The experimental data have been compared with the model predictions. Again two options have been tested concerning the dependence of $E_{sym}$ on density. We can observe a slightly better agreement of the stiff parametrization, especially for Be ions. Though this result seems to support previous indications, we must note that the whole agreement with the data is in any case marginal. On the other hand we remind that, as shown in Sec. 4.1.4, the sensitivity of these observables to the asy-stiffness of the EOS is not strong even for primary fragments (i.e. before the

application of the afterburner).

Beside the <N>/Z ratios, also the isotopic ratios (the ratio of the yields of two specific isotopes) and the isobaric ratios (the ratios of the yields of two close isobars) have been studied. Frequently, also LCPs have been included in this kind of analysis [109, 117, 118]. Indeed, notwithstanding their large spread in the phase-space which makes it difficult to determine their sources, the LCP are abundantly emitted and easily identified even by not optimized detectors. The isotopic ratios measured in ISO-FAZIA are plotted in fig. 6.10 for both reactions (for the $^{48}$Ca target with black triangles and for the $^{40}$Ca target with red squares). They are presented as a function of $V_{par}$ in order to attempt a source ordering from QP (high velocities) towards QT (low velocities). In the different panels, from the top left to the bottom right, we report the d/p, t/p, $^{6}He/\alpha$, $^{7}Li/^{7}Be$ and $^{9}Be/^{7}Be$ ratios. All these pairs experience practically the same Coulomb repulsion during the emission by a given source except for the only isobaric pair reported ($^{7}Li/^{7}Be$).

A larger production of neutron-rich species for the $^{48}$Ca target reaction is evident from the picture, as expected. Moreover, the ratios for different targets tend to converge to the same value towards the QP region; this is quite reasonable because the projectile is the same in the two cases and, particularly for LCPs, the velocity distributions are quite wide thus smearing possible small differences. Another observation is the tendence to produce neutron-rich species towards the midvelocity region.

The figure presents also other data for further interesting comments. The comparable results from I. Lombardo et al. [109] on $^{40}$Ca + $^{40,48}$Ca systems are drawn for the Li/Be ratio and for the Be isotopic ratio. The trend is similar (the values for the neutron-rich system are higher); the values in Ref. [109] are systematically lower than the values of the present work. This behaviour is probably related to the reduced neutron content of the lighter systems studied by Lombardo.

Some specific predictions, for d/p and t/p only, obtained running GEMINI for a few reference sources are represented with grey box in the picture ($^{80}$Kr with $E^* = 100 - 150$ MeV, $^{40,48}$Ca with $E^* = 50 - 100$ MeV, with $20\hbar$ spin each). This comparison is limited to only p, d, t yields where GEMINI predictions are more reliable. The box around beam velocity in the QP region represent the results from the $^{80}$Kr source while the boxes corresponding to the excited Ca sources have been drawn in the region of the forward QT emissions. The calculated d/p and t/p ratios for $^{80}$Kr are compatible with the measured QP values, while the ratios at midvelocity are quite larger than the values expected for excited Ca ions, whatever the assumed excitation energy: this is an additional hint for neutron enrichment of the neck region, coming from LCP yields.

A final comparison is proposed in the figure with the more comprehensive AMD

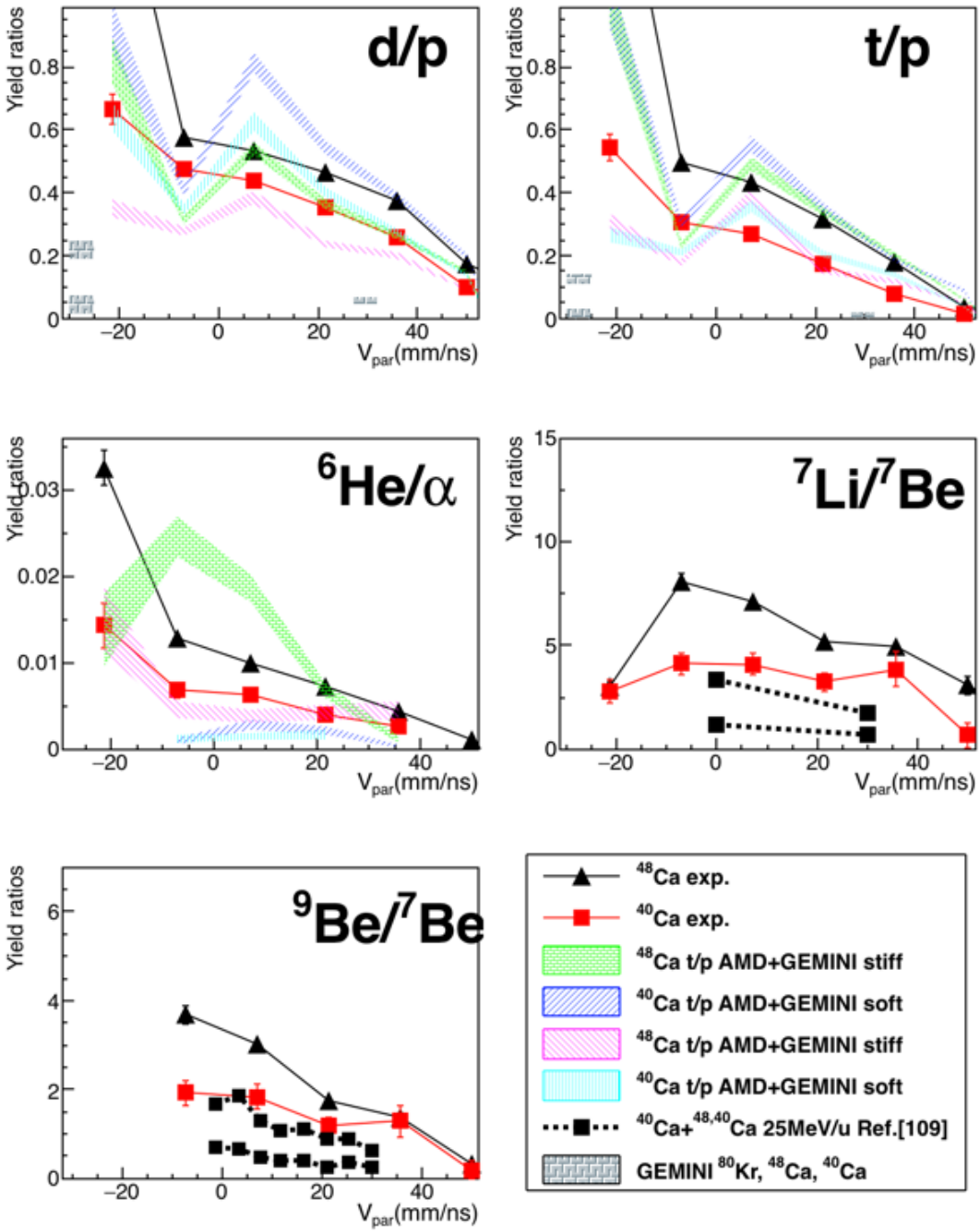


**Figure 6.10:** *Yield ratios between different pairs detected in coincidence with a QP (QP-only plus QP-QT sets) as function of $V_{par}$ in the CM. The black upper triangles (red squares) represents the experimental data on $^{48}Ca$ ($^{40}Ca$) target. The AMD plus GEMINI simulated data have been reported with different colors and shaded area for the different parametrizations used. Some calculations performed with GEMINI are drawn with grey boxes as a reference. Other experimental results from Ref. [109] are also plotted (dashed line and black square markers).*

plus GEMINI calculations. As for IMFs, we have not enough statistics: the too much wide fluctuating bands prevent from doing any conclusion. Instead, we note that for H and He isotopes the model correctly predicts the global behaviour. Specifically, it reproduces the larger ratios for the neutron rich $^{48}$Ca target and the trend toward the QP region where the deuterons and tritons are less abundant. Also, very interestingly, the model nicely describes the strong increase of n-rich isotopes moving into the midvelocity region, with a steep increase in the case of $^{48}$Ca. This observation is relevant because the predictive capability of the model is here severely constrained and therefore it results to be rather satisfying. Coming to the stiffness of $E_{sym}$ as a function of $\rho$, we cannot draw definitive conclusions but only some broad indication. The t/p ratio seems insensitive to the $E_{sym}$ parametrization while there is an indication in favour of a stiff behaviour coming from the d/p and $^{6}$He/$^{4}$He ratios. In fact, the agreement for the asy-soft is quite worse. We remind that an asy-stiff behavior has been also suggested by the previously discussed observables.

## 6.6 Quasi-Projectile fission events

The study of the isospin dynamics also for QP fission events is a very important and original idea of the ISO-FAZIA experiment. Indeed, the QP fission and the neck fragmentation can be viewed as the result of a continuous evolution where the role of the preceeding dynamics is dominant for asymmetric (see Sec. 1.1.3) scissions (neck fragmentation), gradually getting weaker for increasingly symmetric splits. Correspondingly, the time scale of the process get longer.

We remind here that the QP-FIS events contain two fragments with relative velocity 10 mm/ns $< V_{rel} <$ 45 mm/ns (compatible with the standard fission systematics [100]) and a relative angle in the centre of mass frame $40° < \theta^{rel}_{CM} <100°$. In the following, we label as "big" and "small" the heavier and the lighter fragment of the split, respectively. The minimum charge for the small fragment is set to $Z = 5$ and we retain only fission fragment candidates having a summed charge $Z^{sum} > 18$. This is the same lower limit for the QP size adopted in the other event selections.

### 6.6.1 Fission fragments characterization

An important feature of the nuclear scission is the mass (or charge) *asymmetry* of the division, described for instance by an asymmetry parameter $\eta$ defined as:

$$\eta = \frac{Z_{big} - Z_{small}}{Z_{big} + Z_{small}}$$

The value $\eta = 0$ corresponds to symmetric splits. Generally speaking, for the

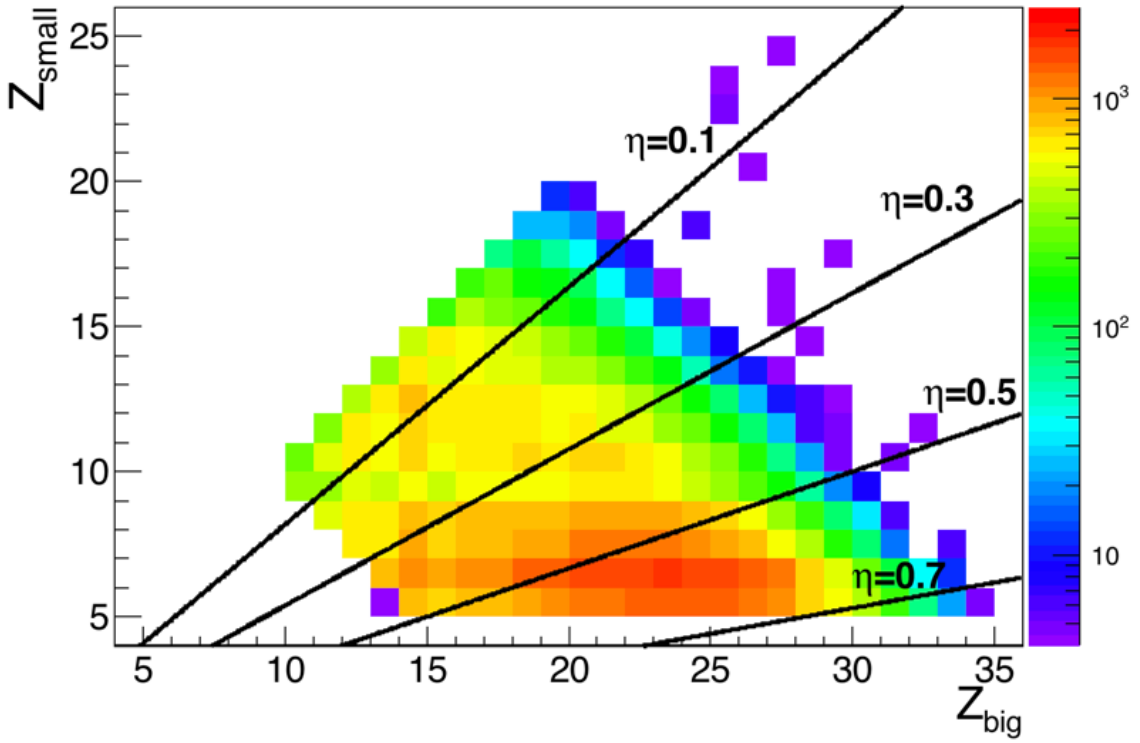


**Figure 6.11:** *Correlation between the Z of the biggest fragment ($Z_{big}$) and the smallest one ($Z_{small}$) for the QP-FIS class of events for $^{48}$Ca system. The black lines correspond to fission with different asymmetry parameter ($\eta$).*

standard nuclear fission, occurring at moderate spin-energy values for very heavy nuclei, the $\eta$ distribution is broad with a hump corresponding to symmetric divisions and an increase for very asymmetric splits towards the evaporation region where light particles and small fragments go with a big daughter residue. In the mass region of the Kr-like QPs of this experiment (most likely $A = 70 - 80$, $Z = 30 - 36$) the fission process is a rare decay mode and preferentially proceeds towards asymmetric breakups without any increase for symmetric splits. Thus, we expect in our data a rather suppressed QP fission channel (we recall the low fission percentages in tab 5.2) dominated by asymmetric splits. The expectation is confirmed by fig. 6.11 where the correlation between the charges of the two fission fragments has been reported for the $^{48}$Ca target. The black lines correspond to different values of $\eta$. The largest part of the measured yield concentrates around pairs with $Z_{big} \approx 18-25$ and $Z_{small} \approx 5-8$ ($\eta > 0.5$). A rough indication of this preferential decay is given by the high yield ratio between the asymmetric and the symmetric splits: $\frac{N_{\eta>0.4}}{N_{\eta<0.2}} = \frac{55 \cdot 10^3}{22 \cdot 10^3} = 2.5$. We note that, at variance with fusion reactions at low energies where one safely assumes the formation of a single source with fixed values of A, Z, E*, here the nuclei undergoing fission are not well constrained in their degrees of freedom. Even the Z, A values

themselves are surely spread because we are observing QP produced over a range of impact parameters. Moreover, we cannot neglect the possible contributions to the increase of the source size fluctuations coming from pre-equilibrium emissions and evaporative decay . This is clearly demonstrated by the fig. 6.11 itself: the correlation in the $Z_{small} - Z_{big}$ plot is not as one would expect for a fixed total charge value (i.e. fixed $Z^{sum} = Z_{small} + Z_{big}$). Therefore the $\eta$ parameter by itself is not sufficient to describe the phenomenon, because the system size can change.

Nevertheless, the asymmetry remains a relevant fission parameter allowing further correlations with other interesting variables. In order to better characterize the fission events, the kinematic features of the parent QP can be reconstructed from those of the assumed fission fragments. As already done in previous Chapters, we label "sum" the QP fragments as reconstructed starting from the fission partners. In fig. 6.12 the average laboratory velocity of QP$^{sum}$ ($V_l^{sum}$) as a function of $\eta$ has been reported for the $^{48}$Ca target (black triangles). $V_l^{sum}$ is a quantity strictly related to the QP velocity before fission and it can be compared with the (average) values of the QP velocity as estimated for the other event classes. These values

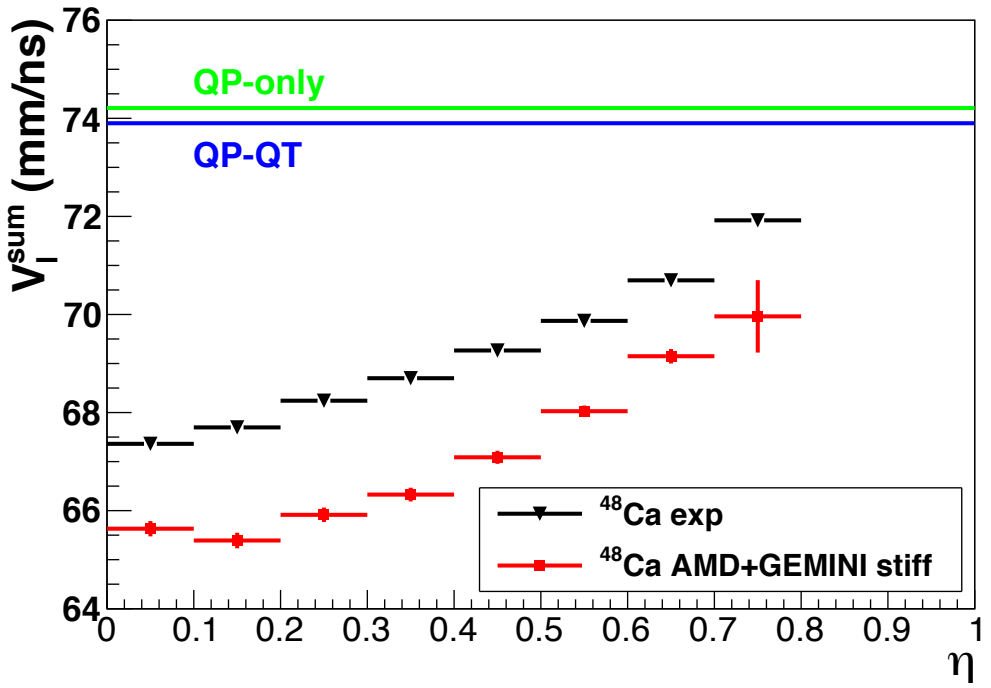


**Figure 6.12:** *Experimental average lab velocity vs. asymmetry $\eta$ of the reconstructed QP$^{sum}$ from fission pairs for the reaction on $^{48}$Ca (black triangles). The green and blue lines correspond to the average velocities for QP observed in the QP-only and QP-QT selection, respectively. The red squares are the AMD+GEMINI model predictions for the QP$^{sum}$ events, for the same target case*

are indicated by the horizontal lines in fig. 6.12 (QP-only in green and QP-QT in blue). The QP$^{sum}$ velocity values are systematically lower than for the other two classes, indicating that this event set corresponds to more dissipative collisions with respect to the classes where the QP (alone or not) is not fissioning. This point was already noticed while discussing fig. 5.19 of Sec. 5.3.3. The evolution with the $\eta$ parameter could be the sign of an impact parameter ordering of the observed fission events, with the more asymmetric splits corresponding to slightly more peripheral collisions. The comprehensive model predictions of the AMD + GEMINI package are drawn with red squares in the same picture. The model follows the trend vs. the mass asymmetry of the measured data but it apparently overestimates the average dissipation of these events because the corresponding velocities are 2 mm/ns below the experimental data.

The events in the QP-FIS class can be viewed as a 3-body process where just after the QP-QT separation, the excited deformed QP breaks up into two pieces. Therefore, as done previously for the neck fragments $Z = 3, 4$, it is very useful to investigate the polarization angle of the fission step with respect to the primary QP-QT axis, as done in the cited recent paper by A. Jedele [28]. We expect that the more symmetric the split, the less polarized is its direction, with the two fragments emitted in a broad angular range, having forgot the original QP-QT direction. This is what can be seen in fig. 6.13 which shows the $cos(\alpha)$ distributions for different $\eta$ intervals, indicated by different colors, for the $^{48}$Ca target. We use this presentation for an easier comparison with the corresponding picture in Ref. [28]. For symmetric fissions the distribution is almost flat but, for increasing asymmetry, the histogram becomes peaked at $cos(\alpha) \approx 1$. The present finding, therefore, nicely confirms the previous results.

### 6.6.2 Isospin of fission fragments

The isotopic distributions of coincident fission fragments, accessible thanks to the excellent performances of the FAZIA telescopes, could provide new information on the reaction dynamics. Several results in the literature pointed out that the asymmetric splits (just resembling very elongated neck ruptures) are faster than the processes leading to more symmetric fission [39]. This means that for symmetric fissions the system has longer lifetimes and thus any initial unbalance possibly induced by the previous collision dynamics (in excitation energy, in neutron content and in deformation) can be smeared out. This is just one of the most relevant observations of Jedele [28] and it could hold also for our data.

To better investigate the isospin features of fission fragments, in fig. 6.14 the neutron content of coincident $Z_{big}$ (left) and $Z_{small}$ (right) fragments has been studied for

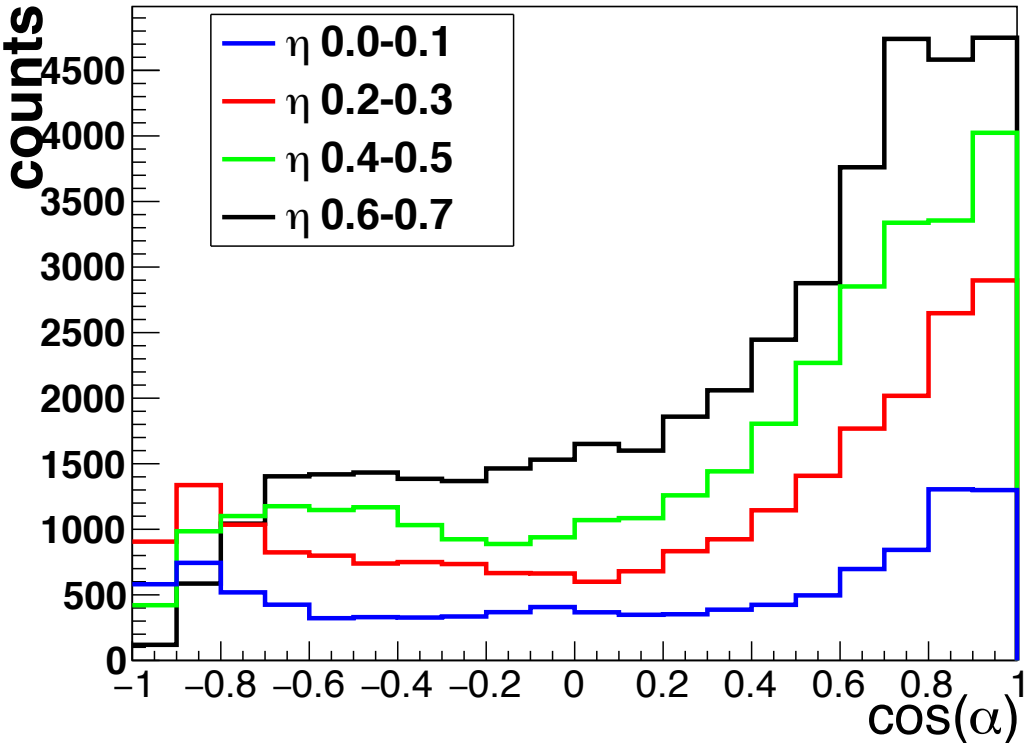


**Figure 6.13:** *Experimental $cos(\alpha)$ distribution (see text) for different $\eta$ intervals for QP-FIS events collected for the $^{80}Kr$+$^{48}Ca$ reaction.*

two well separated $\eta$ intervals: black triangles correspond to the symmetric fission gate ($\eta < 0.25$) while red circles correspond to the asymmetric splits ($\eta > 0.45$). We only show the results of the reaction on $^{48}$Ca because of the lower statistics collected for $^{40}$Ca. The latter features a similar behaviour but with less evident effects (because of the overall lower neutron richness). We observe that the neutron contents of $Z_{big}$ and $Z_{small}$ depend on the mass asymmetry. They are more different for asymmetric splits and tend to become similar for symmetric breakups. In other words, for the symmetric fissions the isospin degree of freedom tends to be more equilibrated. This feature is compatible with the previous observation that the measured symmetric fission corresponds to more central collisions than the asymmetric fission and also with all previous indications that, even for a fixed region of impact parameters (i.e. for a given energy dissipation), the process of symmetric split is slower.

In fig. 6.14 the two $\eta$ intervals are rather large and, since we are measuring a variety of splitting QPs, sources with different initial sizes are included. For example, when we look at $Z_{big} = 17$ the condition $\eta < 0.25$ selects a smaller partner with charge from $Z = 10$ to $Z = 17$ thus coming from initial QP nucleus having $Z^{sum}$ from 27 to 34. The same $Z_{big} = 17$ with the condition $\eta > 0.45$ selects lighter partners in

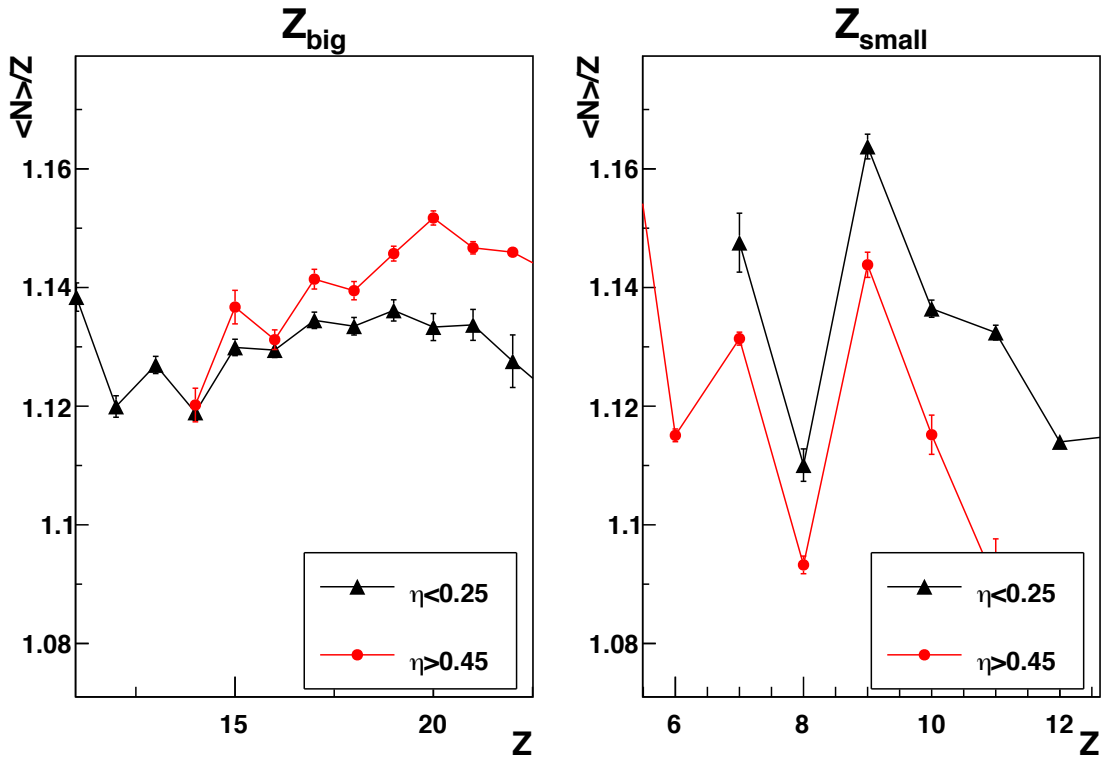


**Figure 6.14:** *Experimental <N>/Z vs. charge Z of the heavier (lighter) fission fragment is drawn in the left (right) panel for the reaction on the $^{48}Ca$ target. In each panel the black triangles and the red circles correspond to the values obtained for the events with $\eta < 0.25$ and $\eta > 0.45$ respectively.*

the range $Z_{small} = 1 - 6$, corresponding to initial QP sources with charge from 18 to 23.

In order to reduce the mixing of informations associated to the source and the fission fragments, introduced by these variables, we try to select specific decay channels as done in Ref. [28]. The available statistics in ISO-FAZIA definitely rules out the surely interesting comparison between the two targets. We select four different cases corresponding to various fission mass asymmetries (and $QP^{sum}$ sizes). Ordered as a function of decreasing asymmetry, the groups are: $Z_{small}$=5 and $Z_{big}$=20, 21; $Z_{small}$=5 and $Z_{big}$=17, 18; $Z_{small}$=9 and $Z_{big}$=16, 17 and $Z_{small}$=10, 11 and $Z_{big} = 15 \div 18$. The $\eta$ values are about 0.60, 0.55, 0.29 respectively for the first three cases while $\eta$ spans the range $0.33 \div 0.15$ for the last group; the measured $Z^{sum}$ changes from 61% to 80% of the projectile charge. For comparison, we remind that for the pairs considered by Jedele the $Z^{sum}$ is around 60% of the projectile charge and the studied asymmetry range is $\eta = 0.26 \div 0.47$.

In fig. 6.15 the observable $\Delta =< (N - Z)/A >$ (the same observable used in Ref. [28]) with has been reported as a function of the $\alpha$ angle. The limited statistics

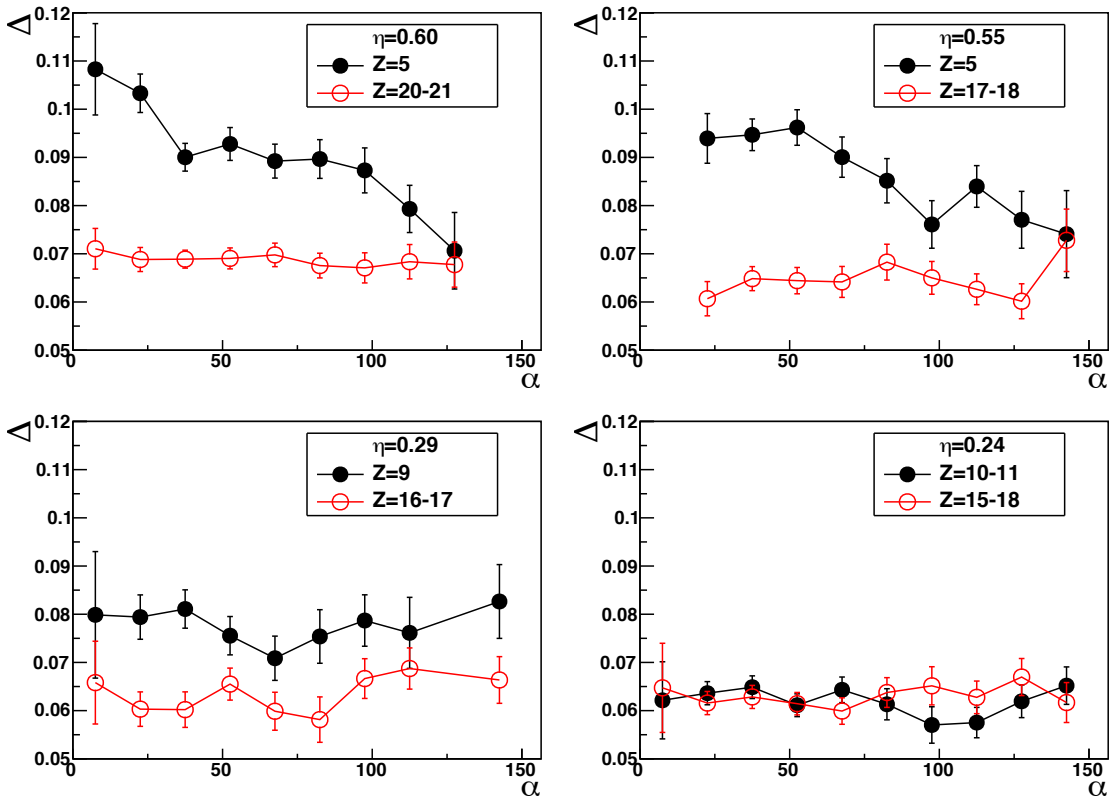


**Figure 6.15:** $\Delta =< (N-Z)/A >$ *as a function of the* $\alpha$ *angle for experimental data acquired for the* $^{48}Ca$ *target. Full black circles:* $\Delta$ *value for the smallest fission partner. Empty red circles:* $\Delta$ *value for the biggest fission partner. When needed, in order to increase the statistics for a given* $\eta$*, fragments with similar Z values have been grouped. The different panels are ordered from the top left to the bottom right as a function of decreasing asymmetry.*

of our experiment does not allow for a refined analysis of the $\alpha$ angle evolution, like the one of Ref. [28]. However, we can still observe similar trends. Namely, we see that for the most asymmetric fission steps the isospin values ($\Delta$) are different when the light fragment is in between QP and QT while they tend to be equal for the opposite orientation. The strongest effect is associated to the most asymmetric split and the effect gets weaker when moving to more symmetric breakups. The isospin variation with the angle is larger for the small partner ($Z = 5$) and it is weak for the heavier one. For the symmetric fission group, the $\Delta$ distributions are flat.

This result represents a positive and independent confirmation of the trend observed by many previous papers, e.g. in the more refined analysis recently proposed by Refs. [28, 115]. Future experiments with FAZIA, also complemented with INDRA as already in the plans of the collaboration, will be a good opportunity to investigate the details of the isospin dynamics.

### 6.6.3 Comparison with the evaporation attractor line

The argument treated in this Section, as far as we know, has been never proposed before. First we remind the semi-empirical study by R. J. Charity [10] (described in Sec. 1.1.2) about the loci in the N vs Z nuclide chart that are populated by the excited nuclei during and at the end of their evaporation path, called EAL (Evaporation Attractor Line). It is essentially a region close to the $\beta$-stability line[1], slightly displaced towards the proton rich side with respect to $\beta$-stability. An excited nucleus reaches the EAL if its initial N, Z values and excitation energy are such as to allow for a "long" evaporative path. It is important to stress that the EAL line cannot be crossed during a given decay path: primary proton-rich nuclei will tend to the EAL from one side, while primary neutron rich nuclei from the other side.

We studied the <N>/Z ratio of the coincident fission fragments and of the reconstructed QP (QP$^{sum}$). Of course the Z-range of the QP$^{sum}$ extends quite beyond the limits of single ion identification ($Z = 25$). In principle, the FAZIA telescopes can give access to the isotopic distributions of the QP$^{sum}$ nuclei as heavy as the Kr-projectile only in the case of (almost) symmetric fission; indeed, for asymmetric splits we have access to a reduced range of isotopic distributions.

In fig. 6.16 we present the experimental results for the $^{48}Ca$ (upper panel) and the $^{40}Ca$ (bottom panel). The <N>/Z values are shown as a function of Z for the two separated fission fragments ($Z_{big}$ and $Z_{small}$) and for the QP$^{sum}$ event by event. The experimental points are compared with the EAL parametrization.

The following observations can be done. As expected and as found for all previous comparisons discussed in this thesis, the reaction on $^{48}$Ca target produces more neutron rich (fission) fragments. We see that for the case of $^{48}$Ca, the isospin stays above the EAL line up to the heaviest identifiable ions while they run just along the EAL line for $^{40}$Ca. In fact, for $^{48}$Ca, the neutron rich parent (hot) primary sources tend to the EAL from the top but they don't reach it. Instead, for the neutron deficient Ca target, the primary ions at the beginning of their decays lie closer to the EAL so that the final (detected) products are also found close to the EAL. It is worth mentioning that the isospin of light fragments (the small fission-like partners) can be quite high, especially for odd Z ions, for both targets. The QP$^{sum}$ behaves quite differently. Whatever the target is, the fissioning sources are most probably Kr-like nuclei (say with Z$< 30-32$ to allow for some dissipation to occur, as confirmed by looking at the primary QP ending in the QP-FIS selection produced by the AMD code). For the $^{40}$Ca target, even admitting the extreme hypothesis of full charge equilibration, the initial source would have <N>/Z = 1.14, i.e. a value almost on the EAL line. The experimental points, instead, fall below the EAL. A

[1]The neutron difference $\delta$N between the two "lines" for $Z = 20$ is $\delta N = 0.33$.

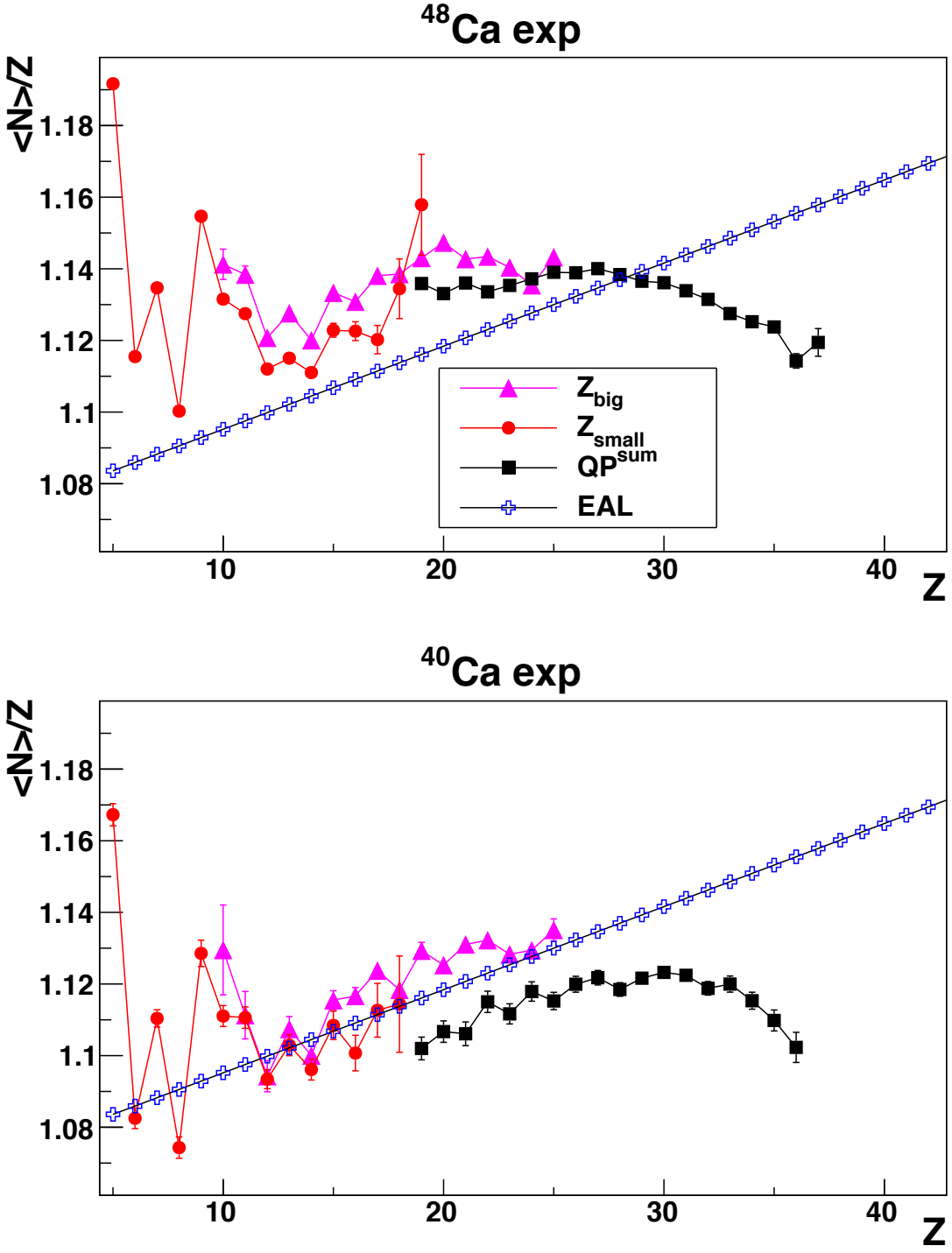


**Figure 6.16:** *Experimental <N>/Z as a function of the charge Z for both fission fragments ($Z_{big}$, magenta triangles; $Z_{small}$, red circles) and for the reconstructed QP ($Z^{sum}$, black squares). In the top (bottom) panel the reaction on $^{48}Ca$ ($^{40}Ca$) target is shown. The blue crosses indicate the EAL parametrization.*

fortiori, in the case of the neutron rich Ca target, for which the equilibrium N/Z value is 1.29, the many points falling below the EAL line are unexpected. Assuming,

on the contrary, the complete absence of isospin diffusion one can refer to the $^{80}$Kr isospin which corresponds to 1.22, in any case much higher than the EAL. The AMD code suggests primary QP sources with a broad distribution of isospin values, around $1.15 \div 1.2$, at the time of 500 fm/c when the afterburner is switched on.

Therefore, in any case, we are forced to consider n-rich primary fissioning nuclei (with respect to the EAL) whose decay cannot ever cross this line or move from it. The findings result to be conflicting with these general arguments.

A way to reconcile this result is to consider the order in time of the two processes of evaporation and fission. Let's assume, for clearness of presentation, two extreme scenarios as depicted in the cartoon of fig. 6.17. In the scenario *A*) the fission step is very slow and the primary QP$^*$ ions have time to emit particles populating a region of remnants which then break apart. Adding up the coincident fragments, which should be cold and close to the EAL, we should track back to the cold QP$^{sum}$ which therefore should be close to the EAL, either from the proton or neutron rich side of it. In the opposite extreme scenario (case *B*), the fission is fast and preceeds the evaporation from the two independent daughter fragments. It is clear that in this case, adding up the two coincident cold fragments leads to an erroneous QP$^{sum}$ source and the EAL related criterium is violated though it is still valid for

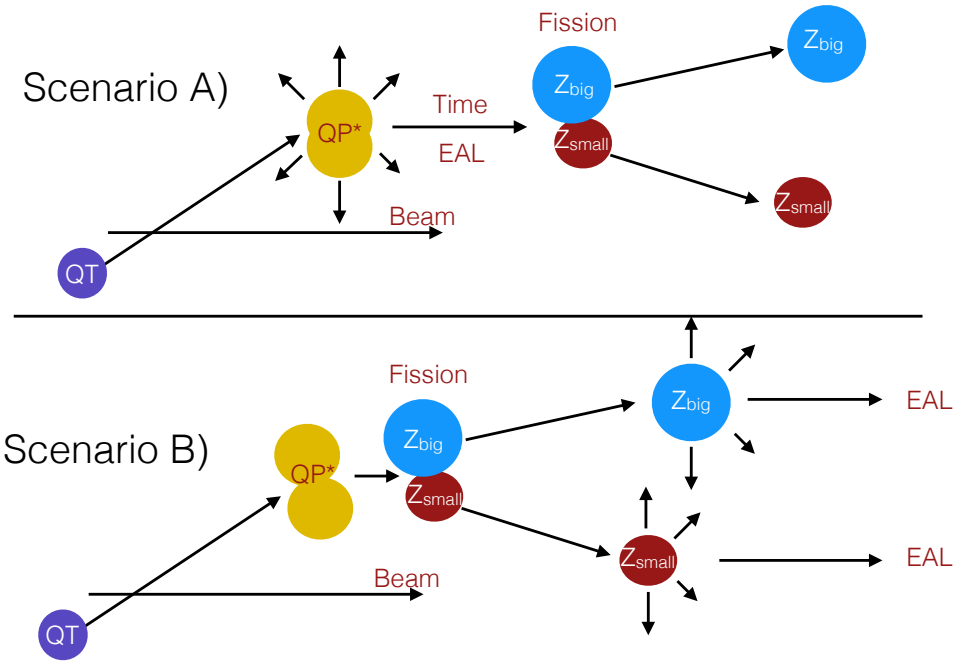


**Figure 6.17:** *Sketch of the two extreme scenarios discussed in the text: A) evaporation preceding the slow (statistical) fission, B) a fast (dynamical) fission precedes evaporation from the fragments*

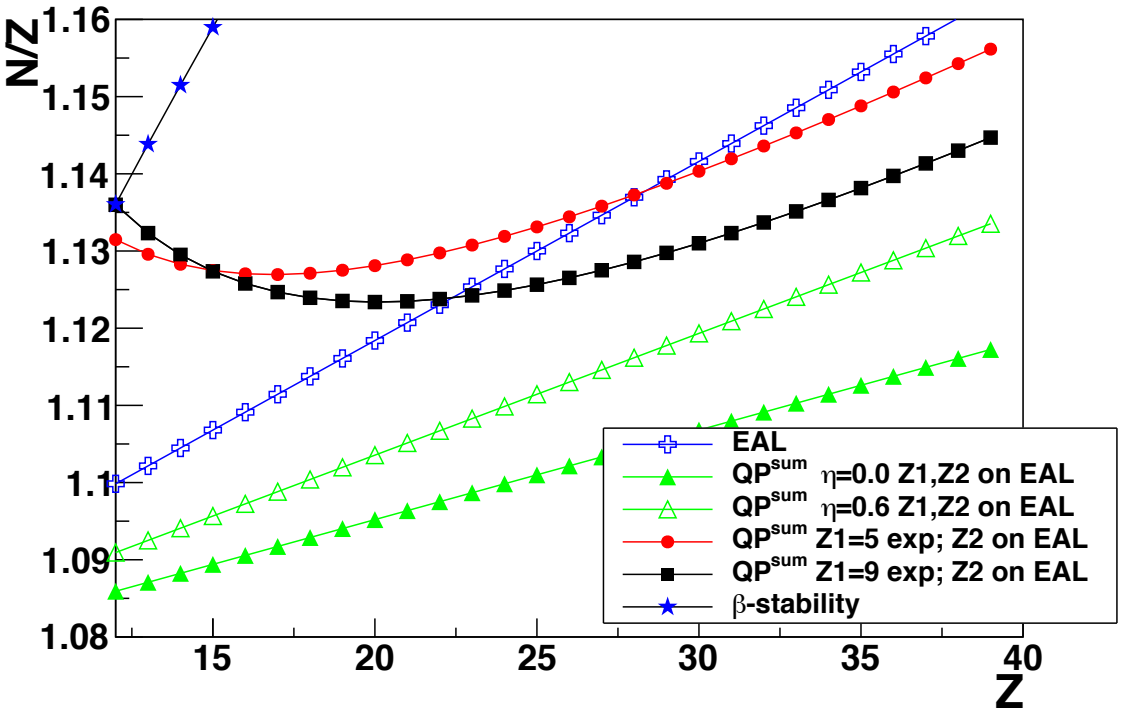


**Figure 6.18:** *Calculated N/Z for reconstructed QP ($QP^{sum}$) by summing event by event the two fission fragments. Four cases are displayed as written in the legenda. See text for details.*

the two individual $Z_{big}$ and $Z_{small}$ ions. The data suggest this second scenario, for both target reactions, more evidently in the region of the heaviest reconstructed QP (corresponding to more symmetric splits). We believe that this is an additional, innovative and model independent confirmation of a fission step which is generally fast with respect to the typical evaporation times.

In order to validate this idea, in fig. 6.18 simple calculation results are shown. The isospin ratios for nuclei on the EAL and on the $\beta$-stability lines are drawn as references. Then the N/Z values are reported for $QP^{sum}$ by summing the final fission fragments, under different hypotheses of their neutron to proton ratio and for different split asymmetries. The green triangles correspond to the assumption of final fragments both on the EAL (filled symbol for two equal fragments, open symbol for $\eta$=0.6 which is close to the maximum considered experimental value studied). If the fragments are both on the EAL, their sum cannot fall on the EAL. We also see that the difference with the EAL is larger for symmetric splits. The other two lines represent hybrid assumptions: namely the smallest fragment is fixed at a value $Z = 5$ (red curve) and $Z = 9$ (black curve) and their assigned N/Z value is taken from the data. This N/Z is relatively higher than the EAL recipe. The N/Z of the larger fragment, in both cases, is the EAL calculated value. We can see that the

isospin of the $QP^{sum}$ can actually cross the EAL at certain Z values in a way that depends on various parameters which are not fully under control in our calculations. What we have found is compatible with the idea that the two fission fragments mainly evaporate after the split and thus, if summed, give $QP^{sum}$ below the EAL. In case of asymmetric splits, since the neutron content of the smaller partner can be very high (red circles of fig. 6.16), there is a partial counterbalance of the effect and the final apparent N/Z for $QP^{sum}$ result to be high, even above the EAL.

The two proposed scenarios and the related calculations are of course only extreme examples. Moreover, the fission split introduces new characterizing quantities (mass and charge asymmetry, fission axis orientation) that can reflect/impact in different manners on the process lifetimes and can be more or less related to the collision dynamics.

In this respect, the previous findings on the correlation between the polarization angle and the isospin content and henceforth times favour an asymmetric fission faster than the symmetric one. This last additional comparison with EAL confirms the short timescales involved in the QP splits, probably strongly influenced by the dynamics and less by statistical concepts. Indeed, by studying the AMD simulated events that are classified as QP-FIS, we checked the validity of this argument. Most fissions are of dynamical type (only one fission over ten cases is produced by GEMINI, i.e. is statistical fission) and they appear to be quite fast: two main fission fragments from QP clearly reseparate within 300 fm/c (1∼zs) from the start of the collision. This time is quite shorter that the typical relaxation time for particle evaporation.

Figure. 6.19 shows in two distinct panels the N/Z vs. Z for the experiment ($^{48}$Ca target) and for the simulated data. QP-FIS events have been separated in two subsets of symmetric ($\eta < 0.25$) and asymmetric fissions ($\eta > 0.45$). We observe that, qualitatively, the behaviour is the one expected. The asymmetric fissions, thanks to the presence of a neutron-rich light fragment can have N/Z values larger than symmetric fissions. The crossing of the EAL, at a certain point, suggests that the breakup is faster than evaporation. The comparison with the model shows that the refined AMD+GEMINI calculations are able to reproduce at least the major aspects. Although with large fluctuations due to the low statistics, the model predicts larger isospin for the asymmetric cases and also the crossing of the EAL. In the model this is not surprising because, as mentioned before, the large majority of the events labeled as QP-fission correspond to rapid ruptures of a system whose shape is strongly perturbed by the violent collision dynamics.

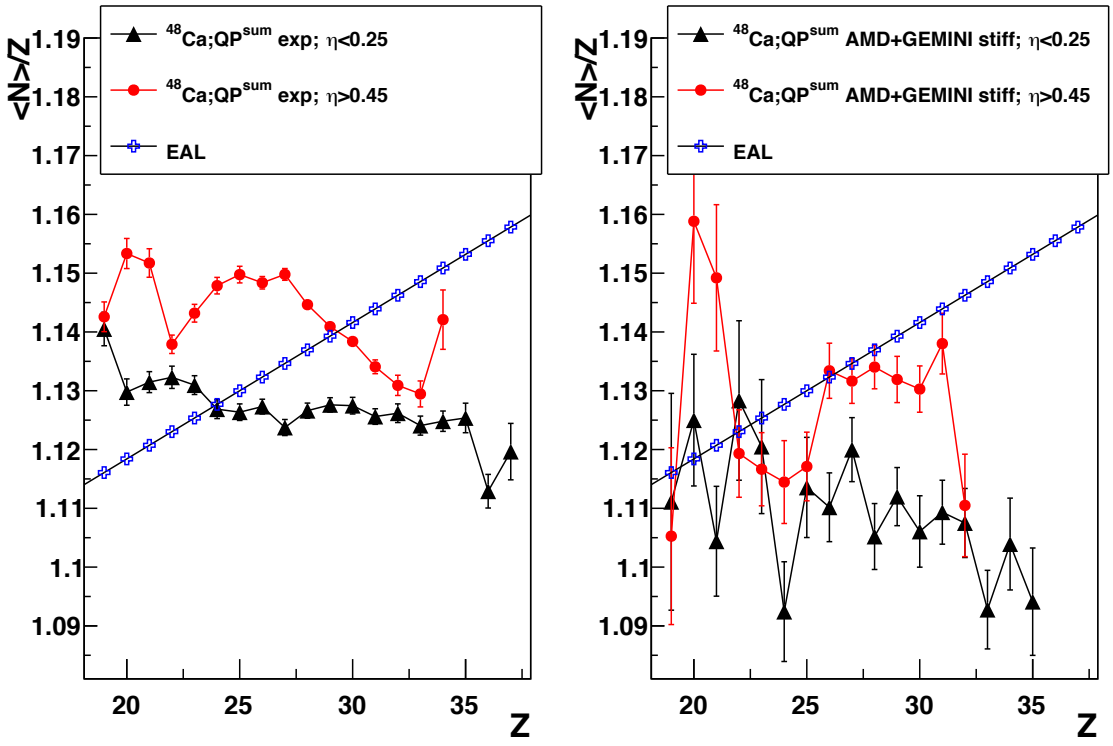


**Figure 6.19:** *Experimental (left panel) and AMD+GEMINI calculated (right panel) N/Z vs. the charge Z of the fragments for QP-FIS events. The figure shows the data separated in the two indicated intervals of η. Asymmetric splits are red points, symmetric splits are black triangles*

# Summary and Conclusions

This work concerns the analysis of the data collected during the ISO-FAZIA experiment, exploiting the reactions $^{80}Kr + ^{40,48}Ca$ at 35 MeV/u. ISO-FAZIA is the first physics measurement completely based on the FAZIA apparatus and it was performed with four blocks of telescopes, covering polar angles between 5° and 17°. ISO-FAZIA is aimed at investigating the isospin transport phenomena, taking advantage of the good isotopic resolution (up to Z∼25, also with low energy thresholds) of the setup, in order to gain information on the density dependence of the symmetry energy term of the nuclear equation of state. Another goal of the experiment is the investigation of the QP fission process, by determining the mass and the charge of the two fission fragments in coincidence, in order to gain information on the time scale of the process from the isospin content of the two fragments. After going through the calibration phase, described in Chapter 3, the work was devoted to the analysis of the experimental data and to their comparison with the predictions of a dynamical model, the AMD code coupled to GEMINI++ as afterburner, with asy-stiff and asy-soft parametrization of the symmetry energy.

The modest geometrical efficiency of the apparatus used for this pioneering FAZIA experiment did not allow for the collection of high statistics, especially for complete events. Therefore, basing on the well known phenomenology of the main reaction types, the data were arranged in four different classes according to their characteristics. In particular, we were able to separate semiperipheral collisions in which the QP was detected alone or together with the QT (identified thanks to the PSA technique), events in which the QP fissioned producing two asymmetric or (less frequently) symmetric fragments, and central multifragmentation events.

A clear effect of isospin diffusion, due to the isospin asymmetry of the entrance channel, was to evidenced by looking at the average isospin of the QP remnants as a function of their charge in semiperipheral collisions, which resulted higher when the target was the neutron rich $^{48}Ca$ (see fig. 6.1 and 6.2). Moreover, the light products emitted in the QP rapidity region showed an isospin enhancement when the target was the neutron rich one (see fig. 6.9 and 6.10). Such an effect was clearly predicted also by the model, but the sensitivity of these observables to the stiffness

of the symmetry energy remains weak. Evidences of isospin drift, due to the density gradient between the QP region at normal density and the low density neck zone, were also found, as shown in fig. 6.9 and 6.10, in agreement with previous findings reported in the literature (e.g. [40, 99, 109, 110]). In fact, a neutron enrichment of light products emitted at midvelocity with respect to those emitted close to the QP velocity was observed both for IMF's (fig. 6.9, <N>/Z of Li and Be) and for the LCP's (isotopic ratios plotted in fig. 6.10). Again, the sensitivity to the symmetry energy parametrization is again weak, although the asy-stiff one seems to better reproduce the experimental data, as also suggested by De Filippo [99]. A higher sensitivity to the $E_{sym}$ resulted for the second moment of the isotopic distribution of the midvelocity IMFs (fig. 6.5), although the small available statistics of the model limited the comparison to very few values of Z. Again, the asy-stiff parametrization seems to better reproduce the data.

Concerning the QP fission, a clear evolution of the emission pattern moving from symmetric (small $\eta$) towards asymmetric (high $\eta$) splitting was observed, as shown in fig. 6.13, with the asymmetric case corresponding to a more aligned configuration, i.e. with the smaller fragment emitted towards the QT. Such an evolution is consistent with several previous experimental observations (e.g. [26, 28]), showing that the larger the mass asymmetry the faster the splitting so that for large mass asymmetries, the system had not enough time to rotate before splitting. This fact is coherent with a predominance of the dynamical fission when the splitting is asymmetric with respect to the symmetric case which appears to be more relaxed.

An original way introduced in this thesis to present the fission data was to compare the <N>/Z of the reconstructed QP on an event by event basis with the EAL parametrization [10], as shown in fig. 6.16 and 6.19; this is obviously possible only when the mass of both fission fragments is measured in coincidence. The striking observation emerging from this picture is the fact that the EAL line is crossed, at variance with the behaviour of a standard evaporation de-excitation. On the contrary, the <N>/Z of the each fission fragment stays close to (and doesn't cross) the EAL line, as expected for cold nuclide after some evaporative decay. This result is a further confirmation of the fact that the fission is mainly of dynamical origin (as clearly suggested also by the model) and takes places on very short time scales (below 300 fm/c). The emerging scenario is that the deformed QP quickly breaks up into two main fragments that possibly undergo evaporation afterwards.

The very interesting results obtained in this work demonstrate that a further investigation of these topics in similar reactions is in order in the next few years, especially when 12 FAZIA blocks will be coupled to the INDRA detector [42] at GANIL, thus allowing a almost complete coverage of the solid angle. In this way it will be possible to better constrain the different classes of events and possibly

separate in a clean way the midvelocity contribution from evaporative emission, maybe extracting further hints on the symmetry energy parametrization. Moreover, the completeness of the data will allow to consider other observables sensitive to the stiffness, as, for example, p-p correlation in central events [119] and the isotopic distribution of the heaviest nuclides after a multifragmentation [120].

# Bibliography


[1] M. D. Toro, et al., J. Phys. G **37**, 083101 (2010).

[2] B. Li, et al., *Isospin physics in heavy-ion collisions at intermediate energies* (Nova, 2001).

[3] M. Colonna, et al., Eur. Phys. J. A **50**, 30 (2014).

[4] A. Ono, et al., Prog. Theor. Phys. **87**, 1185 (1992).

[5] R. Charity, et al., Nuclear Physics A **483**, 371 (1988).

[6] J. Tõke, et al., Phys. Rev. Lett. **75**, 2920 (1995).

[7] V. Baran, et al., Phys. Rev. C **72**, 064620 (2005).

[8] M. B. Tsang, et al., Phys. Rev. Lett. **92**, 062701 (2004).

[9] R. Bougault, et al., Eur. Phys. J. A **50**, 47 (2014).

[10] R. J. Charity, Phys. Rev. C **58**, 1073 (1998).

[11] G. Pastore, et al., Nucl. Instrum. and Meth. A **860**, 42 (2017).

[12] W. Hauser, et al., Phys. Rev. **87**, 366 (1952).

[13] J. Gosset, et al., Phys. Rev. C **16**, 629 (1977).

[14] D. Durand, *Nuclear dynamics in the nucleonic regime* (IOP, 2001).

[15] Di Toro, M., et al., Eur. Phys. J. A **30**, 65 (2006).

[16] G. Casini, et al., Phys. Rev. Lett. **71**, 2567 (1993).

[17] S. Piantelli, et al., Phys. Rev. Lett. **88**, 052701 (2002).

[18] V. Baran, et al., Nuclear Physics A **730**, 329 (2004).

[19] V. Baran, et al., Phys. Rep. **410**, 335 (2005).

[20] B. Faure-Ramstein, et al., Nuclear Physics A **586**, 533 (1995).

[21] F. Auger, et al., Phys. Rev. C **35**, 190 (1987).

[22] B. Borderie, et al., Prog. Part. Nucl. Phys. **61**, 551 (2008).

[23] L. Wolfestein, et al., Phys. Rev. **82**, 690 (1951).

[24] W. Hauser, et al., Phys. Rev. **87**, 366 (1952).

[25] P. Glassel, et al., Z. Phys. A **310**, 189 (1983).

[26] A. A. Stefanini, et al., Z. Phys. A **351**, 167 (1995).

[27] P. Russotto, et al., Phys. Rev. C **81**, 064605 (2010).

[28] A. Jedele, et al., Phys. Rev. Lett. **118**, 062501 (2017).

[29] J. Wilczinski, et al., Phys. Rev. C **81**, 067604 (2010).

[30] M. B. Tsang, et al., Phys. Rev. C **86**, 015803 (2012).

[31] Iida, Kei, et al., Eur. Phys. J. A **50**, 42 (2014).

[32] C. J. Horowitz, Eur. Phys. J. A **30**, 303 (2006).

[33] G. N. William, et al., Eur. Phys. J. A **50**, 41 (2014).

[34] A. Klimkiewicz, et al., Phys. Rev. C **76**, 051603 (2007).

[35] P. Danielewicz, Nuclear Physics A **727**, 233 (2003).

[36] B. Li, et al., Physics Letters B **727**, 276 (2013).

[37] M. Colonna, et al., Eur. Phys. J. A **30**, 165 (2006).

[38] L. Shi, et al., Phys. Rev. C **68**, 064604 (2003).

[39] E. De Filippo, et al., Eur. Phys. J. A **50**, 32 (2014).

[40] S. Barlini, et al., Phys. Rev. C **87**, 054607 (2013).

[41] `http://fazia.in2p3.fr`.

[42] J. Pouthas, et al., Nucl. Instrum. Methods A **357**, 418 (1995).

[43] L. Bardelli, et al., Nucl. Instrum. Methods A **654**, 272 (2011).

[44] N. L. Neindre, Nucl. Instrum. Methods A **701**, 145 (2013).

[45] S. Valdré, Bachelor Thesys (2008-2009).

[46] F. Salomon, et al., Eur. Phys. J. WOC **88**, 01015 (2015).

[47] F. Salomon, et al., Journal Instrum. **11**, C01064 (2016).

[48] G. F. Knoll, *Radiation detection and measurement* (Wiley, 2010).

[49] C. A. Ammerlaan., Nucl. Instrum. Methods A **22**, 189 (1963).

[50] J. England, et al., Nucl. Instrum. Methods A **280**, 291 (1989).

[51] G. Pausch, et al., Nucl. Instrum. Methods A **337**, 573 (1994).

[52] G. Pausch, et al., Nucl. Instrum. Methods A **322**, 43 (1992).

[53] S. Barlini, et al., Nucl. Instrum. Methods A **600**, 644 (2009).

[54] G. Pasquali, et al., Eur. Phys. J. A **50**, 86 (2014).

[55] P. Tove, et al., Nucl. Instrum. Methods **51**, 261 (1967).

[56] H. O. Neidel, et al., Nucl. Instrum. Methods A **212**, 299 (1983).

[57] W. Bohne, et al., Nucl. Instrum. Methods A **240**, 145 (1985).

[58] D. Gruyer, PhD Thesys (2014).

[59] L. Bardelli, et al., Nucl. Instrum. Methods A **602**, 501 (2009).

[60] S. Carboni, et al., Nucl. Instrum. Methods A **664**, 251 (2012).

[61] L. Bardelli, et al., Nucl. Instrum. Methods A **560**, 524 (2006).

[62] L. Bardelli, *Developments of sampling and digital signal processing techniques with applications to nuclear physics detectors* (PhD Thesis, 2005).

[63] J. A. Dueñas, et al., Nucl. Instrum. Methods A **676**, 70 (2012).

[64] L Bardelli, et al., Nucl. Instrum. Methods A **521**, 480 (2004).

[65] H. Hou, et al., IEEE Trans. Acoust., Speech, Signal Processing **26**, 508 (1978).

[66] T. Kurahashi, et al., Nucl. Instrum. Methods A **422**, 385 (1999).

[67] S. Smith, *The scientist and engineer's guide to digital signal processing* (1997).

[68] R. Winyard, et al., Nucl. Instrum. Methods **95**, 141 (1971).

[69] M. Colonna, et al., Nuclear Physics A **642**, 449 (1998).

[70] A. Guarnera, et al., Physics Letters B **373**, 267 (1996).

[71] `https://cc.in2p3.fr`.

[72] `http://indra.in2p3.fr/kaliveda/`.

[73] `https://root.cern.ch`.

[74] R. J. Charity, Phys. Rev. C **82**, 014610 (2010).

[75] O.Lopez, et al., Proceeding IWM 2009 **101**, 148 (2010).

[76] F. Hubert, et al., At. and Nucl. Data Tab. **46**, 1 (1990).

[77] M. Pârlog, et al., Nucl. Instrum. and Meth. A **482**, 674 (2002).

[78] M. Pârlog, et al., Nucl. Instrum. and Meth. A **482**, 693 (2002).

[79] B. Blank, et al., Phys. Rev. C **50**, 2398 (1994).

[80] P. Napolitani, et al., Phys. Rev. C **76**, 064609 (2007).

[81] Y. P. Viyogi, et al., Phys. Rev. Lett. **42**, 33 (1979).

[82] P. Napolitani, et al., Phys. Lett. B **726**, 382 (2013).

[83] J. Aichelin, et al., Phys. Lett. B **176**, 14 (1986).

[84] J. Aichelin, Physics Reports **202**, 233 (1991).

[85] A. Ono, Phys. Rev. C **59**, 853 (1999).

[86] A. Ono, J. Phys: Conference Series **420**, 012103 (2013).

[87] N. Ikeno, et al., Phys. Rev. C **93**, 044612 (2016).

[88] E. Chabanat, et al., Nuclear Physics A **635**, 231 (1998).

[89] G. Q. Li, et al., Phys. Rev. C **48**, 2707 (1993).

[90] F. Puhlhofer, Nuclear Physics A **280**, 267 (1977).

[91] G. Baiocco, et al., Phys. Rev. C **87**, 054614 (2013).

[92] L. G. Moretto, Nuclear Physics A **247**, 211 (1975).

[93] N. Bohr, et al., Phys. Rev. **56**, 426 (1939).

[94] D. Lacroix, et al., Phys. Rev. C **69**, 054604 (2004).

[95] D. Lacroix, et al., Phys. Rev. C **71**, 024601 (2005).

[96] J. Błocki, et al., Annals of Physics **105**, 427 (1977).

[97] D. Durand, Nuclear Physics A **541**, 266 (1992).

[98] E. Galichet, et al., Phys. Rev. C **79**, 064614 (2009).

[99] E. De Filippo, et al., Phys. Rev. C **71**, 044602 (2005).

[100] V. E. Viola, et al., Phys. Rev. C **31**, 1550 (1985).

[101] J. Cugnon, et al., Nuclear Physics A **397**, 519 (1983).

[102] M. D'Agostino, et al., Nuclear Physics A **861**, 47 (2011).

[103] J. Frankland, et al., Nuclear Physics A **689**, 905 (2001).

[104] Y. Larochelle, et al., Phys. Rev. C **62**, 051602 (2000).

[105] J. Łukasik, et al., Phys. Rev. C **55**, 1906 (1997).

[106] E. Plagnol, et al., Phys. Rev. C **61**, 014606 (1999).

[107] C. Cavata, et al., Phys. Rev. C **42**, 1760 (1990).

[108] oral discussion with D. Rifuggiato and S. Marletta.

[109] I. Lombardo, et al., Phys. Rev. C **84**, 024613 (2011).

[110] D. Thériault, et al., Phys. Rev. C **74**, 051602 (2006).

[111] E. De Filippo, et al., Phys. Rev. C **86**, 014610 (2012).

[112] S. Piantelli, et al., Phys. Rev. C **76**, 061601 (2007).

[113] S. Hudan, et al., Eur. Phys. J. A **50**, 36 (2014).

[114] N. L. Neindre, Il Nuovo Cimento C **39**, 377 (2016).

[115] A. B. McIntosh, Il Nuovo Cimento C **39**, 405 (2016).

[116] K. Brown, et al., Phys. Rev. C **87**, 061601 (2013).

[117] R. Płaneta, et al., Phys. Rev. C **77**, 014610 (2008).

[118] S. Piantelli, et al., Phys. Rev. C **96**, 034622 (2017).

[119] L. Heilborn, J. Phys. Conf. Series **420** (2013).

[120] Gulminelli, F., et al., Eur. Phys. J. A **30**, 1 (2006).

# Acknowledgements

I would like to thank all the members of the FAZIA collaboration for the help and the support they gave me during these three years.

I thank the GARR for kindly providing me the cloud computing resources, necessary to perform the AMD calculations reported in this work.

I special thank to Akira Ono for according me the use of his AMD code and for his personal help in the grueling tuning phase.